A Chichibabin's Hydrocarbon Based Molecular Cage: The Impact of Structural Rigidity on Dynamics, Stability, and Electronic Properties

A Chichibabin's Hydrocarbon Based Molecular Cage: The Impact of Structural Rigidity on Dynamics, Stability, and Electronic Properties

Yong Ni,[†] Fernando Gordillo-Gámez,[‡] Miriam Peña Alvarez,[§] Zhihan Nan,[†] Zhengtao Li,[†] Shaofei Wu,[†] Yi Han,[†] Juan Casado,*[,‡] and Jishan Wu*[,†,#]

[†]Department of Chemistry, National University of Singapore, 3 Science Drive 3, 117543, Singapore

[‡]Department of Physical Chemistry, Faculty of Science, University of Málaga, CEI Andalucía Tech, Campus de Teatinos s/n, 29071 Málaga, Spain

[§]Center for Science at Extreme Conditions and School of Physics and Astronomy, University of Edinburgh, EH9 3JZ, Edinburgh, UK

[#]Joint School of National University of Singapore and Tianjin University, International Campus of Tianjin University, Binhai New City, Fuzhou 350207, China

KEYWORDS: Molecular cage; Chichibabin's hydrocarbon; diradicaloid; dynamics; molecular recognition

ABSTRACT: A 3D π-conjugated polyradicaloid molecular cage **c-Ph14**, consisting of three Chichibabin's hydrocarbon motifs connected by two benzene-1,3,5-triyl bridgeheads, was synthesized. Compared with its linear model compound ***l*-Ph4**, the prism-like **c-Ph14** has a more rigid structure, which shows significant impact on the molecular dynamics, stability, and electronic properties. A higher rotation energy barrier for the quinoidal biphenyl units was determined in **c-Ph14** (15.64 kcal/mol) than that of ***l*-Ph4** (11.40 kcal/mol) according to variable-temperature NMR measurements, leading to improved stability, a smaller diradical character, and an increased singlet-triplet energy gap. The pressure-dependent Raman spectroscopic studies on the rigid cage **c-Ph14** revealed a quinoidal-to-aromatic transformation along the biphenyl bridges. In addition, the ellipsoidal cavity in the cage allowed selective encapsulation of fullerene C_{70} over C_{60}, with an associate constant of about 1.43×10^4 M^{-1}. Moreover, **c-Ph14** and ***l*-Ph4** exhibited similar redox behavior and their cationic species (**c-Ph14**$^{6+}$ and ***l*-Ph4**$^{2+}$) were obtained by chemical oxidation and the structures were identified by X-ray crystallographic analysis. The biphenyl unit showed a twisted conformation in ***l*-Ph4**$^{2+}$, whereas remained coplanarity in **c-Ph14**$^{6+}$. Notably, molecules of **c-Ph14**$^{6+}$ form one-dimensional columnar structure via close π-π stacking between the bridgeheads.

INTRODUCTION

Over the past decade, open-shell singlet diradicaloids have received intensive studies mainly due to their unique electronic properties arisen from the intermediate bonding emerging from fractional occupation of frontier π-electrons.[1] The molecules exhibit diradical-like behavior and thermally activated paramagnetic activity. However, the practical applications of diradicaloids are still limited by the low stability, although various thermodynamic and kinetic stabilizing strategies have been developed. The topological structures of the investigated diradicaloids varied from rigid planar skeletons[2] to conformationally flexible molecules,[3] contorted helicenes,[4] macrocycles,[5] 3D molecular cages,[6] and even 2D covalent organic radical frameworks.[7] It has been demonstrated that aromaticity played a critical role on their diradical character and singlet-triplet energy gap.[1g] However, there is almost no systematic study on how the structural rigidity affects the molecular dynamics, stability and electronic properties. This issue becomes particularly important for the design of diradicaloids with flexible conformation and tailored diradical character.

Chichibabin's hydrocarbon (CH), *p*,*p*'-biphenylene-bis-(diphenylmethyl), can be considered as the very first open-shell singlet diradicaloid (Figure 1a).[8] The diradical-like behavior can be ascribed to the recovery of two aromatic sextet rings in the diradical form. The compound showed a bright green color in solid state and X-ray crys-

tallographic analysis revealed a planar *p*-di-xylylene backbone, implying dominant contribution from the closed-shell quinoidal resonance form in the crystal (Figure 1a).[9] On the other hand, the solution displayed a blue-violet color and was very sensitive to oxygen, indicating an open-shell diradical character. While it is practically difficult to determine the real conformation of the molecule in solution, one can expect a dynamic process in which the two phenyl rings in the *p*-di-xylylene unit can rotate along the central CC bond due to its partial single-bond nature as described in the open-shell diradical form (Figure 1a). We believe that such dynamic rotation process can be restricted when the CH units are constrained in a rigid 3D topological structure such as a molecular cage, and as a consequence, the conformational stability of CH could be improved. Therefore, we designed and synthesized a rigid molecular cage **c-Ph14** in which three CH units are linked via two benzene-1,3,5-triyl bridgeheads and there are overall fourteen π-conjugated phenyl rings (Figure 1b). Similar to the CH, the individual CH units in **c-Ph14** have the tendency to become open-shell diradicals, and thus the cage is supposed to display multiple diradical characters. Different from the normal CH, two of the phenyl substituents are replaced by bulky mesityl (Mes) groups which simultaneously provide kinetic stabilization and structural restriction(congestion) in such a way that the CH units always adopt a *cis*- configuration in the cage. For comparison, a CH analogue ***l*-Ph4** with two Mes and two 4-bromophenyl groups was also synthesized, which is supposed to exhibit a *cis*-/*trans*- isomerization via a diradical transition state in the free conformational state (Figure 1c). Detailed studies on the neutral molecules as well as their charged species allow us to understand how the structural rigidity in a 3D π-conjugated molecular cage affects the molecular dynamics, stability, and electronic properties. In addition, the rigid cage-like structure also offers the possibility to investigate free volume cavity controlled properties such as; i) pressure dependent quinoid-benzenoid interconversion,[10] and space spherical filling by host-guest chemistry with fullerenes.[11]

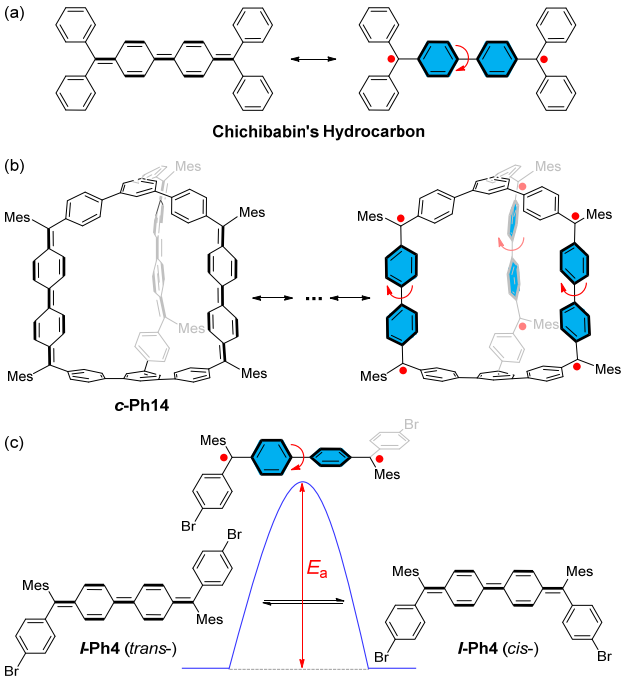

Figure 1. Structures of (a) Chichibabin's hydrocarbon, (b) the new Chichibabin's hydrocarbon based molecular cage **c-Ph14**, and (c) the model compound ***l*–Ph4** with possible *cis*-/*trans*- isomerization via a diradical transition state. The aromatic sextet rings are shaded in blue color.

RESULTS AND DISCUSSION

Synthesis. Synthesis of 3D π-conjugated molecular cages is a challenging task, and recently, dynamic alkyne metathesis,[12] Suzuki coupling,[13] Yamamoto coupling,[6,14] and platinum (Pt)-mediated assembly of stannylated subunits followed by reductive elimination of Pt,[15] turned out to be efficient ways. Herein, a key intermediate **4** containing three 4-bromophenyl groups was first synthesized (Scheme 1). Nucleophilic addition of 4,4′-dibromobenzophenone **1** with excess amount of 2-mesitylmagnesium bromide generated the alcohol intermediate **2** and subsequent methylation by iodomethane gave compound **3** in 86% yield over two steps. A three-fold Suzuki coupling reaction between an excess amount of **3** and 1,3,5-tris(4,4,5,5-tetramethyl-1,3,2-dioxaborolan-2-yl)benzene afforded the precursor **4** in 55% yield. The steric repulsion amongst the mesityl substituents and neighboring phenyl units gives rise to a dihedral angle that is optimal for the $Ni(COD)_2$ mediated Yamamoto homo-coupling of **4** to build the cage structure **5** in 26% yield, after purification by preparative gel permeation chromatography (*pre*-GPC). Six-fold reductive elimination of the methoxy groups in **5** by $SnCl_2$ in dichloromethane (DCM) generated the fully conjugated molecular cage **c-Ph14** in nearly quantitative

yield. The model compound ***l*-Ph4** was synthesized from the building block **6**[16] through a similar nucleophilic addition, methylation and reduction sequence (Scheme 1). The bulky mesityl groups attached onto ***c*-Ph14** and ***l*-Ph4** ensure sufficient stability and solubility, and both compounds can be purified by normal silica gel column chromatography.

Scheme 1. Synthetic route for *c*-Ph14 and *l*-Ph4[a]

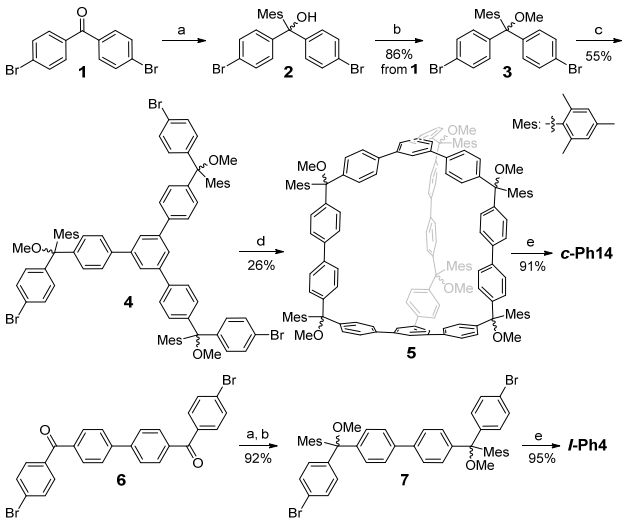

[a]Conditions: (a) MesMgBr, THF, R.T., 4h; (b) NaH, CH_3I, THF, R.T., 6h; (c) 1,3,5-tris(4,4,5,5-tetramethyl-1,3,2-dioxaborolan-2-yl)benzene, $Pd_2(dba)_3$, PPh_3, Cs_2CO_3, CsF, toluene/DMF, reflux, 24h; (d) $Ni(COD)_2$, 2,2'-bipyridine, THF, 65 °C, 72h; (e) $SnCl_2$, DCM, R.T., 12h.

Ground-state geometry. Single crystals suitable for X-ray crystallographic analysis were obtained by slow diffusion of acetonitrile into the THF solution of ***l*-Ph4**.[17] The molecule adopts a C_i symmetry with *trans*- configuration (Figure 2a). Like the CH,[9] the fourteen di-*p*-xylylene carbons in ***l*-Ph4** are essentially coplanar (Figure 2b). The bulky mesityl substituents are almost perpendicular to the mean molecular plane (torsional angle: 72.5°), and the sterically congested 4-bromophenyl groups are displaced out of the main plane with a torsional angle of 35.8°. Bond length analysis clearly disclosed aromatic character of the two outer phenyl rings with the harmonic oscillator model of aromaticity (HOMA)[18] value (0.96) close to the ideal benzene model (HOMA: 1.0). In contrast, large bond alternation was observed in the central di-*p*-xylylene unit, and a much smaller HOMA value (0.57) was calculated for these two six-membered rings, indicating a non-aromatic quinoidal structure. The bond length of central C1-C1' bond (1.427 Å) is much longer than that in typical olefins (1.33 Å) but shorter than the aryl-aryl single bond distance in biphenyl (1.493 Å), suggesting an intermediate open-shell diradical character. Indeed, natural orbital occupation number (NOON) calculations (UCAM-B3LYP/6-31G(d,p)) based on the X-ray structure of ***l*-Ph4** predicted a moderate diradical character (y_o = 0.73, defined as the occupation number of the lowest unoccupied natural orbital (LUNO)). Single crystal of ***c*-Ph14** could not be obtained after many efforts, and its geometry was only assessed by DFT calculations (UB3LYP/6-31G(d,p)). It is predicted that ***c*-Ph14** adopts C_{3h} symmetry, and the three bridges adopt a propeller-like geometry (Figure 2c,d). The bridgehead 1,3,5-triphenylbenzene units display strong aromatic character (HOMA = 0.92/0.94), indicating that the CHs are nearly decoupled due to the cross-conjugated 1,3,5-linkage mode. The three di-*p*-xylylene units are predicted to have a planar geometry with a large bond alternation and small HOMA value (0.50), similar to CH and ***l*-Ph4**. The distance between neighboring methine sites (C2-C3/C3-C4/C4-C2) along one bridgehead is as long as 11.809 Å, implying weak through-space electronic coupling between the three CH units. Indeed, NOON calculations based on the optimized geometry of ***c*-Ph14** predicted similar multi-diradical characters with y_o = 0.67, y_1 = 0.66, and y_2 = 0.51, which are defined as the occupation number of LUNO, LUNO+1, and LUNO+2, respectively. The y_o value is slightly smaller than that of ***l*-Ph4**, indicating that structural restriction in a 3D cage structure may lead to higher rotation barrier and a larger singlet-triplet energy gap ($\Delta E_{S\text{-}T}$). On the other hand, the similitude of the y_o, y_1, and y_2 indices indicate the development of diradical character in each CH unit is almost independent from the others. This hypothesis was verified by variable-temperature (VT) nuclear magnetic resonance (NMR) and electron spin resonance (ESR) measurements of both ***l*-Ph4** and ***c*-Ph14** (*vide infra*).

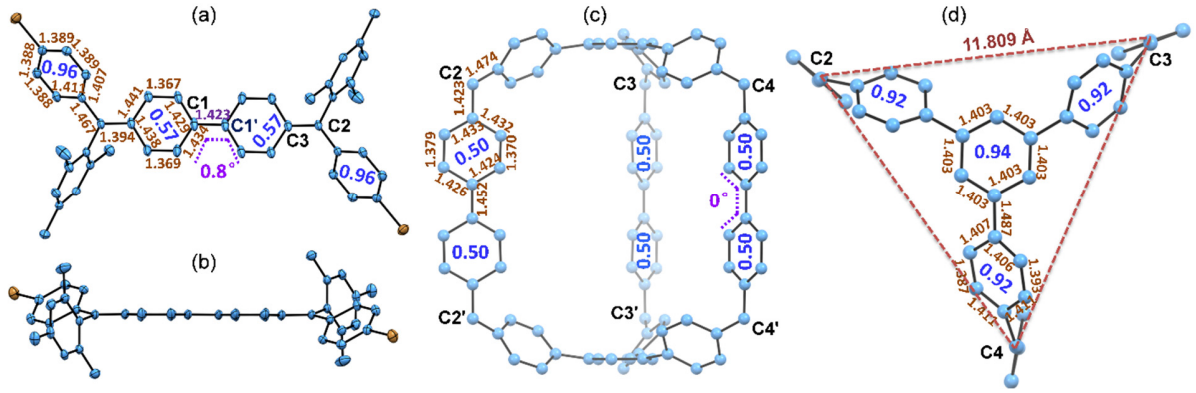

Figure 2. X-ray crystallographic structure of ***l*-Ph4** and optimized structure of **c-Ph14**: (a)/(d) top view; (b)/(c) side view. Hydrogen atoms (for both) and mesityl substituents (for **c-Ph4**) are omitted for clarity. Selected bond lengths (in Å) and dihedral angles in the biphenyl subunits are labeled, and the blue numbers in individual rings are the calculated HOMA values.

Molecular dynamics. Although ***l*-Ph4** was found only in *trans-* configuration in the single crystal, it should have a *cis-* isomer, which might be in equilibrium with the *trans-* isomer in solution (Figure 1c). DFT calculations (UB3LYP/6-31G(d,p)) indicate that the *cis*-isomer almost has the same energy to the *trans-* isomer ($\Delta E_{cis\text{-}trans}$ = 0.01 kcal/mol). VT NMR measurements were conducted for ***l*-Ph4** in THF-d_8 to determine the possible dynamic interconversion process (Figure 3a,b). The ^{1}H NMR spectrum at 268 K is well-resolved and can be fully assigned by 2D COSY and NOESY NMR techniques (Figures S3-S7 in the Supporting Information (SI)). Only one set of averaged resonances was observed due to fast exchange between *cis-*/*trans-* isomers relative to NMR timescale. As the temperature was lowered, the signals were gradually broadened and became fully coalescent at about 258-243 K. Further cooling of the solution resulted in splitting of all the peaks into two sets of signals, which can be assigned to the *cis-* and *trans-* isomer, respectively, indicating a slow *cis-*/*trans-* isomerization process on the NMR timescale. The *cis-*/*tran-* isomers are in an approximately 1:1 ratio below 233 K as estimated from integration of the respective resonance, in accordance with their nearly identical populations as predicted by energy calculations. The *cis-*/*trans-* exchange rate constants (k [s^{-1}]) in the temperature range from 268 K to 218 K were then estimated by careful line-shape analysis of the pair-peaks 6/6′ (see details in SI).[19] The interconversion rate constants k were plotted versus the reciprocal absolute temperature ($1/T$) and the data was then fitted by Eyring equation $\ln\frac{k}{T} = -\frac{\Delta H^{\ddagger}}{R}\times\frac{1}{T} + \ln\frac{k_B}{h} + \frac{\Delta S^{\ddagger}}{R}$ to give the thermodynamic activation parameters $\Delta H^{\ddagger}$ = 112.32±3.15 kJ·mol^{-1} and $\Delta S^{\ddagger}$ = 266.7±13.3 J·mol^{-1}·K^{-1} (Figure 3c). The positive value of $\Delta S^{\ddagger}$ reveals the formation of a distorted transition state in agreement with our hypothesis. The interconversion energy barrier at the coalescence temperature $\Delta G^{\ddagger}_{Tc}$ (T_c = 243K) was then estimated to be 47.51 kJ·mol^{-1} (11.4 kcal·mol^{-1}) related with the energy required to complete the scission of the π–bond from the partial diradical in the reactant/product up to the transition state. It should be noted that the *cis-*/*trans-* isomerization can happen by rotation along either C1-C1′ bond or C2-C3 bond, but according to the X-ray crystallographic data, the former (1.423 Å) is obviously longer than the latter (1.394 Å) (Figure 2a), implying a larger single-bond character. Therefore, the measured interconversion energy barrier based on the protons 6/6′ should be correlated to the rotation barrier about the central C1-C1′ bond.

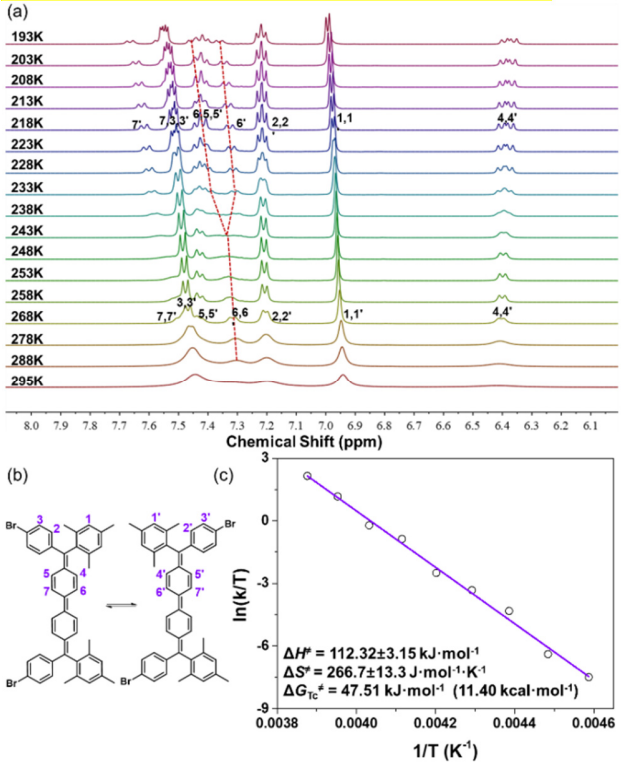

Figure 3. (a) VT ^{1}H NMR spectra (aromatic region) of ***l*-Ph4** in THF-d_8; (b) the labeling in the *cis*- and *trans*- isomers; (c) kinetic analysis of the exchange rate constants at different temperatures by Eyring equation.

In the rigid molecular cage **c-Ph14**, although the CH units are locked in *cis*- configuration, the phenyl rings in the di-*p*-xylylene moieties may still undergo a dynamic restricted flipping process due to the partially single-bond character of the central C-C bond. Indeed, this dynamic flipping process was also found by VT-NMR measurements in THF-d_8 (Figure 4a,b). At low temperature range (T < 300K), two split doublets were observed in an integration ratio of 1:1, which can be assigned to pair-protons 5/5′ based on 2D COSY and NOESY NMR techniques (Figures S8-S9 in SI), indicating that the flipping of phenyl rings in the di-*p*-xylylene unit is slow on NMR timescale. As the temperature was increased, the flipping speeded up, and the two doublets (5/5′) tended to merge together and became fully coalescent at around 310 K. Further heating of the solution would expectedly lead to a well-resolved spectrum with only one set of sharpened peaks. However, severe signal broadening was found above 315 K due to remarkable thermal population from the diamagnetic singlet species to the paramagnetic triplet species, thus hampering the observation and quantification of the fast ring rotation process. The flipping rate constants (k [s^{-1}]) in the range from 310 to 270 K can be estimated by using similar line-shape analysis as ***l*-Ph4** (see details in SI), and fitting by Eyring equation gave the thermodynamic parameters $\Delta H^{\ddagger}$ and $\Delta S^{\ddagger}$ as 112.81 ± 4.23 kJ/mol and 153.67 ± 14.25 J/(mol·K), respectively (Figure 4c). The flipping energy barrier at the coalescence temperature $\Delta G^{\ddagger}_{Tc}$ (T_c = 310 K) was then estimated to be 65.17 kJ·mol^{-1} (15.64 kcal·mol^{-1}), which is much larger than the *cis*-/*trans*- isomerization energy barrier of ***l*-Ph4**. The largely increased barrier can be attributed to the conformational restriction in the rigid cage framework, which also explains the smaller diradical character in comparison to ***l*-Ph4**. Consequently, **c-Ph14** exhibited much better stability (half-life time $t_{1/2}$ = 22.6 days) than ***l*-Ph4** ($t_{1/2}$ = 13.1 days) under ambient air and light conditions as monitored by UV-vis absorption spectroscopy (Figure S1 in SI).

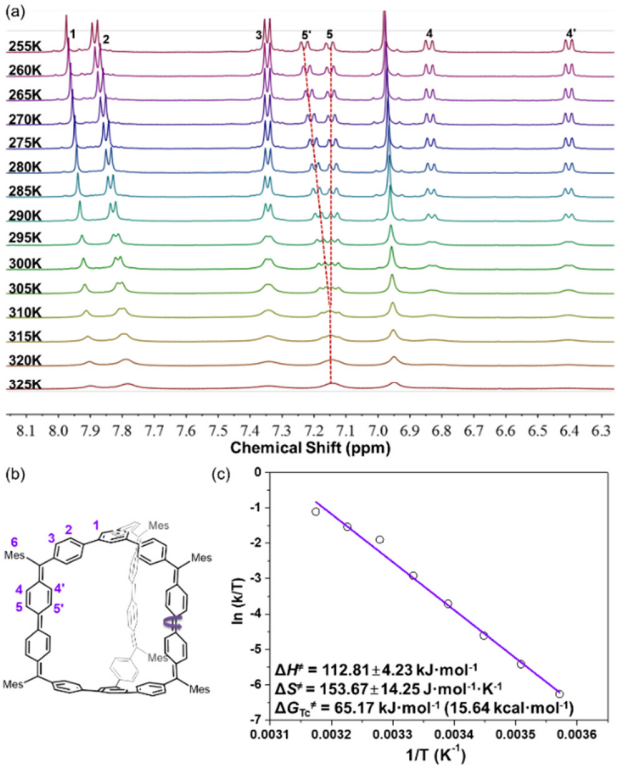

Figure 4. (a) VT ^{1}H NMR spectra (aromatic region) of **c-Ph14** in THF-d_8; (b) the labeling; (c) kinetic analysis of the exchange rate constants at different temperatures by Eyring equation.

Magnetic properties. Compound **c-Ph14** showed a well-resolved ^{1}H NMR spectrum at 295 K in THF-d_8, while heating the solution resulted in severe signal broadening, in particular for the protons on the quinoidal biphenyl subunits (Figure 4a), which can be explained by the existence of thermally populated triplet species as commonly observed in many open-shell singlet diradicaloids.[1] In contrast, ***l*-Ph4** in THF-d_8 exhibited extremely broadened NMR signals even at 288 K (Figure 3a), in accordance with its larger calculated diradical character. The magnetic properties of **c-Ph14** and ***l*-Ph4** were further investigated by VT ESR measurements (Figure 5). **c-Ph14** displayed an unresolved one-line ESR spectrum with g_e of 2.00276 (Figure 5a), implying carbon-centered π–radicals. The signal intensity gradually decreased upon lowering temperature, consistent with its open-shell singlet ground state. Fitting of the VT-ESR data recorded in frozen THF solution by Bleaney–Bowers equation[20] gave a singlet–triplet gap ($\Delta E_{S\text{-}T}$) of -3.04 kcal/mol (Figure 5b). Calculations (UCAM-B3LYP/6-31G(d,p)) on the singlet diradicals show that the spins are well distributed among three bridges, with the spin density mainly delocalized along the di-*p*-xylylene moieties (inset in Figure 5b), indicating weak through-space coupling. Compound ***l*-Ph4** in THF showed a similar

one-line ESR spectrum (g_e = 2.00264) and temperature dependence (Figure 5c). Fitting of the ESR gave a smaller $\Delta E_{S\text{-}T}$ of -2.56 kcal/mol (Figure 5d). The spins are well delocalized along the di-*p*-xylylene unit as well as the two 4-bromophenyl groups (inset in Figure 5d). The larger singlet–triplet gap of **c-Ph14** is in good agreement with its smaller diradical character, larger flipping energy barrier, and better stability as compared to ***l*-Ph4**. Thus, conformational restriction plays a critical role in molecular dynamics, as well as electronic and magnetic properties of a cage-shaped polyradicaloid, **c-Ph14**.

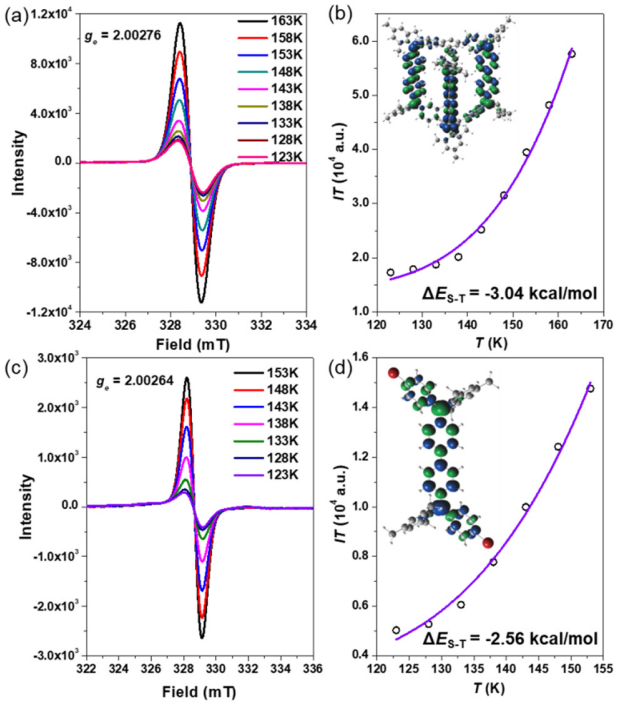

Figure 5. VT ESR spectra and *IT*-*T* plots of (a), (b) **c-Ph14** and (c), (d) ***l*-Ph4** in frozen THF. *I*: integrated ESR intensity; *T*: temperature in K. The violet lines in (b) and (d) are the fitted curves, and inseted are the calculated spin-density distribution maps of the singlet diradicals.

Optical and electrochemical properties. Compounds **c-Ph14** and ***l*-Ph4** have good solubility in common organic solvents, resulting in red color solutions. The UV-vis absorption spectra of both compounds in DCM are compared in Figure 6a. ***l*-Ph4** shows a major absorption band with maximum (λ_{max}) at 552 nm (ε = 1.93×10^5 M^{-1}·cm^{-1}), accompanied by a long tail up to 700 nm. **c-Ph14** displays a similar band structure but with 19 nm blue shift (λ_{max} = 533 nm, ε = 4.89×10^5 M^{-1}·cm^{-1}) due to the larger conformational restriction. The molar coefficient of **c-Ph14** at the absorption maximum is 2.53 times as that of ***l*-Ph4**, implying weak electronic coupling between the CH units.

The electrochemical properties of **c-Ph14** and ***l*-Ph4** were studied by cyclic voltammetry (CV) and differential pulse voltammetry (DPV) measurements in dry DCM solutions (Figures 6b). ***l*-Ph4** showed two reversible oxidation waves with half-wave potential ($E_{1/2}^{ox}$) at 0.16 and 0.40 V and two reversible reduction waves with half-wave potential ($E_{1/2}^{red}$) at -1.52 and -1.75 V (vs Fc/Fc$^+$, Fc = ferrocene). Oxidative titration of ***l*-Ph4** with NO·SbF$_6$ gave corresponding radical cation (λ_{max}= 1620/686 nm, ε = 0.27/0.67×10^5 M^{-1}·cm^{-1}) and dication (λ_{max} = 575 nm, ε = 0.78×10^5 M^{-1}·cm^{-1}) (Figure S2 in SI), which can also be unambiguously generated upon stepwise electrochemical oxidation (Figure 7a).

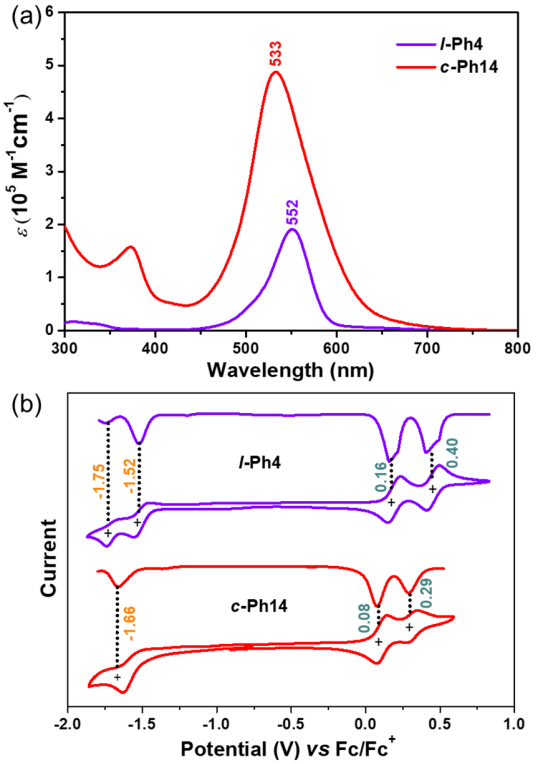

Figure 6. (a) UV-vis absorption spectra of **c-Ph14** and ***l*-Ph4** in DCM. (b) Cyclic voltammograms and differential pulse voltammograms of **c-Ph14** and ***l*-Ph4** in DCM.

For **c-Ph14**, despite the existence of three CH subunits and the multiple diradical characters, similar cyclic voltammogram was recorded with two reversible oxidation waves at $E_{1/2}^{ox}$ = 0.076, 0.29 V (vs Fc/Fc$^+$) as compared to ***l*-Ph4**, attributing to the weak through-space coupling between the CH bridges. Oxidative titration of **c-Ph14** with NO·SbF$_6$ was difficult to control to give pure intermediate states (Figure S2 in SI). Alternatively, stepwise electrochemical oxidation provided three clear oxidation states sequentially (Figure 7b), which can be assigned to the corresponding dication, tetracation and hexacation of **c-Ph14** by

comparison with the absorption spectra of ***l*-Ph4**$^{+\bullet}$ and ***l*-Ph4**$^{2+}$. The absorption spectrum of the first oxidation state of ***c*-Ph14** exhibited a band at 702 nm together with a broad band at 1580 nm tailing up to almost 2000 nm, which is highly correlated with the band structure of the ***l*-Ph4**$^{+\bullet}$ (λ_{max} = 686/1620 nm). However, while the lowest energy band maximum is blue-shifted (1580 nm versus 1620 nm), the higher energy peak is red-shifted (702 nm versus 686 nm) as compared to ***l*-Ph4**$^{+\bullet}$. While we should expect a unison large red-shit/blue-shift of the two bands if the charge would spread over a larger/smaller (more confined) π–core than in ***l*-Ph4**$^{+\bullet}$, such as previsibly would be the cases of the radical cation/radical trication species, the slight changes found on first oxidation indicated the formation of the intermediate diradical dication of ***c*-Ph14** (i.e., ***c*-Ph14**$^{2+}$ where the charges are separated along two bridges in the 3D cage-shaped architecture, or ***c*-Ph14**$^{2(+\bullet)}$). Posterior oxidation of ***c*-Ph14** gave rise to the full clearance of the 702/1580 nm bands accompanied with the concomitant emergence a new band at 593 nm, similar as what has been observed for the ***l*-Ph4**$^{2+}$, but with a slight red-shift (593 nm versus 575 nm). With the same reasoning, the second oxidation state of ***c*-Ph14** was neither a singly confined dication nor a triple dication, but a tetracation (i.e., ***c*-Ph14**$^{4+}$ or ***c*-Ph14**$^{2(2+)}$). Further oxidation of ***c*-Ph14** led to a species with an ***l*-Ph4**$^{2+}$-like absorption band at 565 nm. According to the previous logic and supported by the fact that this species appeared at higher potential than ***c*-Ph14**$^{4+}$, the new oxidized species was the hexacation (i.e., ***c*-Ph14**$^{6+}$ or ***c*-Ph14**$^{3(2+)}$). The Coulomb repulsion among the three dicationic bridges in the cage framework provoked the blue shift of ***c*-Ph14**$^{6+}$ as compared to ***l*-Ph4**$^{2+}$. Moreover, ***l*-Ph4**$^{2+}$ and ***c*-Ph14**$^{6+}$ can be isolated in single-crystal forms by adding two and six equivalent of NO·SbF_6 to the solution of ***l*-Ph4** and ***c*-Ph14** in one portion, respectively.

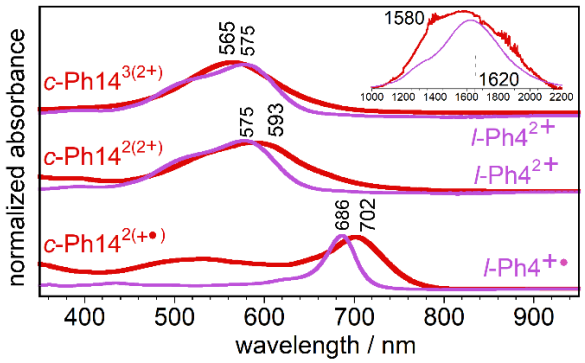

Figure 7. Normalized UV-Vis-NIR absorption spectra of the oxidized species of ***l*-Ph4** (***l*-Ph4**$^{+\bullet}$ and ***l*-Ph4**$^{2+}$) and those of ***c*-Ph14** (***c*-Ph14**$^{2+}$, ***c*-Ph14**$^{4+}$ and ***c*-Ph14**$^{6+}$) all generated from spectroelectrochemistry in 0.1 M $TBAPF_6$ in DCM at 300 K. The inser corresponds to the NIR part of the spectra of ***l*-Ph4**$^{+\bullet}$ and ***c*-Ph14**$^{2+}$.

Crystallographic structures and dynamic NMR spectra of *l*-Ph4^{2+} and *c*-Ph14^{6+}. X-ray crystallographic analysis[17] on a single crystal of ***l*-Ph4**$^{2+}$ revealed a C_i symmetric geometry (Figure 8a), in which the central biphenyl rings are distorted to a dihedral angle of 32.9°, differed from the co-planarity in neutral state. The central C1-C1′ bond now becomes much longer (1.473 Å). In addition, smaller bond length alternation in the central biphenyl ring was observed with a higher HOMA value (0.81) as compared to ***l*-Ph4**. All these indicate a transformation from a quinoidal structure to an aromatic one upon oxidation. Two counter ions (SbF_6^-) locate in close contact to the molecular backbone, and the Coulomb repulsion among the two delocalized positive charges enhances the structural rigidity of ***l*-Ph4**$^{2+}$, thereby the rotation of the phenyl rings along the central C-C bond was restricted allowing an energy barrier in a detectable range of NMR. The ^{1}H NMR spectrum of ***l*-Ph4**$^{2+}$ in CD_2Cl_2 displayed one set of broad resonances at room temperature, while cooling the solution led to more broadened signals which became fully coalescent at 288 K (Figure S11 in SI). Upon further lowering the temperature down to 253 K, the signal for protons 6/7 were split into two well-resolved doublets at an integration ratio of 1:1. The rotation rate constant (k [s^{-1}]) in the range from 298 to 253 K can be estimated by using similar line-shape analysis as ***l*-Ph4**, and fitting by Eyring equation gave the thermodynamic parameters $\Delta H^{\ddagger}$ and $\Delta S^{\ddagger}$ as 107 ± 2.03 kJ/mol and 171.2 ±7.48 J/(mol·K), respectively. Accordingly, the rotation energy barrier at the coalescence temperature $\Delta G^{\ddagger}_{Tc}$ was estimated as 57.72 kJ/mol (13.85 kcal/mol, T_c = 288 K) (Figure S25 in SI). Similar to the neutral compound, the bond length (1.473 Å) of C1-C1′ is longer than that of C2-C3 (1.450 Å), and thus this measured energy barrier is mainly correlated to the rotational barrier along the C1-C1′ bond. This is a rare example in which rotation along the C-C single bond is slowed down due to Coulomb interactions.

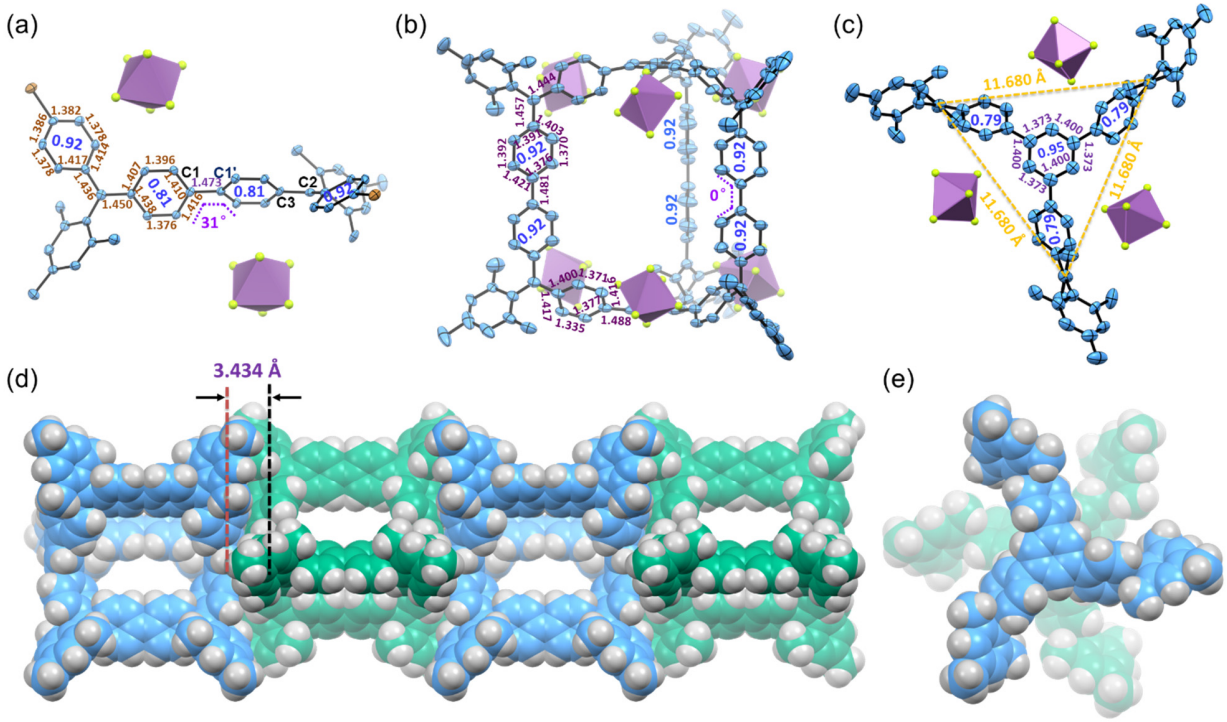

Figure 8. X-ray crystallographic structures of ***l*-Ph4**$^{2+}$ (a), and **c-Ph14**$^{6+}$ from side view (b) and top view (c). Hydrogen atoms are omitted for clarity. Selected bond lengths (in Å) and dihedral angle along the biphenyl subunit are labeled, and the blue numbers in individual rings are the calculated HOMA values. The packing structure of **c-Ph14**$^{6+}$ was also shown from side view (d) and top view (e).

The prism-like structure of **c-Ph14**$^{6+}$ was unambiguously confirmed by X-ray crystallography (Figure 8b,c).[17] The molecule adopts a high C_{3h} symmetry with three bridges in a propeller-like geometry. The six SbF_6^- counter ions locate along the prism and fill the grooves homogenously surrounding two bridgeheads, with close contact to the molecular skeleton. Bond length analysis clearly disclosed three sets of aromatic biphenyl units with small bond length alternation and a large HOMA value (0.92). Unlike the distorted conformation in ***l*-Ph4**$^{2+}$, the biphenyl unit along each bridge of **c-Ph14**$^{6+}$ remains coplanar, presumably due to a high structural rigidity induced by the strong Coulomb repulsion among three dicationic bridges. A similar dynamic flipping process for the biphenyl subunits of **c-Ph14**$^{6+}$ was also observed by VT NMR measurements in CD_2Cl_2 (Figure S15 in SI), but with a larger rotation energy barrier as compared to the model compound ***l*-Ph4**$^{2+}$. For **c-Ph14**$^{6+}$, since the coalescence temperature is higher than the detection limit of CD_2Cl_2, ^{1}H NMR spectrum with one set of well-resolved sharp signals at high-temperature range can't be recorded (changing the solvent to $C_2D_2Cl_4$ with high boiling point resulted in degradation of **c-Ph14**$^{6+}$). Lineshape analysis on the VT-NMR data in the range from 298 K to 263 K and fitting of the data by Eyring equation gave the thermodynamic parameters $\Delta H^{\ddagger}$ and $\Delta S^{\ddagger}$ as 90.24 ± 3.33 kJ/mol and 91.53 ± 11.6 J/(mol·K) (Figure S26 in SI), respectively. Accordingly, $\Delta G^{\ddagger}$ at 288 K was estimated to be 63.88 kJ/mol (15.33 kcal/mol), which is much higher than that of ***l*-Ph4**$^{2+}$ at the same temperature (13.85 kcal/mol). So, again, structural rigidity enhanced the rotation energy barrier in the dicationic form of each CH bridge.

The benzene-1,3,5-triyl bridgeheads in **c-Ph14**$^{6+}$ display strong aromatic character (HOMA: 0.95), whereas the six phenyl rings surrounded are highly bent and deviated from conventional aromatic benzene ring (HOMA value: 0.79) (Figure 8c). **c-Ph14**$^{6+}$ exhibits interesting packing mode in single crystal. In the *ab* plane, molecules pack tightly with SbF_6^- counter ions as well as the *mesityl* groups of adjacent molecules filling the grooves, and the six-surrounding molecules form a hexagonal pattern (Figure S31 in SI). Interestingly, significant π-π interaction was observed between the benzene-1,3,5-triyl bridgeheads of neighboring molecules (with a distance of about 3.434 Å) (Figure 8d and Figure S32 in SI), in spite of the bent 3D-cage skeleton and intermolecular Coulomb repulsion. 1D column is formed, with neighboring propeller-like cage molecules stacked with each other after rotation by 60 degrees along the *c* axis (Figure 8e).

Raman spectra of neutral and oxidized species. To gain a better insight into the changes of struc-

tural and electronic features upon oxidation, Raman spectra were recorded for the neutral and oxidized states of both **c-Ph14** (Figure 9) and ***l*-Ph4** (Figure S19 in SI). Whereas the neutral **c-Ph14** showed the main Raman band at 1597 cm^{-1}, multiple oxidation led to the rise of a new band for typical aromatic benzenes at 1605 cm^{-1}. Meanwhile, the characteristic bands at low frequency range (1120 to 1330 cm^{-1}) were diminished. In particular, the clearance of these bands was observed for **c-Ph14^{6+}**, in which all the quinoidal fragments are fully oxidized to be aromatic. Thereby, the band at 1324 cm^{-1} due C-C stretching and at 1220-1119 cm^{-1} assigned to mixed C-C stretches + C-H deformation modes all arise from the quinoidal biphenyl moiety of the neutral[21] (the band at 1535 cm^{-1} likely arises from the trisubsttuted benzene). Similarly, oxidation provoked an up-shift of the main Raman band of the neutral ***l*-Ph4** from 1577 cm^{-1} to 1580 cm^{-1} and 1603 cm^{-1} in the radical cation and dication, respectively (Figure S19 in SI). The changes, however, are larger (26 cm^{-1}, from 1577 to 1603 cm^{-1}) in ***l*-Ph4** than in **c-Ph14** (8 cm^{-1}, from 1597 to 1605 cm^{-1}), revealing a high degree of conformational restriction in **c-Ph14** that reduces (i.e., makes more energetic) the amplitude of the quinoidal→aromatic conversion upon oxidation in the cage in line with previous data. On the other hand, the similitude between ***l*-Ph4^{2+}** and **c-Ph14^{6+}** is in line with the fact that each arm bears two positive charges.

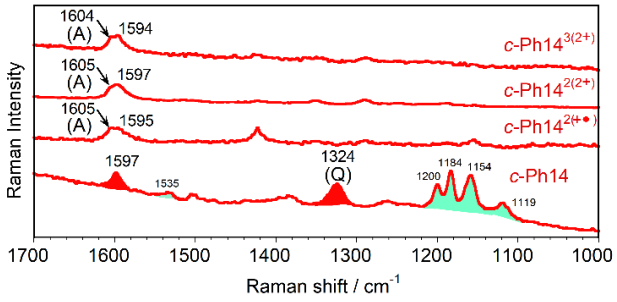

Figure 9. Raman spectra of **c-Ph14** and its oxidized species **c-Ph14^{2+}**, **c-Ph14^{4+}** and **c-Ph14^{6+}** in DCM at 300K. Q/A: quinoidal/aromatic bands.

Pressure depedent Raman spectra of c-Ph14. It is well-known that π-conjugated molecules undergo a wide range of conformational transformations under high pressure,[10] which can also be used to modulate the electro-optical properties of materials. Therefore, it would be of great interest to investigate conformational and electronic diversity of a conjugated cage-shaped molecule consisting of both quinoidal and aromatic phenyl rings. To test this hypothesis, the evolution of the Raman spectra of **c-Ph14** in solid state at room temperature upon variable pressure were recorded (Figure 10a).

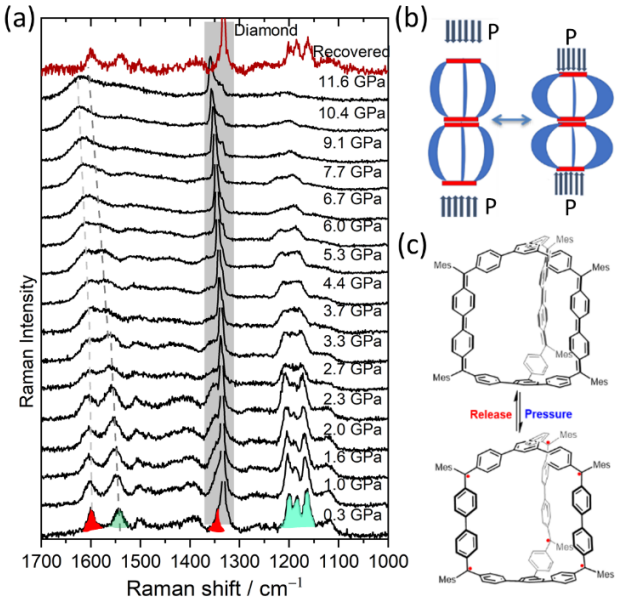

Figure 10. (a) Pressure dependent Raman spectra of **c-Ph14** in solid state at 300K. (b) Qualitative view of the deformation of **c-Ph14** under pressure, the red discs represent benzene-1,3,5-triyl bridgeheads and the blue parts represent quinoidal biphenyls. (c) Proposed quinoidal to aromatic transformation upon pressure at a molecular level.

Interestingly, the two bands at 1597 (of the quinoidal biphenyl) and 1535 cm^{-1} (of the connecting tri-substituted benzenes) progressively coalesced into a broad one at high pressure at room temperature, suggesting a structural deformation of the cage with pressure. At molecular level, the increment of pressure would decrease the volume of the cavity, which can be viewed as a flattening of the cage (Figure 10b). Considering the unique π-π stacking as observed in the crystal of **c-Ph14^{6+}**, it is reasonable to assume that pressure is transmitted intermolecularly through direct contacts between the benzene-1,3,5-triyl bridgeheads (Figure 10b). In parallel, the biphenyl quinoidal cores are subsequently deformed to reduce the molar volume.[10] Noticed that the nature of the pressure effect in these two bands is different as revealed by the different behaviour of their wavenumbers with pressure (see Figure S20). The Raman spectra of **c-Ph14** under pressure exhibited a similar band structure to **c-Ph14^{6+}** in 1500-1600 cm^{-1}, and the clearance of bands within 1120-1330 cm^{-1} underlined a common structural response to pressure and to oxidation, suggesting a quinoidal to aromatic transformation of the central biphenyl subunits. Thereby, pressure serves as external stimuli to reach multiradical states of **c-Ph14** by enforcing the quinoidal bridges to open-shell radical form (Figure 10c). Moreover, the whole pressure cycle is reversible, that is, when the external

pressure is released, a Raman spectrum that highly matched with **c-Ph14** under ambient pressure was recovered.

Host-guest chemistry with fullerenes. Considering the well-defined cavity of **c-Ph14**, the molecule may serve as a supramolecular host for selective encapsulation of certain type of π-conjugated guest molecules with convex surface, such as fullerenes C_{60} and C_{70}.[11] The binding of **c-Ph14** with C_{60} and C_{70} was monitored by UV-vis absorption and fluorescence titration experiments (Figure 11a,c). Upon gradual addition of C_{60}, no appreciable change was observed in both absorption and fluorescence spectra (Figure S27 in SI). In contrast, a clear fluorescence quenching was observed when the solution of **c-Ph14** in 1,2-dichlorobenzene was titrated with C_{70} (Figure 11c), indicating the existence of intermolecular electronic interaction between **c-Ph14** and C_{70}. Fitting of the fluorescence change at 780 nm under different concentrations gave an association constant (K_a) of $1.43\times10^4 \pm 350.5$ M^{-1}.[22] Judging from Job's plot (Figure 11b), the complexation stoichiometry was determined to be 1:1, which was further supported by MALDI-TOF mass spectroscopic analysis (Figure S28 in SI). The **c-Ph14**-C_{70} complex clearly showed two peaks with *m/z* at 841.3 and 1853.8 for both components, as well as a weak peak with *m/z* at 2694.6 corresponding to 1:1 host-guest complex C_{70}@**c-Ph14**. In addition, upon addition of 1 equivalent of C_{70}, all the ^{1}H NMR resonances for the protons on the backbone of **c-Ph14** are slightly shifted to the high field (Figure S29), indicating effective electronic interactions between the host and guest. Furthermore, DOSY NMR analysis (Figures S30-S31) revealed that the **c-Ph14** (D = 6.44 m^2/S) and the 1:1 **c-Ph14**/C_{70} complex (D = 6.31 m^2/S) exhibited a similar diffusion coefficient (D), suggesting that they have similar molecular size and thus C_{70} should be encapsulated inside the cavity of **c-Ph14**. The selective encapsulation of C_{70} over C_{60} can be explained by the ellipsoidal cavity of the cage framework, as demonstrated in the single-crystal structure of **c-Ph14**$^{6+}$. The distance between two benzene-1,3,5-triyl bridgeheads is 13.41 Å, whereas the distance between neighboring methine-carbons surrounding the same bridgehead is 11.68 Å, the resulting cavity fits better with the ellipsoidal surface of C_{70} rather than the spherical surface of C_{60}.

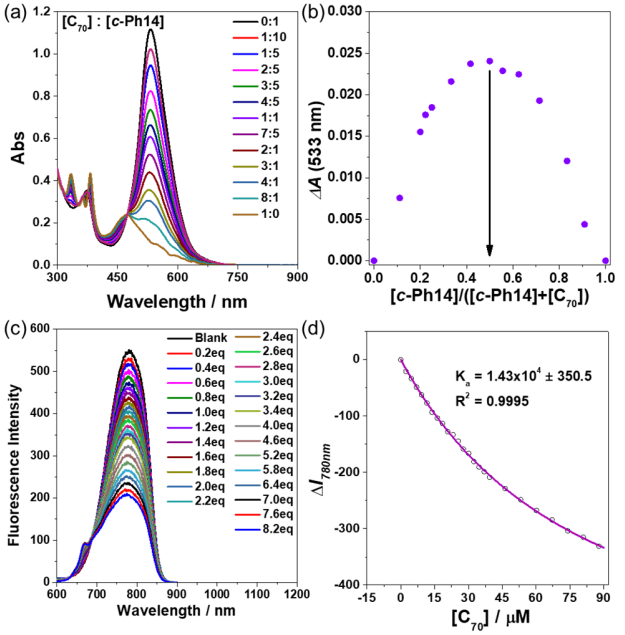

Figure 11. (a) UV-vis absorption spectra of C_{70} and **c-Ph14** at different ratios in 1,2-dichlorobenzene. (b) Job plot of **c-Ph14** and C_{70} based on the UV-vis titration. (c) Fluorescence spectra of **c-Ph14** upon addition of various amount of C_{70}. (d) Plot of fluorescence change at 780 nm (ΔI_{780nm}) versus the concentration of C_{70} ([C_{70}]) in 1,2-dichlorobenzene for estimation of the association constant (K_a), R^2 is the standard deviation.

CONCLUSION

In summary, a 3D π-conjugated polyradicaloid cage **c-Ph14** consisting of three Chichibabin's hydrocarbon motifs connected by two benzene-1,3,5-triyl bridgeheads was synthesized through a concise and efficient strategy. A restricted rotation process was found for the quinoidal biphenyl unit in the rigid molecular cage **c-Ph14** as well as the linear model compound ***l*-Ph4** by dynamic NMR spectroscopic technique, but the former showed a larger energy barrier due to structural rigidity. As a consequence, the cage compound **c-Ph14** exhibited improved stability, a smaller diradical character, and an increased singlet-triplet energy gap compared to ***l*-Ph4**. The rigid cage molecule **c-Ph14** also underwent a quinoidal-to-aromatic transformation upon increased pressure as monitored by Raman spectroscopy. In addition, **c-Ph14** showed selective encapsulation of C_{70} over C_{60} in a 1:1 stoichiometry via its ellipsoidal cavity. X-ray crystallography of ***l*-Ph4**$^{2+}$ and **c-Ph14**$^{6+}$ confirmed aromatic biphenyl subunits in both cases, which were also supported by UV-vis absorption and Raman spectroscopic measurements. Notably, the rigid hexacation **c-Ph14**$^{6+}$ form 1D columnar structure in crystal via intermolecular π-π stacking of the ben-

zene-1,3,5-triyl bridgeheads. Our studies demonstrated how the structural rigidity in 3D π-conjugated molecular cages affected the dynamics, stability, and electronic properties of diradicaloids/polyradicaloids.

ASSOCIATED CONTENT

Supporting Information. The Supporting Information is available free of charge on the ACS Publications website.

Synthetic procedures and characterization data of all new compounds; details for all physical characterizations and theoretical calculations; additional spectra and X-ray crystallographic data (PDF)

X-ray crystallographic data (CIF)

AUTHOR INFORMATION

Corresponding Author

*Email: chmwuj@nus.edu.sg (J.W.); casado@uma.es (J.C.)

Notes

The authors declare no competing financial interest.

ACKNOWLEDGMENT

J.W. acknowleges financial support from the MOE Tier 2 grants (MOE2018-T2-2094 and MOE2019-T2-1-030) and NRF Investigatorship (NRF-NRFI05-2019-0005). J.C. acknowledges MINECO and Junta de Andalucía of Spain project references PGC2018-098533-B-I00 and UMA18FEDERJA057. M.P.-A. acknowledges the support of the European Research Council (ERC) Grant Hecate Reference No. 695527 held by prof. Graeme Ackland. We thank the spectroscopic services from the School of Chemistry of the University of Edinburgh for the access to the Raman spectrometer, in particular to Dr. Andrei Gromov for his help.

REFERENCES

(1) (a) Abe, M. Diradicals. *Chem. Rev.* **2013**, *113*, 7011–7088. (b) Sun, Z.; Zeng, Z.; Wu, J. Zethrenes, Extended *p*-Quinodimethanes, and Periacenes with a Singlet Biradical Ground State. *Acc. Chem. Res.* **2014**, *47*, 2582-2591. (c) Zeng, Z.; Shi, X.; Chi, C.; López Navarrete, J. T.; Casado, J.; Wu, J. Pro-aromatic and Anti-aromatic π-Conjugated Molecules: an Irresistible Wish to be Diradicals. *Chem. Soc. Rev.* **2015**, *44*, 6578–6596. (d) Kubo, T. Recent Progress in Quinoid Singlet Biradical Molecules. *Chem. Lett.* **2015**, *44*, 111–122. (e) Miyoshi, H.; Nobusue, S.; Shimizu, A.; Tobe, Y. Non-alternant non-benzenoid kekulenes: the birth of a new kekulene family. *Chem. Soc. Rev.* **2015**, *44*, 6560–6577. (f) Gopalakrishna, T. Y.; Zeng, W.; Lu, X.; Wu, J. From open-shell singlet diradicaloids to polyradicaloids. *Chem. Commun.* **2018**, *54*, 2186–2199. (g) Liu, C.; Ni, Y.; Lu, X.; Li, G.; Wu, J. Global Aromaticity in Macrocyclic Polyradicaloids: Hückel's Rule or Baird's Rule? *Acc. Chem. Res.* **2019**, *52*, 2309–2321.

(2) For examples, some graphene-like molecules: (a) Konishi, A.; Hirao, Y.; Nakano, M.; Shimizu, A.; Botek, E.; Champagne, B.; Shiomi, D.; Sato, K.; Takui, T.; Matsumoto, K.; Kurata, H.; Kubo, T. Synthesis and Characterization of Teranthene: A Singlet Biradical Polycyclic Aromatic Hydrocarbon Having Kekulé Structures. *J. Am. Chem. Soc.* **2010**, *132*, 11021–11023. (b) Sun, Z.; Huang, K.-W.; Wu, J. Soluble and Stable Heptazethrenebis(dicarboximide) with a Singlet Open-Shell Ground State. *J. Am. Chem. Soc.* **2011**, *133*, 11896–11899. (c) Li, Y.; Heng, K.-W.; Lee, B. S.; Aratani, N.; Zafra, J. L.; Bao, N.; Lee, R.; Sung, Y. M.; Sun, Z.; Huang, K.-W.; Webster, R. D.; López Navarrete, J. T.; Kim, D.; Osuka, A.; Casado, J.; Ding, J.; Wu, J. Kinetically Blocked Stable Heptazethrene and Octazethrene: Closed-Shell or Open-Shell in the Ground State? *J. Am. Chem. Soc.* **2012**, *134*, 14913–14922. (d) Konishi, A.; Hirao, Y.; Matsumoto, K.; Kurata, H.; Kishi, R.; Shigeta, Y.; Nakano, M.; Tokunaga, K.; Kamada, K.; Kubo, T. Synthesis and Characterization of Quarteranthene: Elucidating the Characteristics of the Edge State of Graphene Nanoribbons at the Molecular Level. *J. Am. Chem. Soc.* **2013**, *135*, 1430– 1437. (e) Huang, R.; Phan, H.; Herng, T. S.; Hu, P.; Zeng, W.; Dong, S.; Das, S.; Shen, Y.; Ding, J.; Casanova, D.; Wu, J. Higher Order π-Conjugated Polycyclic Hydrocarbons with Open-Shell Singlet Ground State: Nonazethrene versus Nonacene. *J. Am. Chem. Soc.* **2016**, *138*, 10323–10330. (f) Zeng, W. D.; Sun, Z.; Herng, T. S.; Gonçalves, T. P.; Gopalakrishna, T.Y.; Huang, K.-W.; Ding, J.; Wu, J. Super-heptazethrene. *Angew. Chem. Int. Ed.* **2016**, *55*, 8615– 8619. (g) Zeng, W.; Phan, H.; Herng, T. S.; Gopalakrishna, T. Y.; Aratani, N.; Zeng, Z.; Yamada, H.; Ding, J.; Wu, J. Rylene Ribbons with Unusual Diradical Character. *Chem* **2017**, *2*, 81–92. (h) Ajayakumar, M. R.; Fu, Y.; Ma, J.; Hennersdorf, F.; Komber, H.; Weigand, J. J.; Alfonsov, A.; Popov, A. A.; Berger, R.; Liu, J.; Müllen, K.; Feng, X. Toward Full Zigzag-Edged Nanographenes: peri-Tetracene and Its Corresponding Circumanthracene. *J. Am. Chem. Soc.* **2018**, *140*, 6240–6244. (i) Ni, Y.; Gopalakrishna, T. Y.; Phan, H.; Herng, T. S.; Wu, S.; Han, Y.; Ding, J.; Wu, J. A Peri-tetracene Diradicaloid: Synthesis and Properties. *Angew. Chem. Int. Ed.* **2018**, *57*, 9697–9701. (j) Zeng, W.; Gopalakrishna, T. Y.; Phan, H.; Tanaka, T.; Herng, T. S.; Ding, J.; Osuka, A.; Wu, J. Super-octazethrene: An Open-shell Graphene-Like Molecule Possessing Large Diradical Character but Still with Reasonable Stability. *J. Am. Chem. Soc.* **2018**, *140*, 14054–14058.

(3) Some representative examples: (a) Takahashi, T.; Matsuoka, K.; Takimiya, K.; Otsubo T.; Aso, Y. Extensive Quinoidal Oligothiophenes with Dicyanomethylene Groups at Terminal Positions as Highly Amphoteric Redox Molecules. *J. Am. Chem. Soc.* **2005**, *127*, 8928–8929. (b) Kostenko, A.; Tumanskii, B.; Karni, M.; Inoue, S.; Ichinohe, M.; Sekiguchi, A.; Apeloig, Y. Observation of a Thermally Accessible Triplet State Resulting from Rotation around a Main-Group π Bond. *Angew. Chem. Int. Ed.* **2015**, *54*, 12144–12148. (c) Wentrup, C.; Regimbald-Krnel, M. J.; Mgller, D.; Comba, P. A

Thermally Populated, Perpendicularly Twisted Alkene Triplet Diradical. *Angew. Chem. Int. Ed.* **2016**, *55*, 14600–14605. (d) Zhang, H.; Phan, H.; Herng, T. S.; Gopalakrishna, T. Y.; Zeng, W.; Ding, J.; Wu, J. Conformationally Flexible Bis(9-fluorenylidene)porphyrin Diradicaloids. *Angew. Chem. Int. Ed.* **2017**, *56*, 13484–13488. (e) Wang, J.; Xu, X.; Phan, H.; Herng, T. S.; Gopalakrishna T. Y.; Li, G.; Ding, J.; Wu, J. Stable Oxindolyl-Based Analogues of Chichibabin's and Müller's Hydrocarbons. *Angew. Chem. Int. Ed.* **2017**, *56*, 14154–14158.

(4) (a) Ma, J.; Liu, J.; Baumgarten, M.; Fu, Y.; Tan, Y.-Z.; Schellhammer, K. S.; Ortmann, F.; Cuniberti, G.; Komber, H.; Berger, R.; Müllen, K.; Feng, X. A Stable Saddle-Shaped Polycyclic Hydrocarbon with an Open-Shell Singlet Ground State. *Angew. Chem. Int. Ed.* **2017**, *56*, 3280–3284. (b) Hsieh, Y.-C.; Wu, C.-F.; Chen, Y.-T.; Fang, C.-T.; Wang, C.-S.; Li, C.-H.; Chen, L.-Y.; Cheng, M.-J.; Chueh, C.-C.; Chou, P.-T.; Wu, Y.-T. 5,14-Diaryldiindeno[2,1□f:1′,2′-j]picene: A New Stable [7]Helicene with a Partial Biradical Character. *J. Am. Chem. Soc.* **2018**, *140*, 14357–14366. (c) Ravat, P.; Šolomek, T.; Haussinger, D.; Blacque, O.; Juríček, M. Dimethylcethrene: A Chiroptical Diradicaloid Photoswitch. *J. Am. Chem. Soc.* **2018**, *140*, 10839–10847.

(5) (a) Nobusue, S.; Miyoshi, H.; Shimizu, A.; Hisaki, I.; Fukuda, K.; Nakano, M.; Tobe, Y. Tetracyclopenta[def,jkl,pqr,vwx]tetraphenylene: A Potential Tetraradicaloid Hydrocarbon. *Angew. Chem., Int. Ed.* **2015**, *54*, 2090–2094. (b) Das, S.; Herng, T. S.; Zafra, J. L.; Burrezo, P. M.; Kitano, M.; Ishida, M.; Gopalakrishna, T. Y.; Hu, P.; Osuka, A.; Casado, J.; Ding, J.; Casanova, D.; Wu, J. Fully Fused Quinoidal/aromatic Carbazole Macrocycles with Poly-radical Characters. *J. Am. Chem. Soc.* **2016**, *138*, 7782–7790. (c) Lu, X.; Lee, S.; Hong, Y.; Phan, H.; Gopalakrishna, T. Y.; Herng, T. S.; Tanaka, T.; Sandoval-Salinas, M. E.; Zeng, W.; Ding, J.; Casanova, D.; Osuka, A.; Kim, D.; Wu, J. Fluorenyl Based Macrocyclic Polyradicaloids. *J. Am. Chem. Soc.* **2017**, *139*, 13173–13183. (d) Liu, C.; Sandoval-Salinas, M. E.; Hong, Y.; Gopalakrishna, T. Y.; Phan, H.; Aratani, N.; Herng, T. S.; Ding, J.; Yamada, H.; Kim, D.; Casanova, D.; Wu, J. Macrocyclic Polyradicaloids with Unusual Super-ring Structure and Global Aromaticity. *Chem* **2018**, *4*, 1586–1595. (e) Lu, X.; Gopalakrishna, T. Y.; Phan, H.; Herng, T. S.; Jiang, Q.; Liu, C.; Li, G.; Ding, J.; Wu, J. Global Aromaticity in Macrocyclic Cyclopenta-fused Tetraphenanthrenylene Tetraradicaloid and Its Charged Species. *Angew. Chem. Int. Ed.* **2018**, *57*, 13052–13056. (f) Rana, A.; Hong, Y.; Gopalakrishna, T. Y.; Phan, H.; Herng, T. S.; Yadav, P.; Ding, J.; Kim, D.; Wu, J. Stable Expanded Porphycene-Based Diradicaloid and Tetraradicaloid. *Angew. Chem. Int. Ed.* **2018**, *57*, 12534–12537. (g) Ni, Y.; Sandoval-Salinas, M. E.; Tanaka, T.; Phan, H.; Herng, T. S.; Gopalakrishna, T. Y.; Ding, J.; Osuka, A.; Casanova, D.; Wu, J. [n]Cyclo-para-biphenylmethine Polyradicaloids: [n]Annulene Analogs and Unusual Valence Tautomerization. *Chem* **2019**, *5*, 108–121. (h) Ni, Y; Gopalakrishna, T. Y.; Wu, S.; Wu, J. A Stable All-Thiophene-Based Core-Modified [38]Octaphyrin Diradicaloid: Conformation and Aromaticity Switch at Different Oxidation States. *Angew. Chem., Int. Ed.* **2020**, *59*, 7414–7418.

(6) (a) Gu, X.; Gopalakrishna, T. Y.; Phan, H.; Ni, Y.; Herng, T. S.; Ding, J.; Wu, J. A Three-Dimensional π-conjugated Diradical Molecular Cage. *Angew. Chem. Int. Ed.* **2017**, *56*, 15383–15387. (b) Ni, Y.; Gopalakrishna, T. Y.; Phan, H.; Kim, T.; Herng, T. S.; Han, Y.; Tao, T.; Ding, J.; Kim, D.; Wu, J. 3D global aromaticity in a fully conjugated diradicaloid cage at different oxidation states. *Nat. Chem.* **2020**, *12*, 242–248. (c) Li, G.; Matsuno, T.; Han, Y.; Phan, H.; Wu, S.; Jiang, Q.; Zou, Y.; Isobe, H.; Wu, J. Benzidine/Quinoidal-Benzidine Linked, Superbenzene Based π-Conjugated Chiral Macrocycles and Cyclophanes. *Angew. Chem. Int. Ed.* **2020**, *59*, 9727–9735.

(7) Wu, S.; Li, M.; Phan, H.; Wang, D.; Herng, T. S.; Ding, J.; Lu, Z.; Wu, J. Toward π-Conjugated 2D Covalent Organic Radical Frameworks. *Angew. Chem. Int. Ed.* **2018**, *57*, 8007–8011.

(8) Tschitschibabin, A. E. Über einige phenylierte Derivate des *p, p*-Ditolyls. *Ber. Dtsch. Chem. Ges.* **1907**, *40*, 1810–1819.

(9) Montgomery, L. K.; Huffman, J. C.; Jurczak, E. A.; Grendze, M. P. The Molecular Structures of Thiele's and Chichibabin's Hydrocarbons. *J. Am. Chem. Soc.* **1986**, *108*, 6004–6011.

(10) (a) Hanfland, M.; Brillante, A.; Syassen, K.; Stamm, M.; Fink, J. Polyparaphenylene under pressure: Optical absorption and vibrational modes. *J. Chem. Phys.* **1989**, *90*, 1930–1934. (b) Alvarez, M. P.; Burrezo, P. M.; Kertesz, M.; Iwamoto, T.; Yamago, S.; Xia, J.; Jasti, R.; Navarrete, J. T. L.; Taravillo, M.; Baonza, V. G.; Casado, J. Properties of Sizeable [n] Cycloparaphenylenes as Molecular Models of Single-Wall Carbon Nanotubes Elucidated by Raman Spectroscopy: Structural and Electron-Transfer Responses under Mechanical Stress. *Ang. Chem. Int. Ed.* **2014**, *53*, 7033–7037. (c) Qiu, L.; Peña-Alvarez, M.; Taravillo, M.; Evans, P. J.; Darzi, E.R.; Jasti, R.; Mayorga Burrezo, P.; López Navarrete, J. T.; Baonza, V. G.; Casado, J.; Kertesz, M. High-Pressure Chemistry and the Mechanochemical Polymerization of [5]-Cyclo-*p*-phenylene. *Chem. Eur. J.* **2017**, *23*, 16593–16604. (d) Qiu, L.; Peña-Alvarez, M.; Taravillo, M.; Baonza, V. G.; Casado, J.; Kertesz, M. Mechanochemistry in [6]Cycloparaphenylene: A Combined Raman Spectroscopy and Density Functional Theory Study. *Chem. Phys. Chem.* **2018**, *19*, 1903–1916. (e) Peña-Alvarez, M.; Qiu, L.; Baonza, V.G.; Taravillo, M.; Kertesz, M. Casado, Molecules under Pressure: The Case of [n]Cycloparaphenylenes. *Chem. Mater.* **2019**, *31*, 6443–6452. (f) Peña-Álvarez, M.; Fanetti, S.; Falsini, N.; Novelli, G.; Casado, J.; Valentín G. Baonza, V. G.; Taravillo, M.; Parsons, S.; Bini, R.; Citroni, M. Linear, Non-Conjugated Cyclic and Conjugated Cyclic Paraphenylene under Pressure. *Molecules* **2019**, *24*, 3496–3517.

(11) (a) Tashiro, K.; Aida, T.; Zheng, J.-Y.; Kinbara, K.; Saigo, K.; Sakamoto, S.; Yamaguchi, K. A Cyclic Dimer of Metalloporphyrin Forms a Highly Stable Inclusion Complex with C_{60}. *J. Am. Chem. Soc.* **1999**, *121*, 9477–9478. (b) Sun, D.; Tham, F. S.; Reed, C. A.; Chaker, L.; Burgess, M.; Boyd, P. D. W. Porphyrin-Fullerene Host-Guest Chemistry. *J. Am. Chem. Soc.*

2000, *122*, 10704–10705. (c) Shoji, Y.; Tashiro, K.; Aida, T. Selective Extraction of Higher Fullerenes Using Cyclic Dimers of Zinc Porphyrins. *J. Am. Chem. Soc.* **2004**, *126*, 6570–6571. (d) Shoji, Y.; Tashiro, K.; Aida, T. Selective Extraction of Higher Fullerenes Using Cyclic Dimers of Zinc Porphyrins. *J. Am. Chem. Soc.* **2004**, *126*, 6570–6571. (e) Cui, S.; Zhuang, G.; Lu, D. Huang, Q.; Jia, H.; Wang, Y.; Yang, S.; Du, P. A Three-Dimensional Capsule-like Carbon Nanocage as a Segment Model of Capped Zigzag [12,0] Carbon Nanotubes: Synthesis, Characterization, and Complexation with C_{70}. *Angew. Chem. Int. Ed.* **2018**, *57*, 9330–9335. (f) Shi, Y.; Cai, K.; Xiao, H.; Liu, Z.; Zhou, J.; Shen, D.; Qiu, Y.; Guo, Q.-H.; Stern, C.; Wasielewski, M. R.; Diederich, F.; Goddard, III, W. A.; Stoddart, J. F. Selective Extraction of C_{70} by a Tetragonal Prismatic Porphyrin Cage. *J. Am. Chem. Soc.* **2018**, *140*, 13835–13842.

(12) Wang, Q.; Zhang, C.; Noll, B. C.; Long, H.; Jin, Y.; Zhang, W. A Tetrameric Cage with D_{2h} Symmetry through Alkyne Metathesis. *Angew. Chem. Int. Ed.* **2014**, *53*, 10663–10667.

(13) Song, J.; Aratani, N.; Shinokubo, H.; Osuka, A. A Porphyrin Nanobarrel That Encapsulates C_{60}. *J. Am. Chem. Soc.* **2010**, *132*, 16356–16357.

(14) Matsui, K., Segawa, Y.; Itami, K. All-benzene carbon nanocages: sizeselective synthesis, photophysical properties, and crystal structure. *J. Am. Chem. Soc.* **2014**, *136*, 16452–16458.

(15) Kayahara, E.; Iwamoto, T.; Takaya, H.; Suzuki, T.; Fujitsuka, M.; Majima, T.; Yasuda, N.; Matsuyama, N.; Seki, S.; Yamago, S. Synthesis and physical properties of a ball-like three-dimensional p-conjugated molecule. *Nat. Commun.* **2013**, *4*, 2694–2700.

(16) Cai, M.; Zhu, M.; Wang, P.; Song, C. Synthesis and Properties of Novel Poly(aryl ether ketone)s Containing Both Diphenyl Moiety and Amide Linkages in The Main Chains. *Polymer* **2010**, *51*, 1293–1300.

(17) Crystallogaphic data for ***l*-Ph4**, ***l*-Ph4^{2+}**, and ***c*-Ph14^{6+}** are deposited in the Cambridge Crystallographic Data Centre (CCDC) with CCDC number 1190471, 1190472, and 1190473, respectively.

(18) Raczyńska, E. D.; Hallman, M.; Kolczyńska, K.; and Stepniewski, T. M. On the harmonic oscillator model of electron delocalization (HOMED) index and its application to heteroatomic π-electron systems. *Symmetry* **2010**, *2*, 1485–1509.

(19) Gasparro, F. P.; Kolodny, N. H. NMR Determination of The Rotational Barrier in *N*,*N*-Dimethylacetamide. A Physical Chemistry Experiment. *J. Chem. Edu.* **1977**, *54*, 258–261.

(20) Bleaney, B.; Bowers, K. D. Anomalous Paramagnetism of Copper Acetate. *Proc. R. Soc. London Ser. A* **1952**, *214*, 451–465.

(21) (a) Casado, J.; Patchkovskii, S.; Zgierski, M. Z.; Hermosilla, L.; Sieiro, C.; Moreno Oliva, M.; López Navarrete, J.T. Raman Detection of "Ambiguous" Conjugated Biradicals: An Extended Viologen Undergoing Rapid Thermal Singlet-to-Triplet Intersystem Crossing. *Angew. Chem. Int. Ed.* **2008**, *47*, 1443-1446. (b) Mayorga Burrezo, P.; Zafra, J.L.; López Navarrete, J.T.; Casado, J., Quinoidal/Aromatic transformations in π–conjugated oligomers: Vibrational Raman studies on the limits of rupture for π–bonds. *Angew. Chem. Int. Ed.* **2017**, *56*, 2250-2259. (c) Mayorga Burrezo, P.; Lin, N.-T.; Nakabayashi, K.; Ohkosh, S.; Calzado, E.M.; Boj, P.G.; Díaz García, M.A.; Franco, C.; Rovira, C.; Veciana, J.; Moos, M.; Lambert, C.; López Navarrete, J.T.; Tsuji, H.; Nakamura, E.; Casado, J. Bis(Aminoaryl) Carbon-Bridged Oligo(phenylenevinylene)s Expand the Limits of Electronic Couplings. *Angew. Chem. Int. Ed.* **2017**, *56*, 2898-2902.

(22) (a) Conners, K. A. Binding Constants: The Measurement of Molecular Complex Stability; Wiley-VCH: New York, **1987**. (b) Yu, G.; Zhou, X.; Zhang, Z.; Han, C.; Mao, Z.; Gao, C.; Huang, F. Pillar[6]arene/Paraquat Molecular Recognition in Water: High Binding Strength, pH-Responsiveness, and Application in Controllable Self-Assembly, Controlled Release, and Treatment of Paraquat Poisoning. *J. Am. Chem. Soc.* **2012**, *134*, 19489–19497.

Graphical abstract entry:

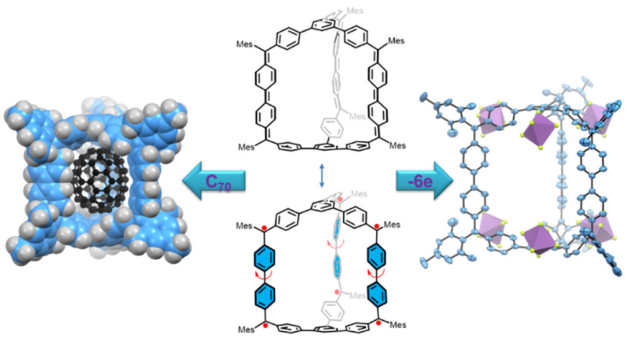

Supporting Information for

A Chichibabin's Hydrocarbon Based Molecular Cage: The Impact of Structural Rigidity on Dynamics, Stability, and Electronic Properties

Yong Ni, Fernando Gordillo-Gámez, Miriam Peña Alvarez, Zhihan Nan, Zhengtao Lin, Shaofei Wu, Yi Han, Juan Casado, and Jishan Wu**

Table of Contents

1. Experiment section

1.1 General

All reagents and starting materials were obtained from commercial suppliers and used without further purification unless otherwise noted. Anhydrous toluene and THF were distilled from sodium-benzophenone immediately prior to use. Anhydrous dichloromethane (DCM) was distilled from CaH_2. All reaction conditions dealing with air and moisture sensitive compounds were carried out in a dry reaction vessel under nitrogen atmosphere. All the other chemicals were reagent grade and used without any further purification. Flash silica gel column chromatography was performed on silica gel 60N (spherical and neutral gel, 40-50 μm, Kanto), and gel permeation chromatography (GPC) was performed on JAI LC-9104 systems equipped with UV and RI detectors using JAI GEL 1H-40, 2H-40 and 2.5H-40 columns (eluent: $CHCl_3$). The ^1H NMR and ^{13}C NMR spectra were recorded in solution of DMSO-d_6, $CDCl_3$, CD_2Cl_2 or THF-d_8 on DRX 500 NMR spectrometers. All chemical shifts are quoted in ppm, relative to tetramethylsilane, using the residual solvent peak as a reference standard. The following abbreviations were used to explain the multiplicities: s = singlet, d = doublet. Atmospheric Pressure Chemical Ionization Mass Spectrometry (APCI MS) measurements were performed on a Finnigan TSQ 7000 triple stage quadrupole mass spectrometer. UV-vis-NIR absorption spectra were recorded on a Shimadzu UV-3600 spectrophotometer. Cyclic voltammetry (CV) and differential pulse voltammetry measurements were performed in dry DCM on a CHI 620C electrochemical analyzer with a three-electrode cell, using 0.1 M *n*-Bu_4NPF_6 as supporting electrolyte, AgCl/Ag as reference electrode, gold disk as working electrode, Pt wire as counter electrode, with scan rate was at 50 mV/s for CV. The potential was externally calibrated against the ferrocene/ferrocenium couple. Continuous wave X-band ESR spectra were obtained with a JEOL (FA200) spectrometer using a variable temperature liquid nitrogen cryostat. The VT ESR data of ***c*-Ph14** and ***l*-Ph4** in the frozen THF solutions were fitted by Bleaney-Bowers equation,

$$IT = \frac{C}{k_B[3 + exp(-2J/k_BT)]}$$

where C is a constant and $-2J$ is correlated to the excitation energy from the ground state to the first triplet excited state.

Raman Spectroscopy. The Raman spectra of the neutral and oxidized species were recorded by using the 532 nm excitation of a Bruker Senterra Raman microscope by averaging spectra during 50 min with a resolution of 3–5 cm^{-1}. A CCD camera operating at –50 ºC was used. The spectra were collected using the 1 × 1 camera of the mentioned microscope.

Variable pressure Raman Spectroscopy. Pressure dependent Raman measurements were conducted with an Invia Reflex Raman RENISHAW microscope with 785 nm as excitation wavelength with a spectral resolution of 0.5-1 cm^{-1} (1800 gr/mm). High pressure studies were conducted in a screw-driven diamond anvil cell (DAC) with ultra-low fluorescence diamonds and culet size 250 μm. Rhenium gasket 25 μm thick with a gasket hole of 80 μm was used. No pressure transmitting medium was used and the shift of the diamond was use as the pressure calibrant. The recovered samples, after pressure cycles, were also analyzed, taking several spectra on different sample points to confirm the reproducibility on the same sample and to ensure whether the transformation of the samples is complete or not.

UV-Vis-NIR spectroelectrochemistry. In situ UV-Vis-NIR spectroelectrochemical studies were conducted on the Cary 5000 spectrophotometer. A C3 epsilon potentiostat from BASi was used for the electrolysis using a thin layer cell from a demountable omni cell from Specac. In this cell a three electrodes system was coupled to conduct in situ spectroelectrochemistry. A Pt gauze was used as the working electrode, a Pt wire was used as the counter electrode, and an Ag wire was used as the pseudo-reference electrode. The spectra were collected a constant potential electrolysis and the potentials were changed in interval of 15 mV. The electrochemical medium used was 0.1 M TBA-PF6 in fresh distilled CH_2Cl_2, at room temperature with sample concentrations of 10^{-3} M.

1.2. Synthetic procedure and characterization data

Compound **6** was synthesized by following the reported procedure.[1]

Synthesis of compound 3:

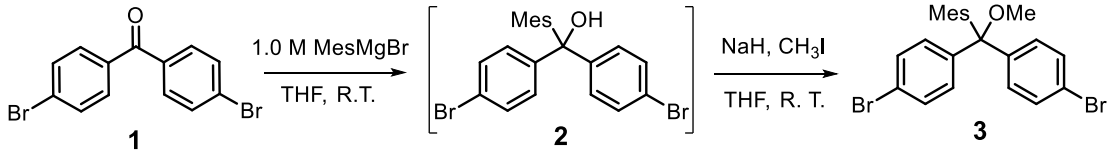

4,4′-Dibromobenzophenone **1** (2.42 g, 5.40 mmol) was dissolved in 100 mL of degassed anhydrous THF. 2-Mesitylmagnesiumbromide (MesMgBr) solution (1.0 M, 6.0 mL, 1.11 eq) was added dropwise at room temperature (R. T.), and the reaction mixture was allowed to stir for 4 hours. After quenching by water and extracted with diethyl ether (3 × 60 mL), the organic phase was collected and dried over Na_2SO_4. The organic solvent was then removed by rotary evaporation and the residue was dried under vacuum, which was then used for the next step reaction without any purification.

The residue was re-dissolved in anhydrous THF (60 mL), and NaH (60% in mineral oil, 432 mg, 10.8 mmol, 2.0 eq) was added at 0 °C. After stirring for 30 min, CH_3I solution (2.0 M in *tert*-butyl methyl ether, contains copper as stabilizer, *Sigma-Aldrich*, 4.05 ml, 1.5 eq) was added at 0 °C under nitrogen atmosphere. The reaction mixture was stirred at room temperature overnight and then carefully quenched with H_2O (10 mL), extracted with diethyl ether (3 × 60 mL). The organic layer was washed with brine, dried over Na_2SO_4, and concentrated in vacuo. The residue was purified by column chromatography (hexanes/DCM = 1:0 to 6:1) to afford compound **3** (2.91 g, 86%) as a light yellow solid. ^{1}H NMR (500 MHz, DMSO-d_6): δ ppm 7.45 (d, J = 8.3 Hz, 4H), 7.19 (d, J = 8.3 Hz, 4H), 6.85 (s, 2H), 3.14 (s, 3H), 2.22 (s, 3H), 1.74 (s, 6H). ^{13}C NMR (126 MHz, DMSO): δ ppm 145.50, 138.88, 136.53, 134.41, 131.50, 130.92, 128.68, 119.68, 86.44, 51.58, 24.06, 20.05. HR-MS (APCI): m/z = 440.9847 $[M\text{-}OMe]^+$, calcd. for $C_{22}H_{19}Br_2$, 440.9848, the methyloxyl group was removed during HR-Mass characterization in positve mode.

Synthesis of compound 4:

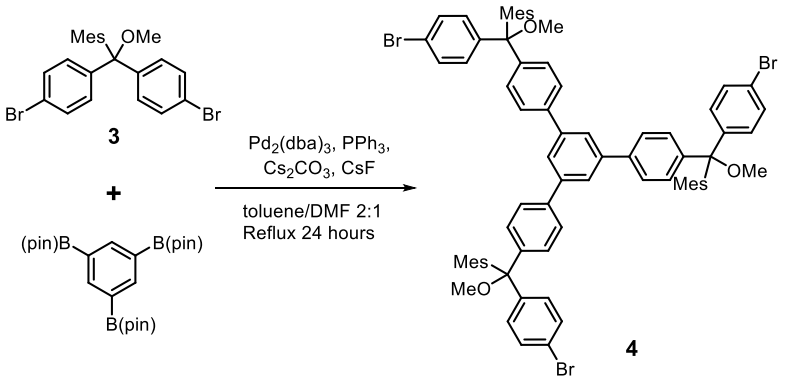

A solution of 1,3,5-phenyltriboronic acid, tris(pinacol)ester (500 mg, 1.1 mmol), **3** (4.72 g, 10 mmol, 9 eq), $Pd_2(dba)_3$ (60 mg, 0.066 mmol), PPh_3 (70 mg, 0.26 mmol), Cs_2CO_3 (950 mg, 2.93 mmol), and CsF (450 mg, 2.93 mmol) in toluene/DMF (60 mL/30 mL) was degassed through three freeze-pump-thaw cycles, and the reaction flask was purged with nitrogen. The resulting mixture was stirred at reflux for 24 hours. After cooling down to room temperature, the reaction mixture was diluted with DCM, washed with water and dried over anhydrous sodium sulfate. After evaporation of the solvent, the residue was purified by silica-gel column chromatography (deactivated by triethylamine (TEA)) to give compound **4** as a white solid (759 mg, 55%). ^{1}H NMR (500 MHz, Methylene Chloride-d_2): δ ppm 7.74 (s, 3H), 7.57 (d, J = 8.6 Hz, 6H), 7.40 (dd, J = 8.7, 6.8 Hz, 12H), 7.28 (d, J = 8.7 Hz, 6H), 6.86 (s, 6H), 3.26 (s, 9H), 2.29 (s, 9H), 1.87 (s, 18H). ^{13}C NMR (126 MHz, Methylene Chloride-d_2): δ ppm 146.81, 146.31, 142.18, 140.32, 139.56, 137.48, 136.04, 132.12, 131.51, 129.55, 128.10, 127.31, 125.24, 120.74, 87.84, 52.39, 30.29, 24.88, 20.84 ppm. HRMS (APCI): m/z = 1254.2834 $[M]^+$, calcd. for $C_{75}H_{69}Br_3O_3$, 1254.2791.

Synthesis of compound 5:

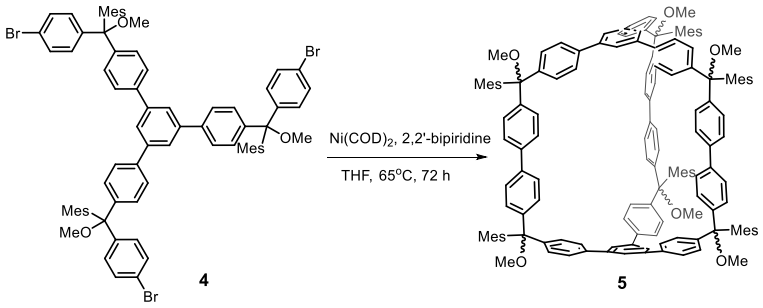

In a nitrogen-filled glove box, $Ni(COD)_2$ (421 mg, 1.53 mmol, 3.3 equiv), 2,2′-bipyridyl (260 mg, 1.67 mmol, 3.3 eq), and anhydrous THF (60 mL) were sequentially

added to a 100 mL glass vial equipped with a stir bar. The vial was sealed with a teflon-lined septum cap, transferred out of glove box, and stirred at 60 °C for 0.5 h. After cooling down to room temperature, the vial was moved back into the glove box. In the glove box, compound **4** (582 mg, 0.46 mmol, 1.0 equiv) and THF (500 mL) were added to a 1.0 L glass heavy-wall pressure vessel equipped with a stirring bar. Next, the content in the 100 mL glass vial was transferred to the pressure vessel *via* syringe. The vessel was capped, transferred out of the glove box, and was stirred at 65 °C for 72 h. The reaction mixture was cooled down to room temperature and filtered through a short pad of silica gel by using 1:2 Hexanes/$CHCl_3$ (300 mL) as eluent. The solvent was removed under reduced pressure, and the residue was further purified by preparative GPC to afford the cage **5** (122 mg, 26%) as a white solid. Due to the existence of multiple isomers, the NMR spectrum of compound **5** is very complicated. HRMS (APCI): *m*/*z* = 2035.0514 $[M]^+$, calcd. for $C_{150}H_{138}O_6$, 205.0488.

Synthesis of compound 7:

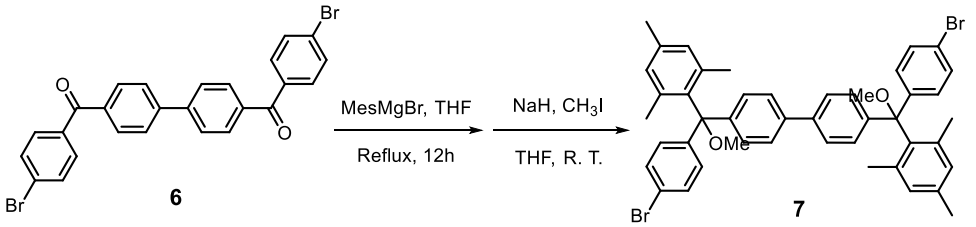

The synthetic procedure was modified a little bit from that of compound **3**. Compound **6** (600 mg, 1.16 mmol) was dispersed in 80 mL of degassed anhydrous THF (the solubility of compound **6** is very poor in common organic solvents). 2-Mesitylmagnesiumbromide (MesMgBr) solution (1.0 M, 4 mL, 3.4 eq) was added dropwise at R. T., and the reaction mixture was stirred at reflux for 12 hours. After quenching by water and extracted with diethyl ether (3 × 60 mL), the organic phase was collected and dried over Na_2SO_4. The organic solvent was then removed by rotary evaporation and the residue was dried under vacuum, which was then used for the next step reaction without any purification.

The residue was re-dissolved in anhydrous THF (60 mL), and NaH (60% in mineral oil, 186 mg, 4.64 mmol, 4.0 eq) was added at 0 °C. After stirring for 30 min, CH_3I solution (2.0 M in *tert*-butyl methyl ether, contains copper as stabilizer, *Sigma-*

Aldrich, 1.8 ml, 3.1 eq) was added at 0 °C under nitrogen atmosphere. The reaction mixture was stirred at room temperature overnight and then carefully quenched with H_2O (10 mL), extracted with diethyl ether (3 × 40 mL). The organic layer was washed with brine, dried over Na_2SO_4, and concentrated in vacuo. The residue was purified by column chromatography (hexanes/DCM = 1:0 to 6:1) to afford compound **7** (748 mg, 82%) as a white solid. ^{1}H NMR (500 MHz, DMSO-d_6): δ ppm 7.54 (d, J = 8.1 Hz, 4H), 7.44 (d, J = 8.2 Hz, 4H), 7.28 (d, J = 8.1 Hz, 4H), 7.22 (d, J = 8.3 Hz, 4H), 6.84 (s, 4H), 3.15 (s, 6H), 2.22 (s, 6H), 1.77 (s, 12H). ^{13}C NMR (126 MHz, $CDCl_3$): δ ppm 145.89, 145.01, 138.94, 137.43, 136.37, 134.97, 131.47, 130.83, 128.80, 127.12, 126.09, 119.54, 86.64, 51.57, 40.01, 24.07, 20.07. HR-MS (APCI): m/z = 755.1513 $[M\text{-}OMe]^+$, calcd. for $C_{45}H_{41}Br_2O$, 755.1519, one methyloxyl group was removed during HR-Mass characterization in positive mode.

General procedure for synthesis of *l*-Ph4 and *c*-Ph14:

Under argon atmosphere, the precursors **5** and **7** with 'OMe' groups (60 mg) was dissolved in a solution of DCM (25 mL), then $SnCl_2$ (170 mg, 0.22 mmol, excess amount) was added. The mixture was stirred at room temperature overnight. After evaporation of the solvent, the residue was purified by flash column chromatography (silica gel pre-deactivated by triethylamine, DCM/Hexane = 1:3 to 1:2) in air to give the corresponding compounds ***l*-Ph4** and ***c*-Ph14**.

Compound ***l*-Ph4**: 52.5 mg, yield 95%.

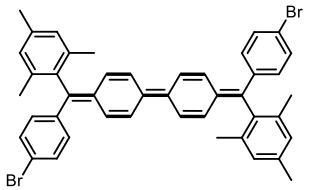

^{1}H NMR (500 MHz, THF-d_8) at 268 K: δ ppm 7.46 (m, 8H), 7.31 (d, J = 9.8 Hz, 2H), 7.20 (d, J = 8.2 Hz, 4H), 6.94 (s, 4H), 6.39 (d, J = 9.7 Hz, 2H), 2.30 (s, 6H), 1.97 (s, 12H). ^{1}H NMR (500 MHz, THF-d_8) at 218 K: δ ppm 7.65 – 7.59 (d, J = 9.9 Hz, 1H), 7.52 (m, 5H), 7.46 – 7.39 (m, 3H), 7.32 (dd, J = 10.0, 2.1 Hz, 1H), 7.21 (m, 4H), 6.98 (m, 4H), 6.45 – 6.32 (d, J = 8.5, 2H), 2.31 (m, 6H), 1.97 (m, 12H). HR-MS (APCI): m/z = 725.1393 $[M+H]^+$, calcd. for $C_{44}H_{39}Br_2$, 725.1413.

Compound ***c*-Ph14**: 49.6 mg, yield 91%.

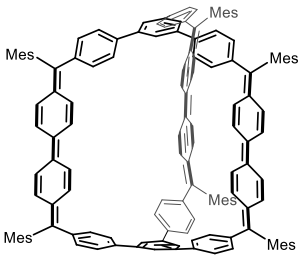

^{1}H NMR (500 MHz, THF-d_8) at 275 K: δ ppm 7.95 (s, 6H), 7.85 (d, J = 8.0 Hz, 12H), 7.34 (d, J = 8.0 Hz, 12H), 7.19 (s, 6H), 7.14 (d, J = 10.3 Hz, 6H), 6.97 (s, 12H), 6.84 (d, J = 10.2 Hz, 6H), 6.40 (d, J = 9.8 Hz, 6H), 2.32 (s, 18H), 2.14 (s, 36H). HR-MS (APCI): m/z = 1848.9421 $[M]^+$, calcd. for $C_{144}H_{120}$, 1848.9385.

2. Additional spectra

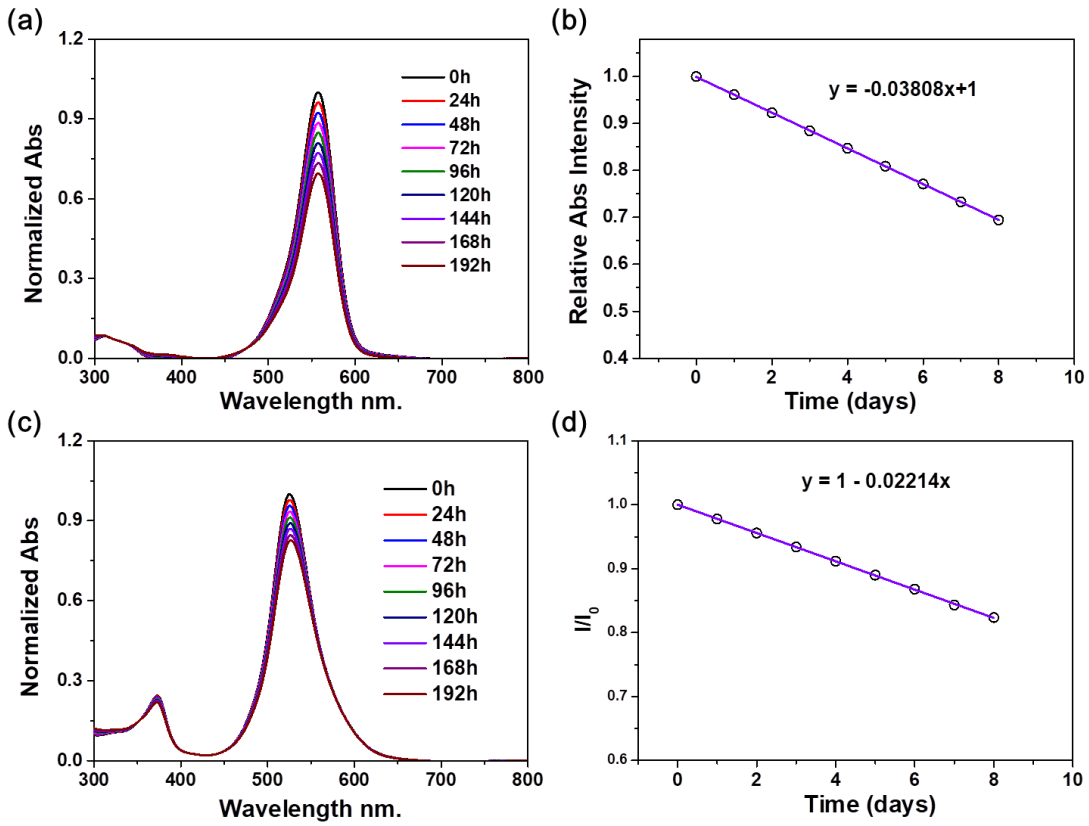

Figure S1. Photo-stability test of (a) ***l*-Ph4** and (c) ***c*-Ph14** under ambient white light and air condition in DCM. The decay of the absorbance at absorption maximum was plotted with time, and the half-life time ($t_{1/2}$) can be determined to be 13.1 and 22.6 days for (b) ***l*-Ph4** and (d) ***c*-Ph14**, respectively.

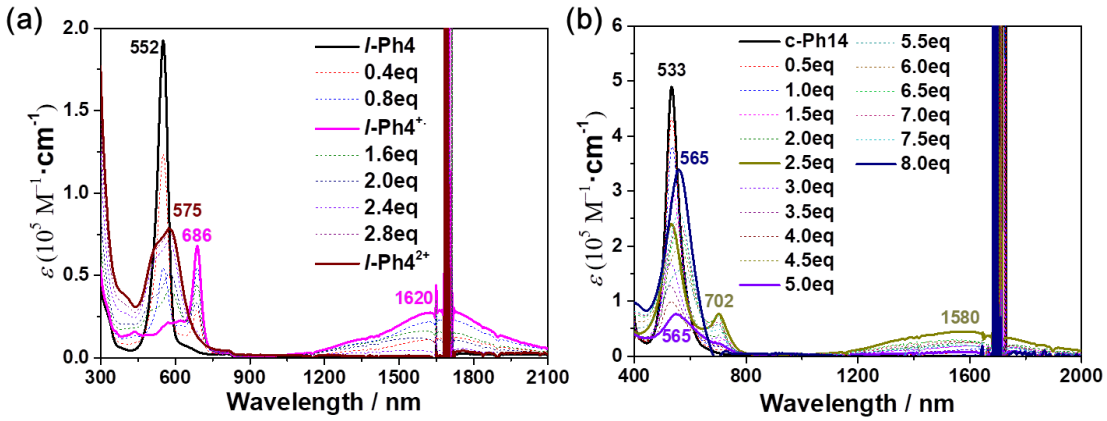

Figure S2. Change of the UV-vis-NIR absorption spectra of (a) ***l*-Ph4** and (b) ***c*-Ph14** in dry DCM upon oxidative titration with NO•SbF_6 (dissolved on minimal amount of dry acetonitrile). ***l*-Ph4** can reach two oxidation states which can be assigned to radical cation and dication. For ***c*-Ph14**, the intermediate states can't be fully assigned, but the final state should be assigned to hexacation.

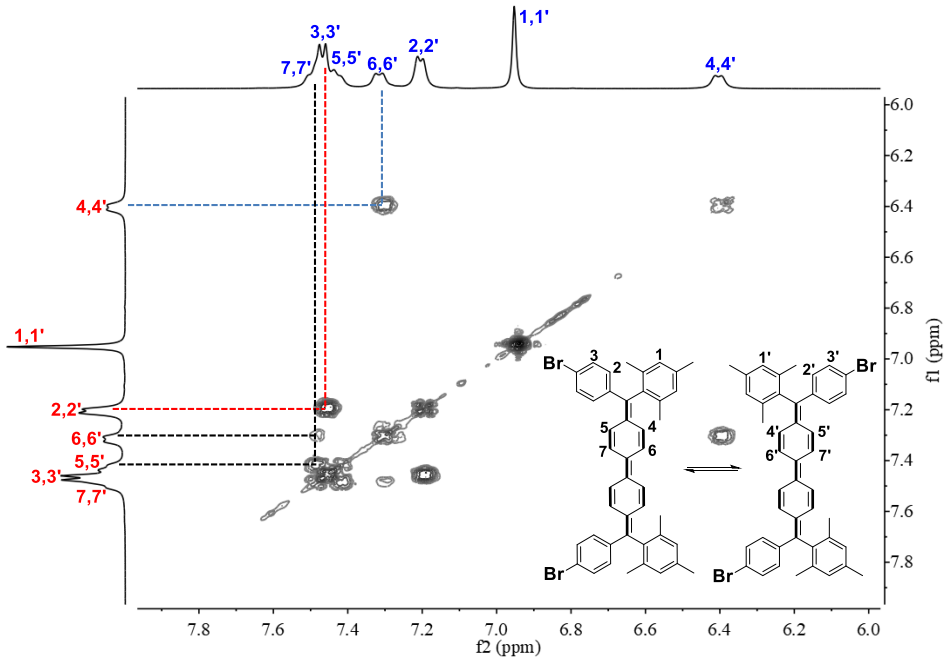

Figure S3. 2D COSY NMR spectrum (aromatic region) of ***l*-Ph4** in THF-d_8 at 268 K with the assignment.

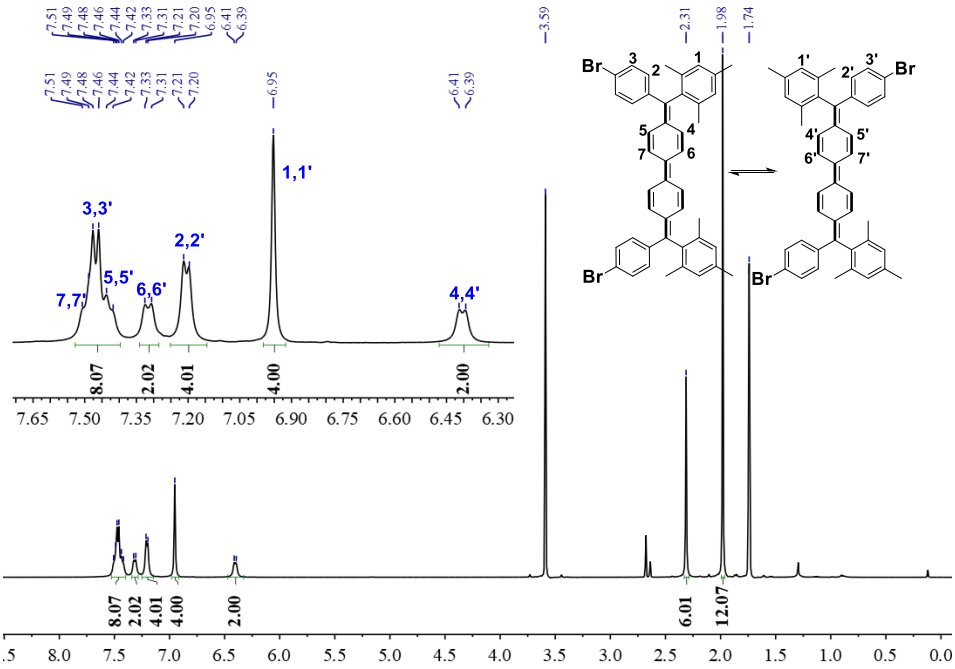

Figure S4. ^{1}H NMR spectrum of ***l*-Ph4** in THF-d_8 at 268 K with the assignment and integration.

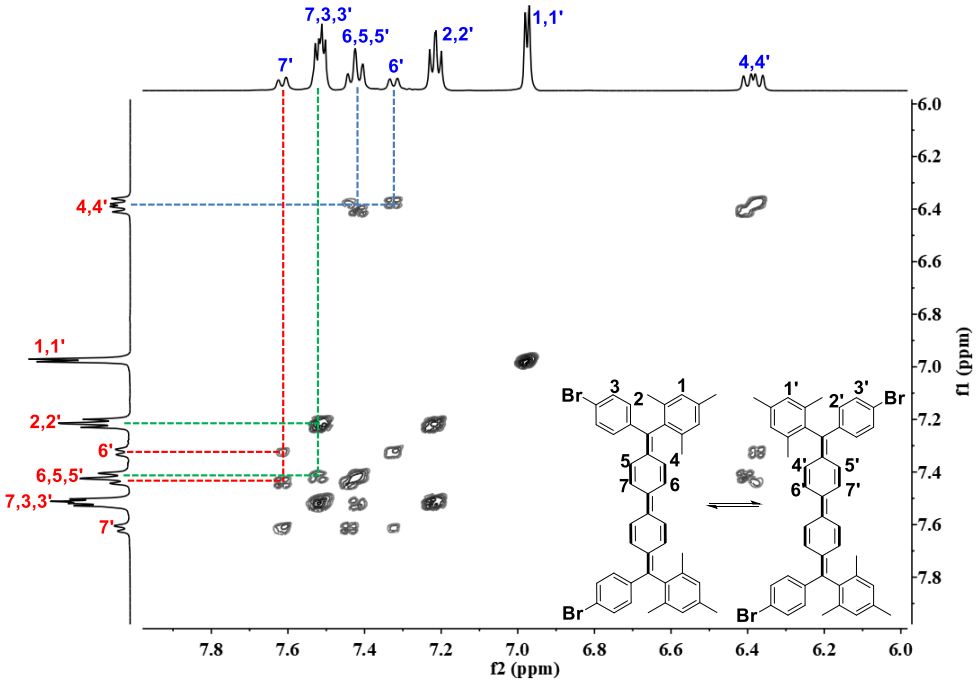

Figure S5. 2D COSY NMR spectrum (aromatic region) of ***l*-Ph4** in THF-d_8 at 218 K with the assignment.

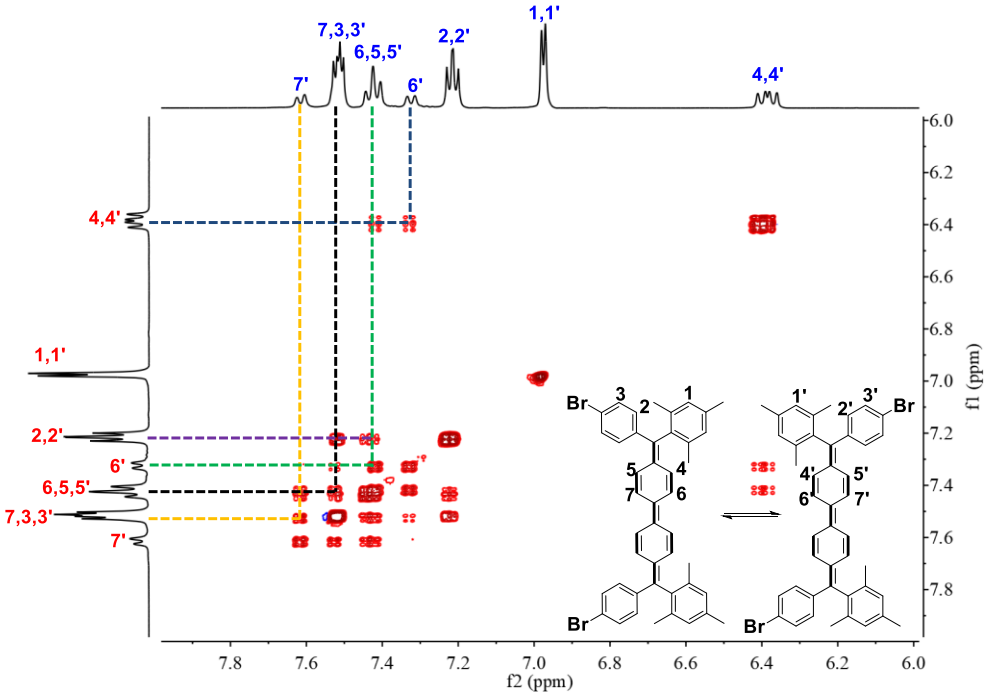

Figure S6. 2D NOESY NMR spectrum (aromatic region) of ***l*-Ph4** in THF-d_8 at 218 K with the assignment. The red/blue cross peaks represent positive/negative signal, respectively, and the positive cross peaks come from dynamic exchange, not from normal NOE.

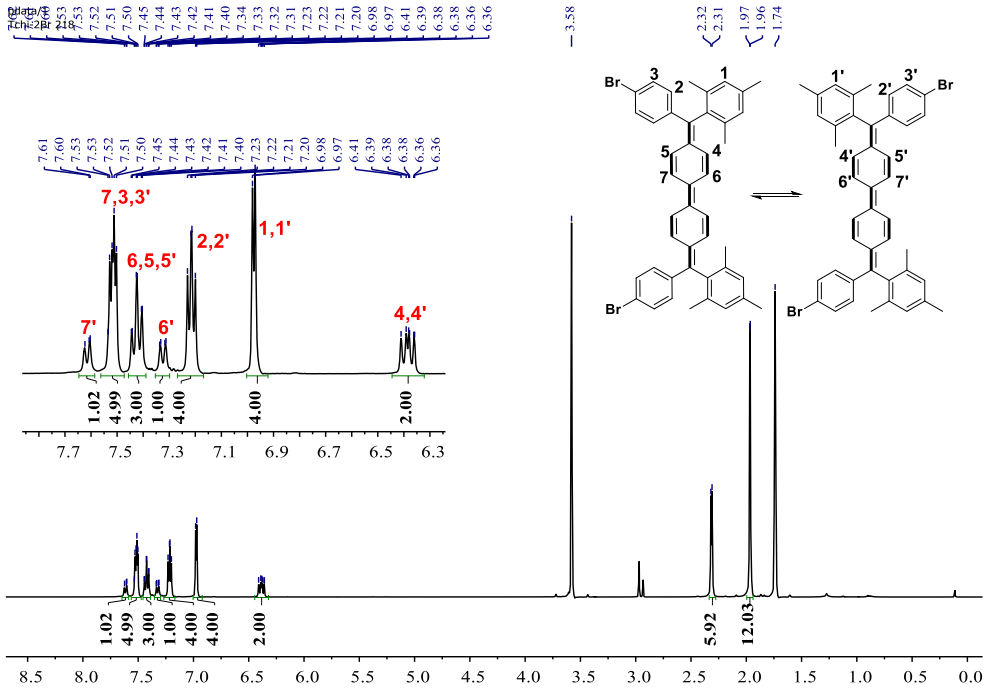

Figure S7. ^{1}H NMR spectrum of ***l*-Ph4** in THF-d_8 at 268 K with the assignment and integration.

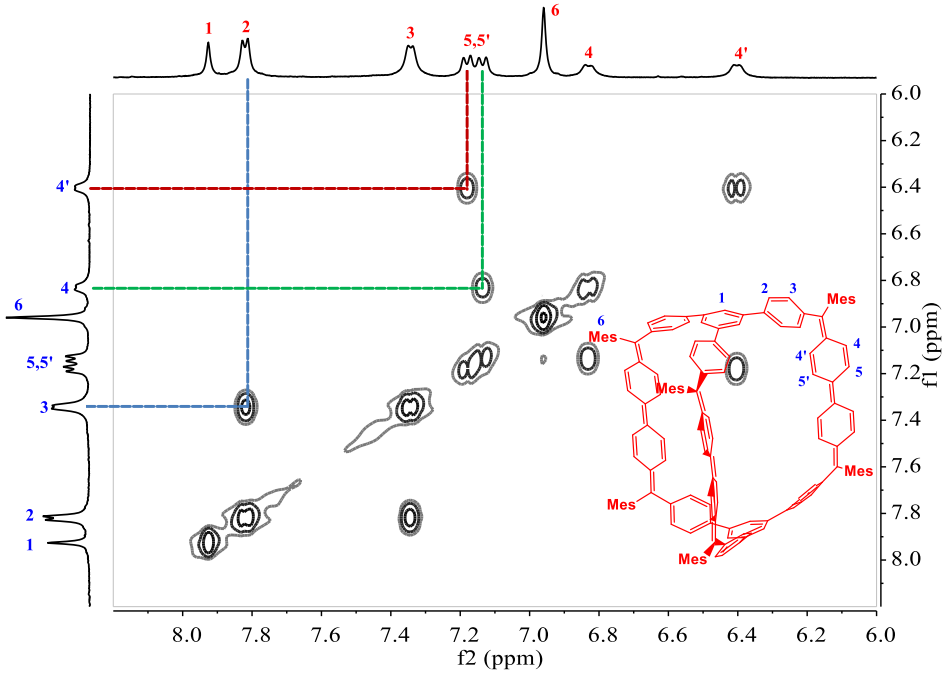

Figure S8. 2D COSY NMR spectrum (aromatic region) of ***c*-Ph14** in THF-d_8 at 295 K with the assignment.

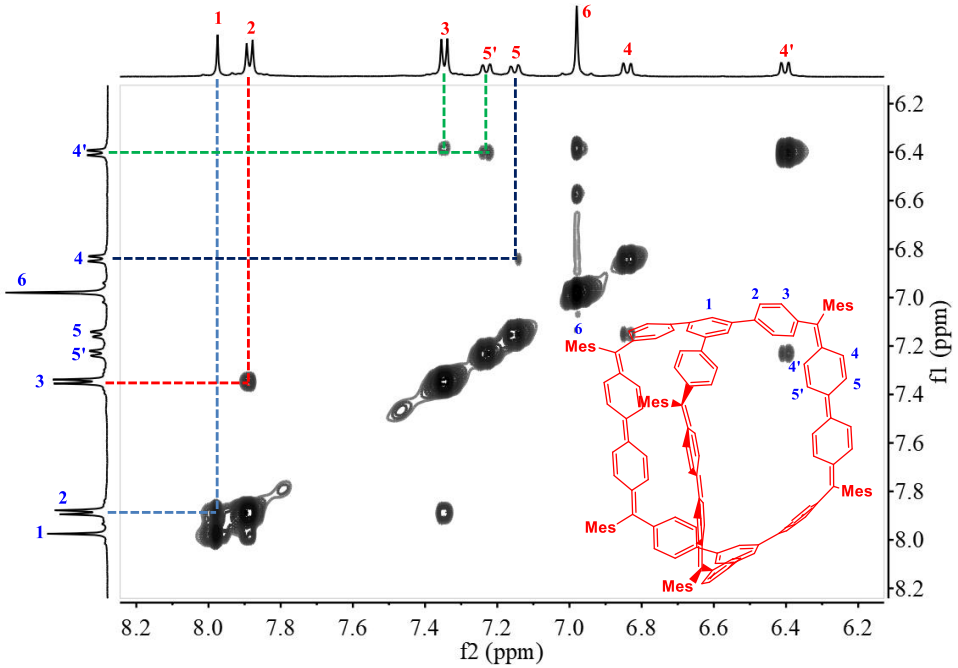

Figure S9. 2D NOESY NMR spectrum of ***c*-Ph14** in THF-d_8 at 275 K with the assignment.

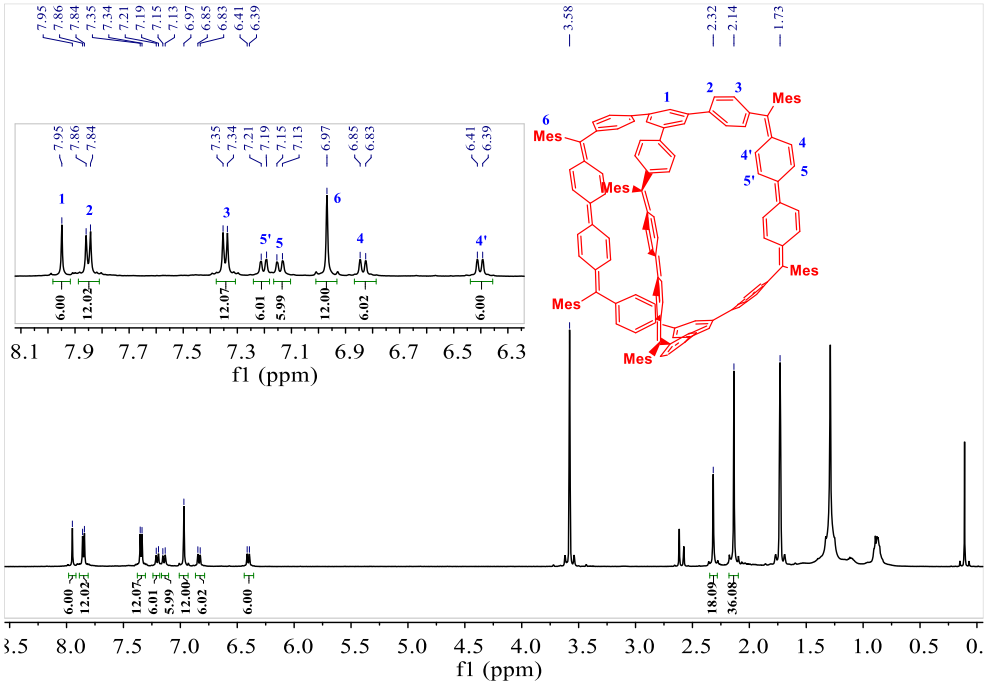

Figure S10. ^{1}H NMR spectrum of ***c*-Ph14** in THF-d_8 at 275 K with the assignment and integration.

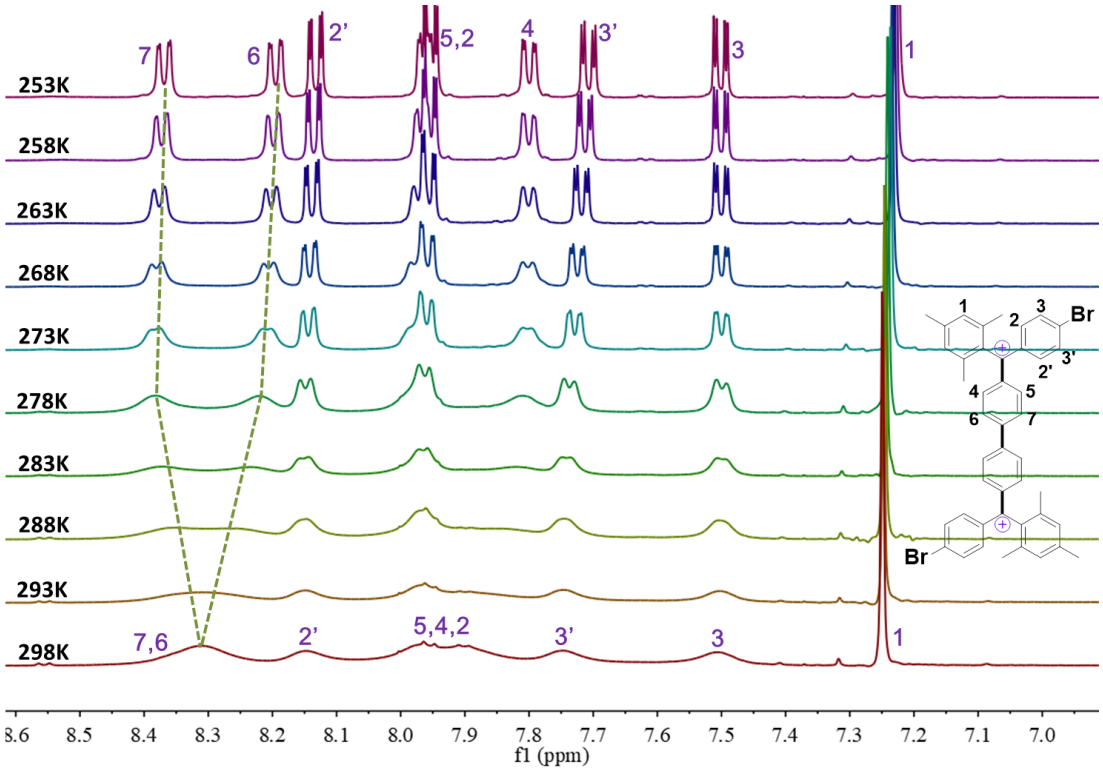

Figure S11. Variable temperature (298 K-253 K) ^{1}H NMR spectra of ***l*-Ph4^{2+}** (aromatic region) in CD_2Cl_2 with the assignment.

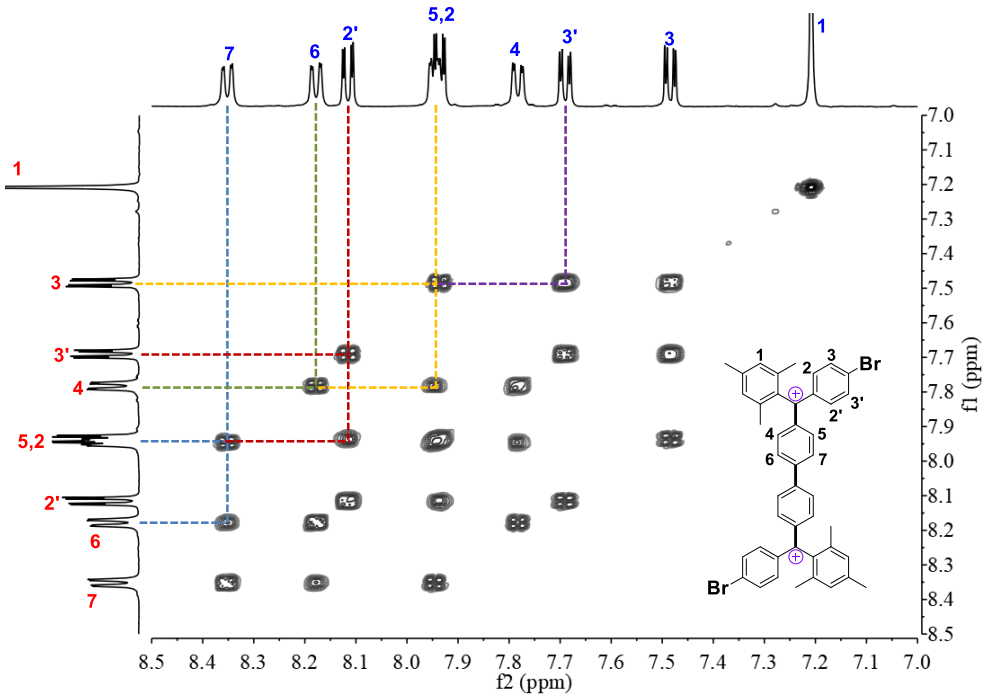

Figure S12. 2D COSY NMR spectrum (aromatic region) of ***l*-Ph4**$^{2+}$ in CD_2Cl_2 at 253K with the assignment.

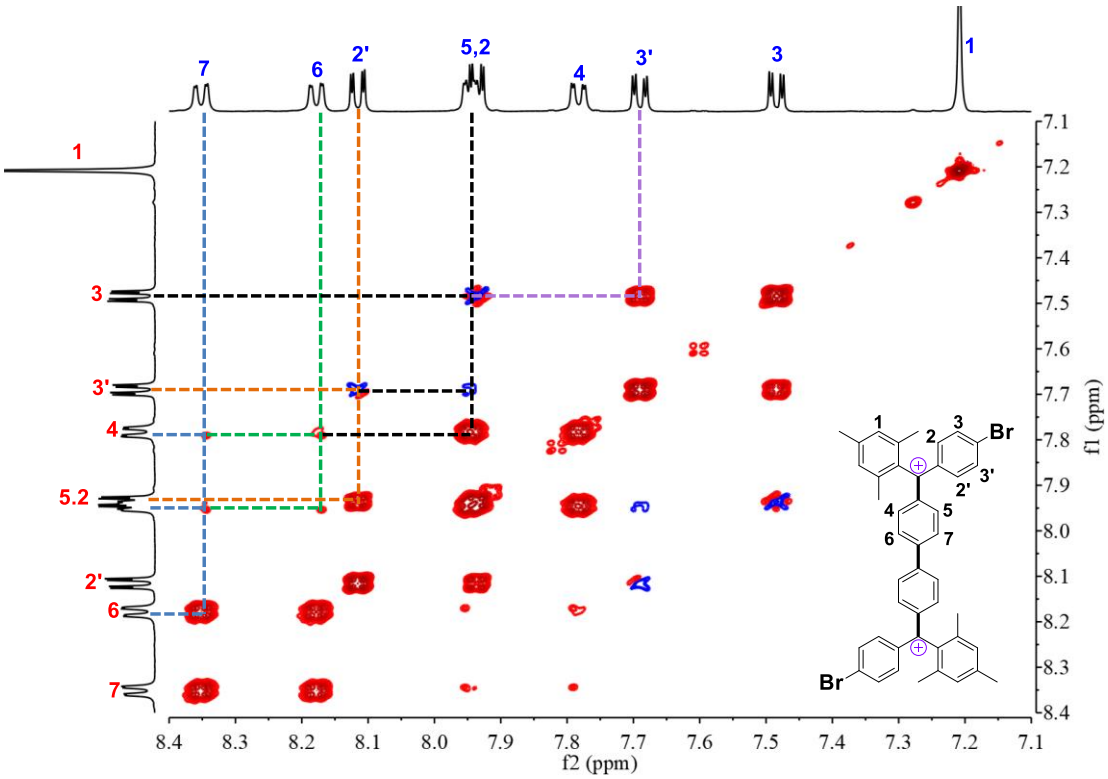

Figure S13. 2D NOESY NMR spectrum (aromatic region) of ***l*-Ph4**$^{2+}$ in CD_2Cl_2 at 253 K with the assignment. The red/blue cross peaks represent positive/negative signal, respectively, and the positive cross peaks come from dynamic exchange, not from normal NOE.

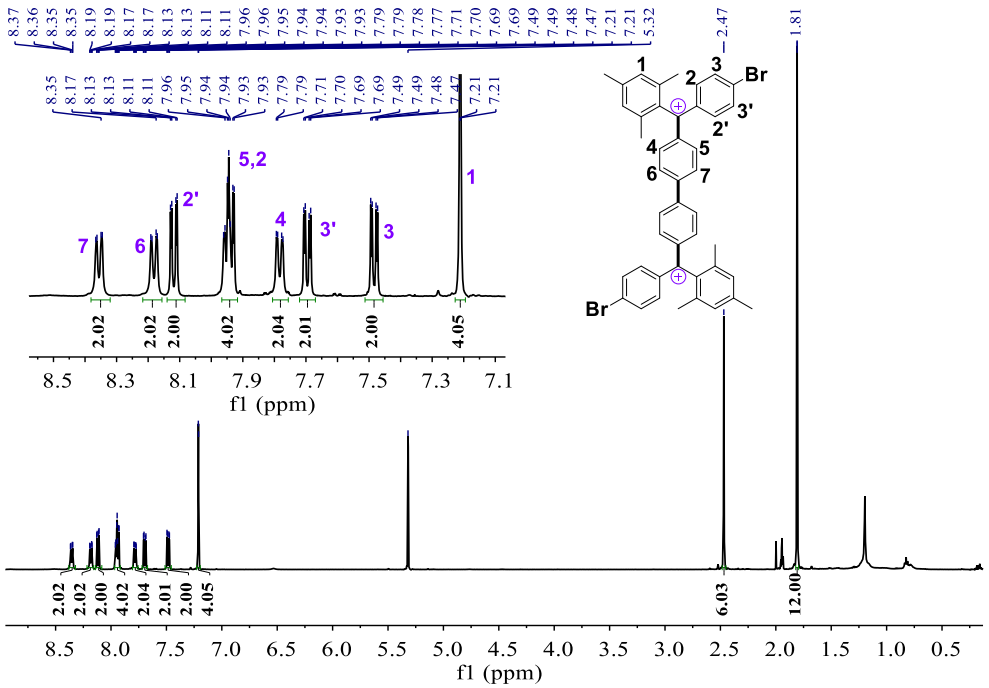

Figure S14. ^{1}H NMR spectrum of ***l*-Ph4^{2+}** in CD_2Cl_2 at 253 K with the assignment and integrations.

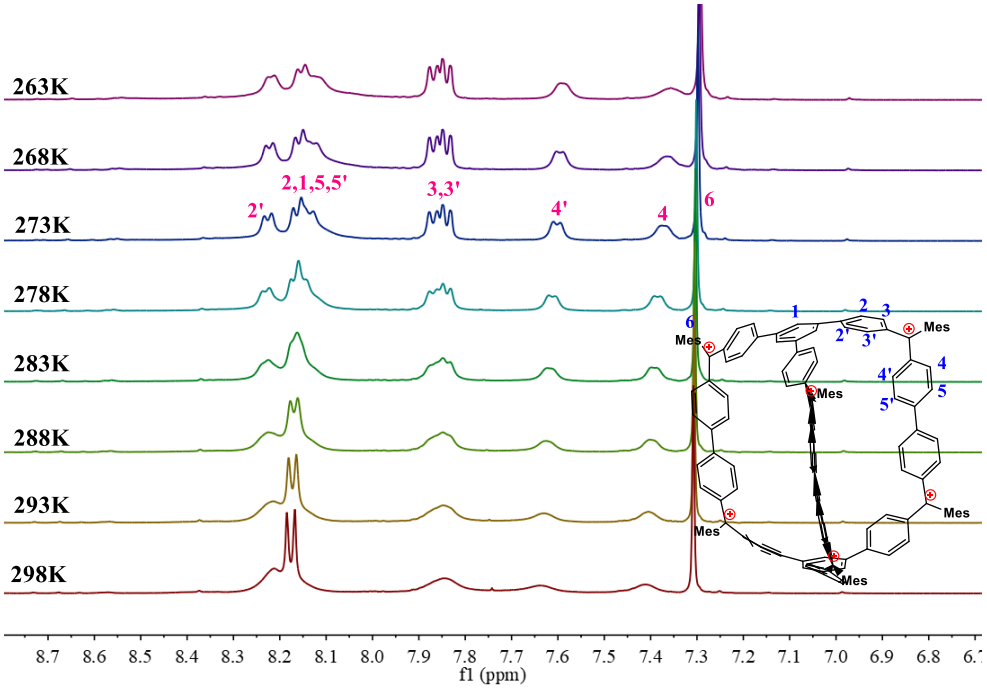

Figure S15. Variable temperature (298 K-263 K) ^{1}H NMR spectra of ***c*-Ph14^{6+}** (aromatic region) in CD_2Cl_2 with the assignment.

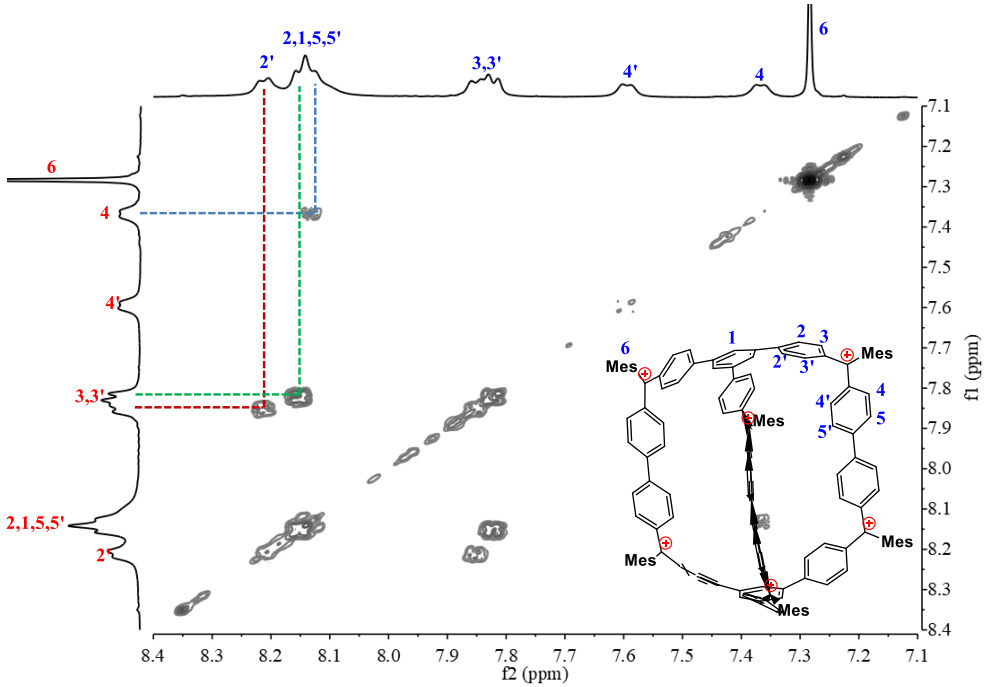

Figure S16. 2D COSY NMR spectrum (aromatic region) of ***c*-Ph14^{6+}** in CD_2Cl_2 at 268 K with the assignment.

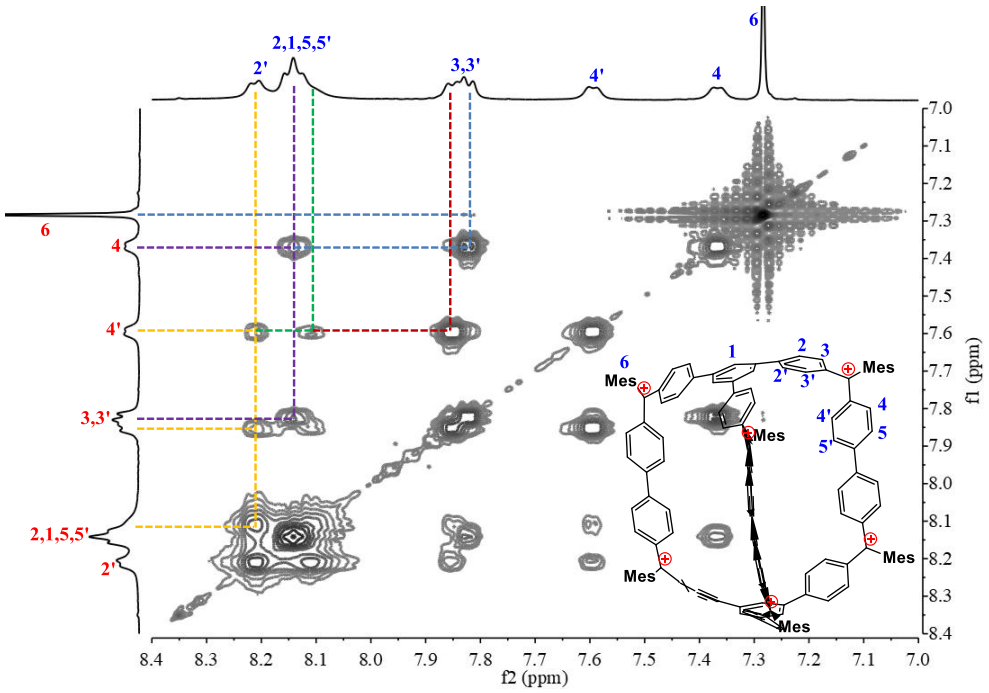

Figure S17. 2D NOESY NMR spectrum (aromatic region) of ***c*-Ph14^{6+}** in CD_2Cl_2 at 268 K with the assignment.

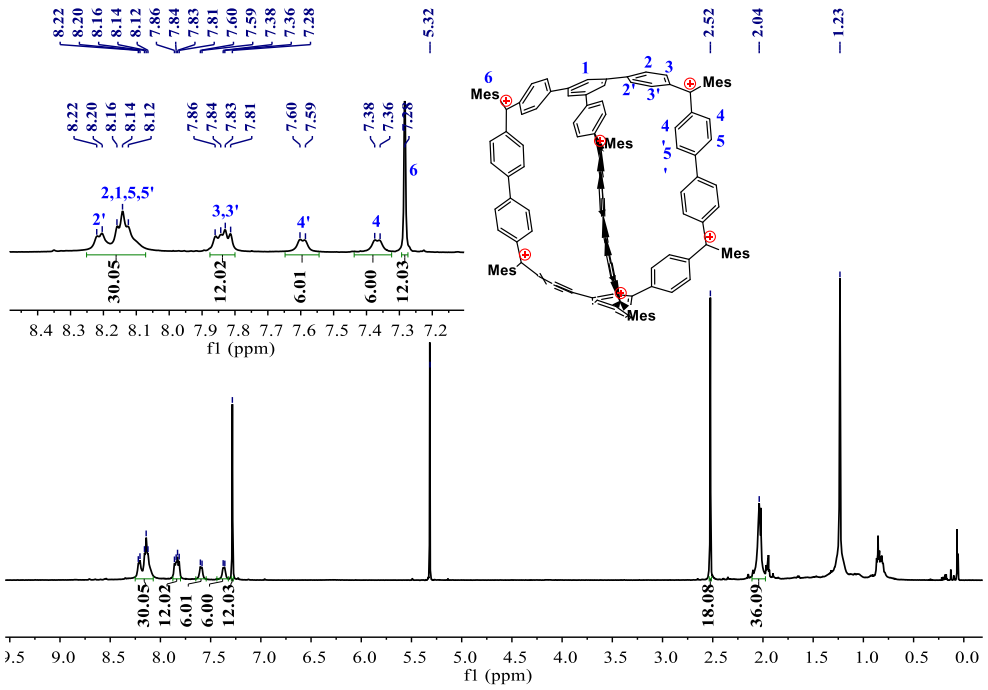

Figure S18. ^{1}H NMR spectrum of ***c*-Ph14^{6+}** in CD_2Cl_2 at 268 K with the assignment and integrations.

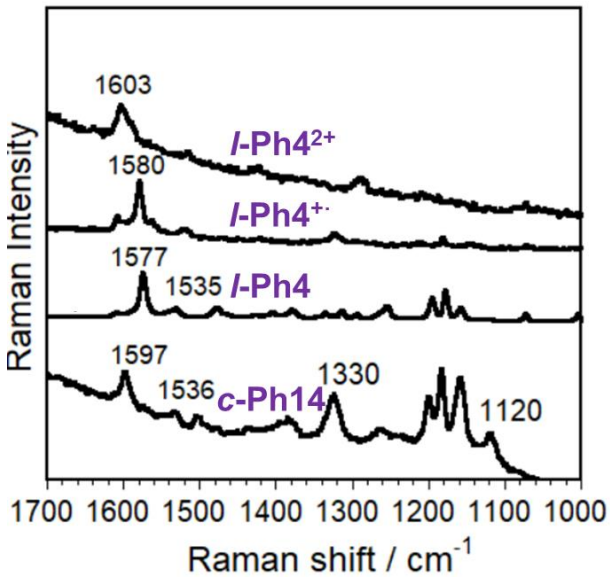

Figure S19. Raman spectra of ***c*-Ph14** and neutral ***l*-Ph4** together with the spectra of the radical cation ***l*-Ph4$^{+\cdot}$** and ***l*-Ph4^{2+}** obtained by electrochemical oxidation at room temperature.

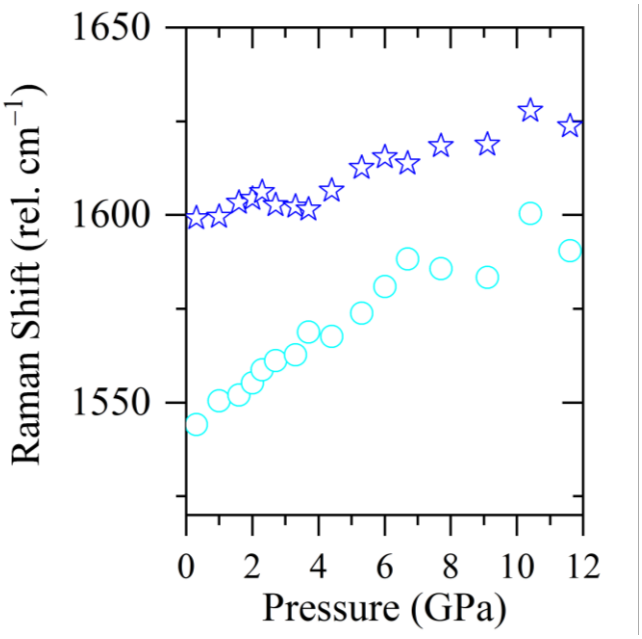

Figure S20. Raman shifts as a function of pressure of the CC stretching modes of the phenyl units (1600 cm^{-1} region).

3. Estimation of energy barrier by dynamic NMR

The exchange rate constant k was estimated according to the literature.[2] Three characteristic exchange regions were observed in all cases if available: (1) a slow exchange region, in which the exchange is slower than the spectrometer timescale and two separate peaks are observed; (2) coalescence, at which two peaks completely merge into one peak; and (3) fast exchange region, in which the exchange is rapid than the spectrometer and the two peaks are merged into one peak. The exchange rate constant k can be calculated by individual equation in these three regions.

i) At slow exchange temperature ($T < T_c$), two peaks are separated enough, the rate constant k can be determined by comparing the linewidth of a peak with no exchange with the line width of the peak with little exchange using the following formula:

$$k=\pi[(\Delta v_e)_{\frac{1}{2}} - (\Delta v_0)_{\frac{1}{2}}] \qquad (1)$$

ii) When temperature is close to T_c, two separated peaks will overlap with each other but not fully coalescent, thus the exchange constant at this temperature can then be calculated by:

$$k=\frac{\pi}{\sqrt{2}}(\Delta V_0^2 - \Delta V_e^2)^{1/2} \qquad (2)$$

iii) For the coalescence temperature k can be calculated using:

$$k = \frac{\pi \Delta V_0}{\sqrt{2}} \qquad (3)$$

iv) At fast exchange temperature ($T > T_c$)

$$k = \frac{\pi \Delta V_0^2}{2}[(\Delta v_e)_{\frac{1}{2}} - (\Delta v_0)_{\frac{1}{2}}]^{-1} \qquad (4)$$

In these equations, ΔV is the difference in chemical shift (Hz) between two correlated peaks at one temperature in the slow exchange region. ΔV_0 is defined as the value of ΔV at no exchange temperature (at which the two peaks are mostly separated), and ΔV_e is defined as the value of ΔV at all other temperatures in this region if available. $(\Delta v)_{\frac{1}{2}}$ is the linewidth (Hz) at half height of peak at anyone temperature in all region if available. $(\Delta v_0)_{\frac{1}{2}}$ is defined as the value of $(\Delta v)_{\frac{1}{2}}$ at no exchange temperature. $(\Delta v_e)_{\frac{1}{2}}$ is defined as the value of $(\Delta v)_{\frac{1}{2}}$ at all other temperatures in all

region if available. T_c is defined as coalescence temperature at which two peaks completely merge into one peak. The obtained k values were then fitted with Eyring equation:

$$\ln\frac{k}{T} = -\frac{\Delta H^{\ddagger}}{RT} + \frac{\Delta S^{\ddagger}}{R} + ln\frac{k_B}{h} \qquad (6)$$

and then:

$$\Delta G^{\ddagger} = \Delta H^{\ddagger} - T\Delta S^{\ddagger} \qquad (7)$$

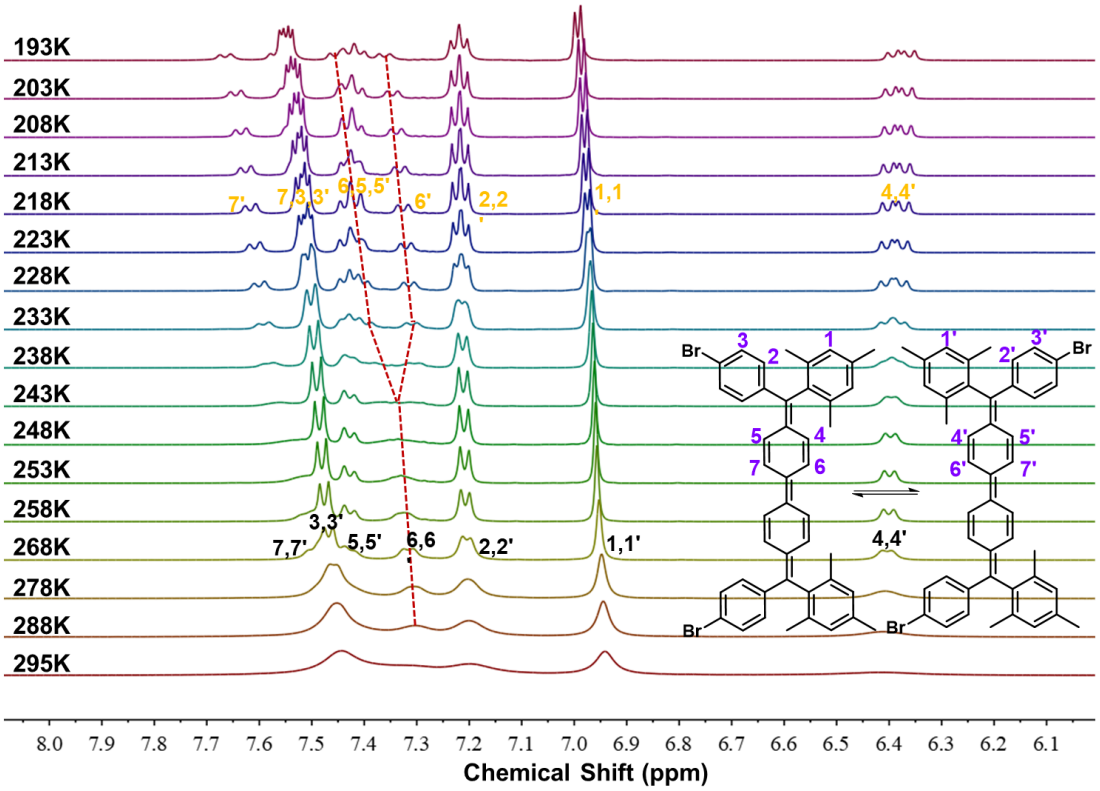

Figure S21. VT ^{1}H NMR spectra (aromatic region) of ***l*-Ph4** in THF-d_8.

From the VT ^{1}H NMR spectra of ***l*-Ph4** in THF-d_8 (Figure S21), the *cis*-/*trans*-isomerization process was clearly demonstrated with the following information:

1) The coalescence temperature is 243 K;

2) When the temperature goes to 213 K, the peaks are fully separated.

Therefore, the exchange rate constant k can be calculated by individual equation in these three regions.

Table S1. Parameters obtained from the line-shape analysis based on the VT ^{1}H NMR spectra of ***l*-Ph4** in THF-d_8.

T (K)	$\Delta\upsilon_e^{1/2}$ (Hz)	ΔVe	Exchange constant k (s^{-1})	1/T (K^{-1})	ln(k/T)
268	20.14 (Fully merged) $\Delta\upsilon_0^{1/2}$ for one peak temperature range				
258	21.70		2221.44	0.003876	2.15295
253	24.40		814.15	0.003953	1.168749
248	37.43		200.72	0.004032	-0.21151
243	Coalescence Temp		102.36	0.004115	-0.86453
238	24.45	42.9	19.64	0.004202	-2.4946
233	19.39	43.5	8.4	0.004292	-3.32263
228	16.98	44.4	3.05	0.004386	-4.31492
223	15.78	45	0.375	0.004484	-6.38687
218	15.66	45.41	0.122	0.004587	-7.48676
213	15.60 ($\Delta\upsilon_0^{1/2}$)	46.08 (ΔV_0)			

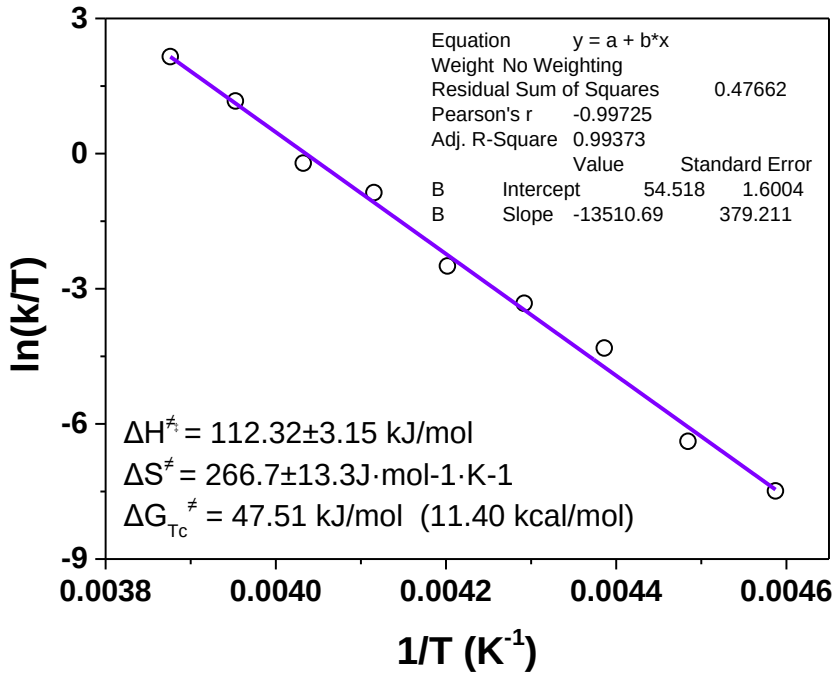

Figure S22. Estimation of the *cis*-/*trans*- isomerization energy barrier of ***l*-Ph4** by fitting the exchange rate constants at different temperatures by Eyring equation.

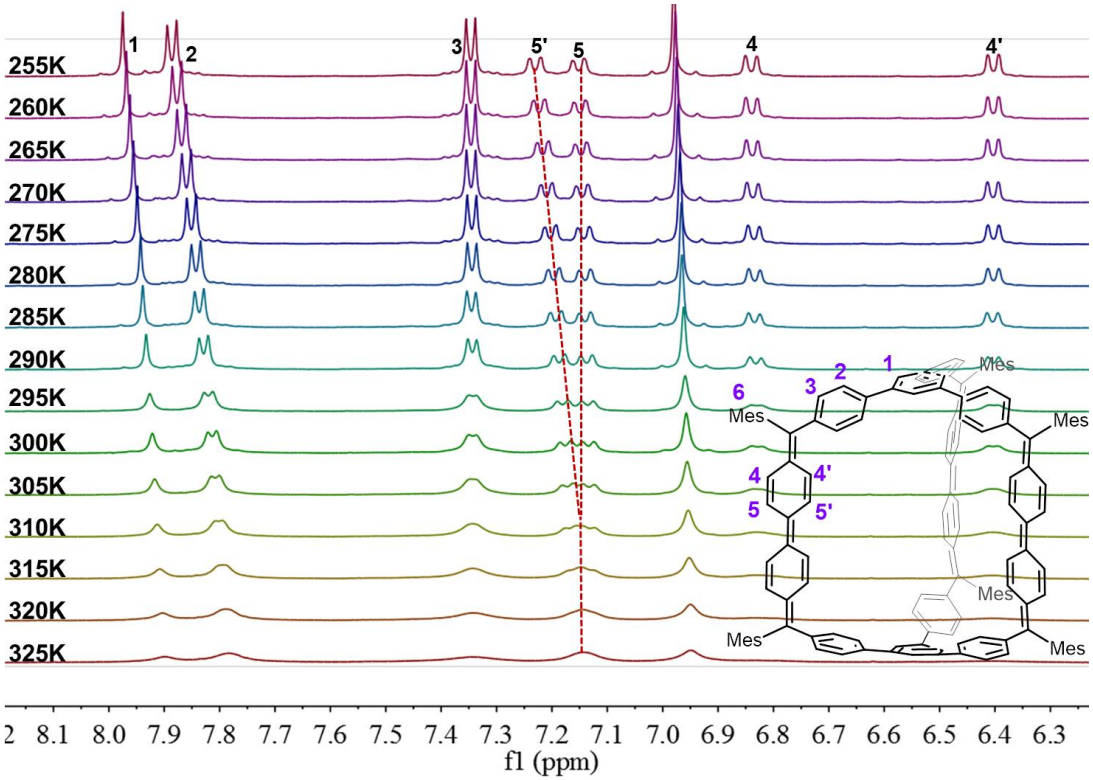

Figure S23. VT ^{1}H NMR spectra (aromatic region) of ***c*-Ph14** in THF-d_8.

From the VT ^{1}H NMR spectra of ***c*-Ph14** in THF-d_8 (Figure S23), the dynamic flipping process was clarified with the following information:

1) The coalescence temperature is 310K;

2) When the temperature goes to 275K, the peaks are fully separated.

Therefore, the exchange rate constant k can be calculated by individual equation in these three regions.

Table S2. Parameters obtained from the line-shape analysis based on the VT ^{1}H NMR spectra of ***c*-Ph14** in THF-d_8.

T (K)	Exchange constant k (s^{-1})	1/T (K^{-1})	ln(k/T)
275	Peaks are fully seperated		
280	0.533146	0.003571	-6.26375
285	1.266221	0.003509	-5.41645
290	2.887871	0.003448	-4.60936
295	7.21651	0.00339	-3.71016
300	16.21651	0.003333	-2.91772

305	45.67701	0.003279	-1.89872
310	66.732	0.003226	-1.53589
315	104.3	0.003175	-1.1053
320	112.62	0.003125	-1.0443

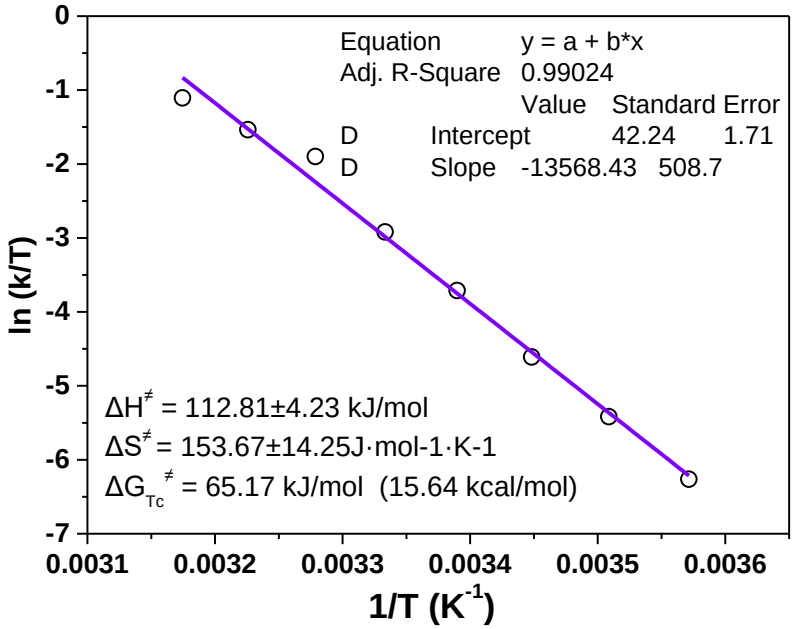

Figure S24. Estimation the flipping energy barrier of ***c*-Ph14** by fitting the exchange rate constants at different temperatures by Eyring equation.

From the VT ^{1}H NMR spectra of ***l*-Ph4^{2+}** in CD_2Cl_2 (Figure S11) we can see that the rotation of the central biphenyl subunits was restricted to a detectable range, in which the following information can be drawn:

1) The coalescence temperature is 288 K;

2) When the temperature goes to 263 K, the peaks are fully separated.

Therefore, the exchange rate constant *k* can be calculated by individual equation in these three regions.

Table S3. Parameters obtained from the line-shape analysis based on the VT ^{1}H NMR spectra of ***l*-Ph4^{2+}** in CD_2Cl_2.

T (K)	Exchange constant k (s^{-1})	1/T (K^{-1})	ln(k/T)

288	195.04	0.003472	-0.3897
283	98.46	0.003534	-1.0558
278	44.68	0.003597	-1.8977
273	13.64	0.003663	-2.9965
268	7.44	0.003731	-3.5839
263	2.64	0.003802	-4.6017
258	1.0	0.003876	-5.5445

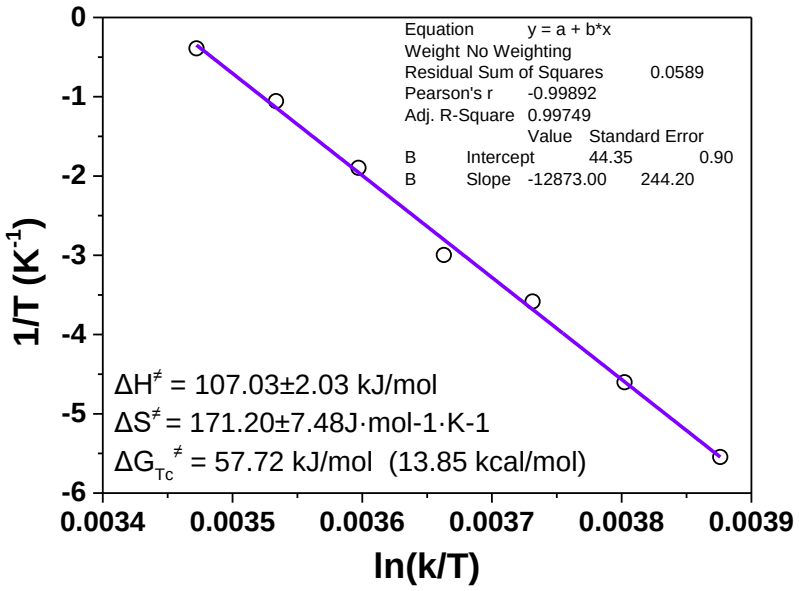

Figure S25. Estimation of the rotation energy barrier of the central biphenyls in ***l*-Ph4^{2+}** by fitting the exchange rate constants at different temperatures by Eyring equation.

From the VT ^{1}H NMR spectra of ***c*-Ph14^{6+}** in CD_2Cl_2 (Figure S15), we can see that the rotation of the central biphenyl subunits was restricted to a detectable range, in which the following information can be drawn:

1) The coalescence temperature is beyond boiling point of CD_2Cl_2, due to the structural rigidity and conformational restriction of the cage framework;

2) When the temperature goes to 268 K, the peaks are fully separated.

Therefore, the exchange rate constant *k* can be calculated by individual equation, and the rotation energy barrier of the central biphenyls in can ***c*-Ph14^{6+}** be roughly estimated.

Table S4. Parameters obtained from the line-shape analysis based on the VT ^{1}H NMR spectra of ***c*-Ph14^{6+}** in CD_2Cl_2.

T (K)	Exchange constant k (s^{-1})	1/T (K^{-1})	ln(k/T)
298	55.05	0.003356	-1.69
293	28.45	0.003413	-2.33
288	16.00	0.003472	-2.89
283	9.21	0.003534	-3.43
278	3.99	0.003597	-4.25
273	1.67	0.003663	-5.10

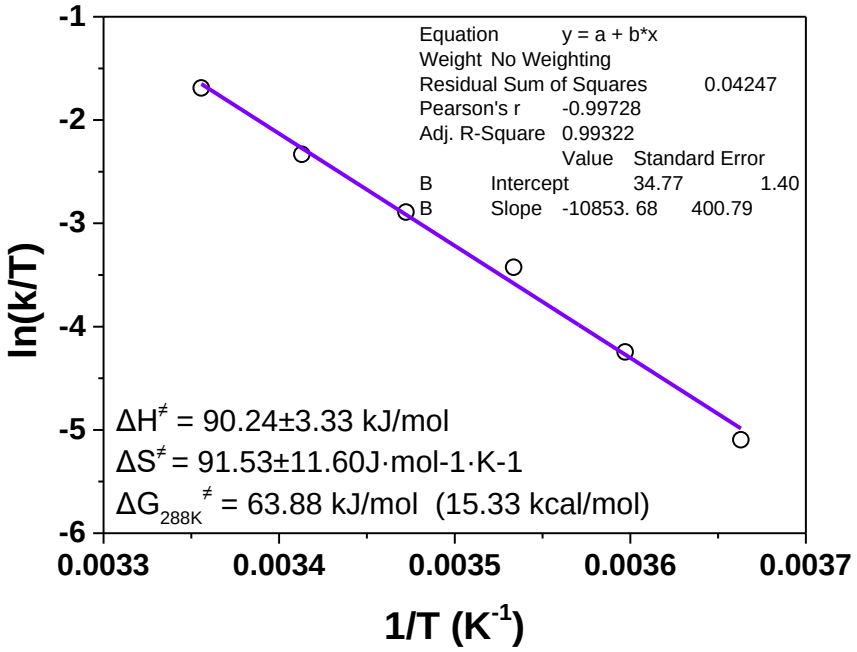

Figure S26. Estimation of the rotation energy barrier of the central biphenyls in ***c*-Ph14^{6+}** by fitting the exchange rate constants at different temperatures by Eyring equation. Since the coalescent temperature is beyond the detection limit using CD_2Cl_2 as solvent, the thermal dynamic parameters were roughly estimated from observed VT-NMR data, and the energy barrier of ***c*-Ph14^{6+}** at 288 K (the coalescent temperature of ***l*-Ph4^{2+}**) was calculated to make comparison with ***l*-Ph4^{2+}**.

4. Estimation of association constant

To determine the selective encapsulation of C_{70} over C_{60}, the binding of ***c*-Ph14** with C_{60} and C_{70} was monitored by UV-vis absorption and fluorescence titration experiments. Upon gradual addition of C_{60}, no appreciable change was observed in both absorption and fluorescence spectra (Figure S27). In contrast, a clear fluorescence quenching was observed when the solution of ***c*-Ph14** in 1,2-dichlorobenzene was titrated with C_{70}. In the fluorescence titration experiments, the concentration of ***c*-Ph14** was constant to be 1.16×10^{-5} M, and the fluorescence intensity upon adding varying concentration of C_{70} was recorded. The association constant (K_a) of ***c*-Ph14**⊃ **C_{70}** was then estimated by a non-linear curve-fitting method on the basis of the following equation:

$$\Delta F = (\Delta F_\infty/[H]_0)(0.5[G]_0+0.5([H]_0+1/K_a)-(0.5([G]_0^2+(2[G]_0(1/K_a-[H]_0))+(1/K_a+[H]_0)^2)^{0.5})) \quad (8)$$

Where ΔF is the fluorescence intensity changes at 780 nm at $[H]_0$, ΔF_∞ is the fluorescence intensity changes at 780 nm when ***c*-Ph14** is completely complexed, $[G]_0$ is the initial concentration of C_{70}, and $[H]_0$ is the fixed initial concentration of ***c*-Ph14**.

^{1}H NMR and DOSY NMR spectra of ***c*-Ph14** and its complex with C_{70} were recorded to determine the rough size of the binding structure (Figures S29 and S30). The diffusion coefficient obtained from DOSY NMR is roughly related to the molecular size on the following equation:

$$D = \frac{k_B T}{6\pi\eta r_h}$$

where D represent the diffusion coefficient, k_B is the Boltzman's constant, T is the temperature (K), η is the solvent viscosity, r_h is the hydrodynamic radius of the molecule that was roughly seen as a ball.

From the DOSY NMR analysis (Figures S30-S31), the diffusion coefficient (D) of ***c*-Ph14** is estimated to be 6.44 m^2/S, whereas the complex [***c*-Ph14**+C_{70}] shows a D value of about 6.31 m^2/S. These two values are similar, suggesting that they have similar molecular size and thus C_{70} should be encapsulated inside the cavity of ***c*-Ph14**.

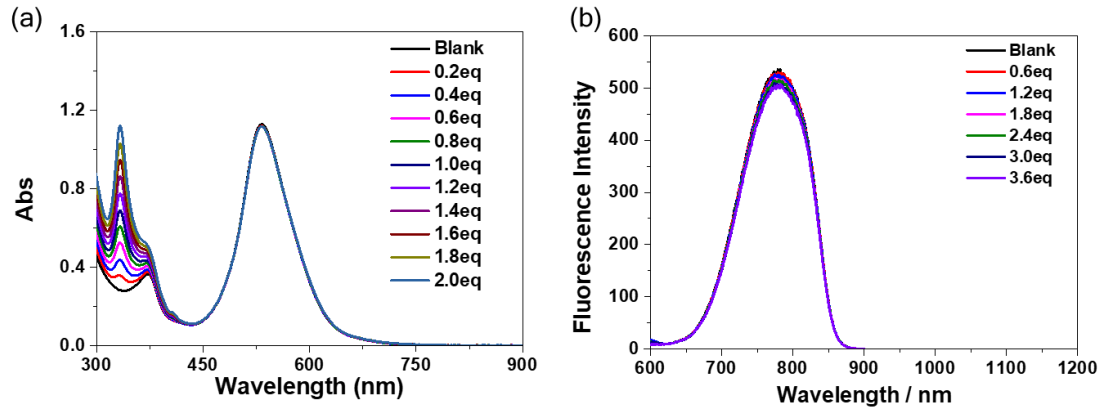

Figure S27. Change in (a) absorption spectra (0→2.0 equiv) and (b) fluorescence spectra upon addition of C_{60} (0→3.6 equiv) to the solution of ***c*-Ph14** in 1,2-dichlorobenzene.

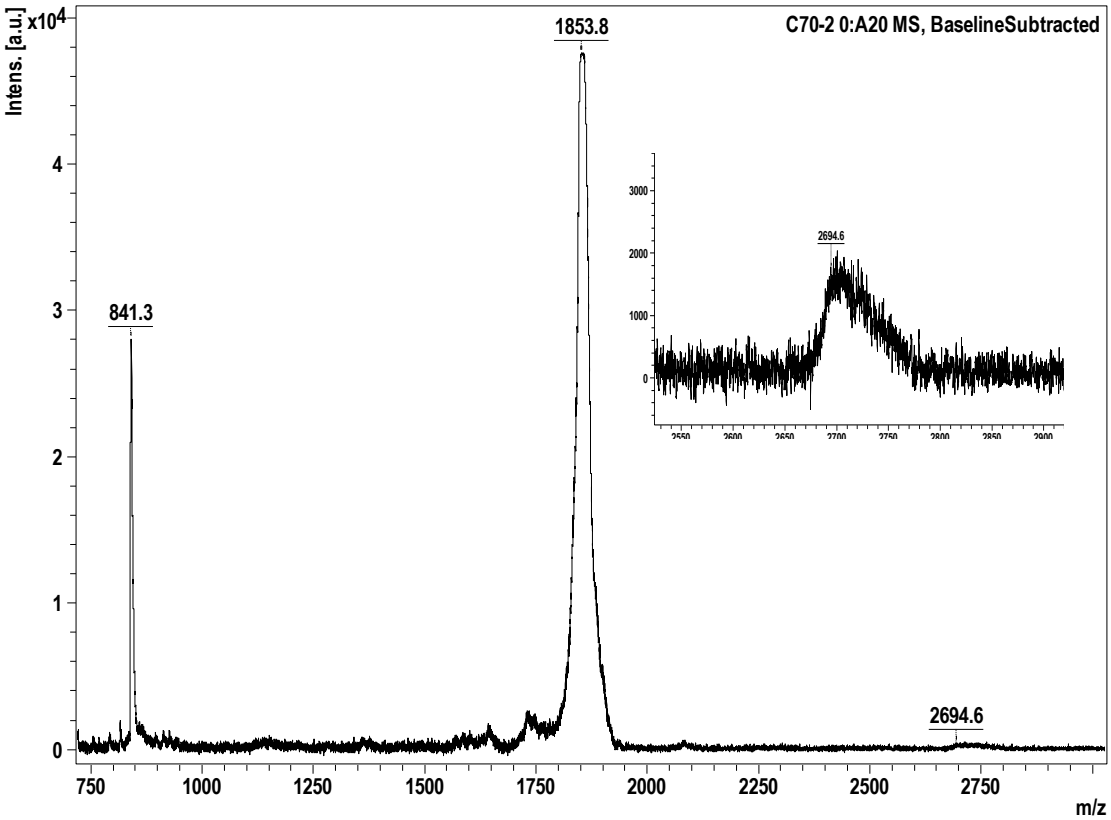

Figure S28. MALDI-TOF mass spectra for the complex of ***c*-Ph14** with C_{70}. In the mass spectrum, the signal peak for each component was observed, 841.3 for C_{70} and 1853.8 for ***c*-Ph14**, respectively, and a small peak corresponding to the complex C_{70}@***c*-Ph14** at 2694.6 was obtained as well.

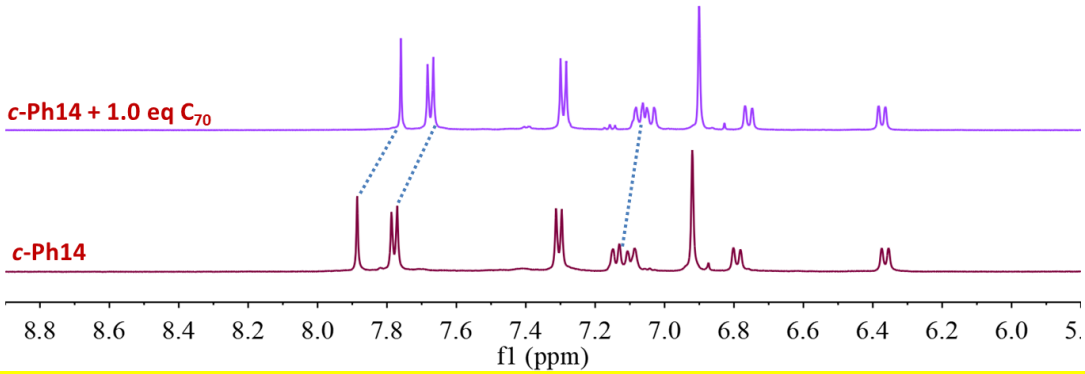

Figure S29. ^{1}H NMR spectra of ***c*-Ph14** and ***c*-Ph14** with 1.0 equivalent C_{70} in the mixture solvent consisting of 60% d_8-THF and 40% CS_2 at 285 K. All peaks for the protons on the backbone of ***c*-Ph14** are shifted to high field upon complexation, indicating an encapsulation of C_{70} inside the cavity.

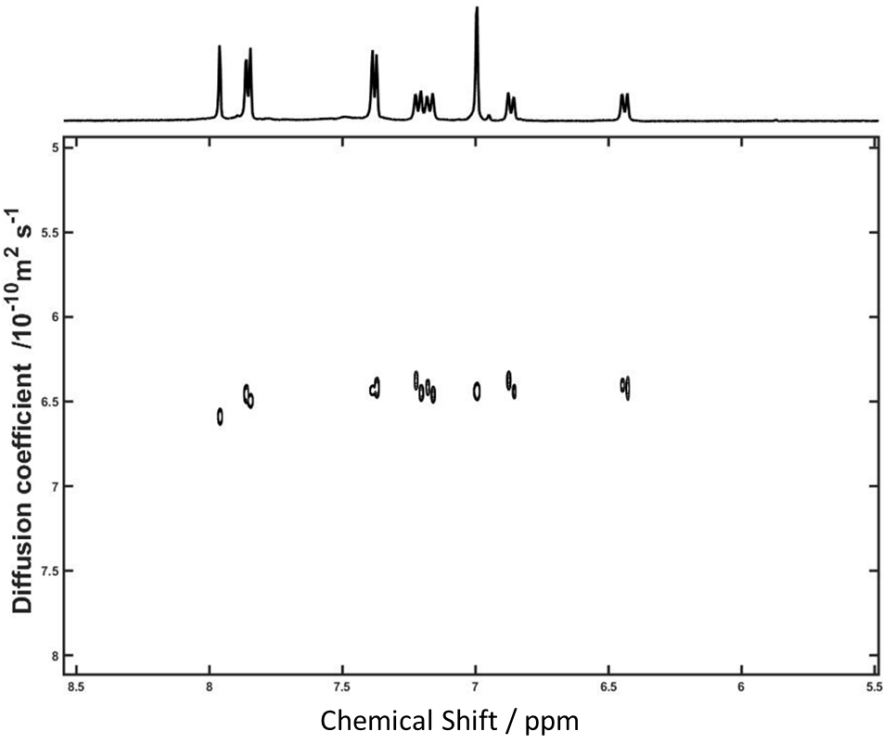

Figure S30. DOSY NMR spectrum of ***c*-Ph14** in the mixture solvent consisting of 60% d_8-THF and 40% CS_2 at 285 K, and the averaged diffusion coefficient (*D*) is estimated to be 6.44 m^2/S.

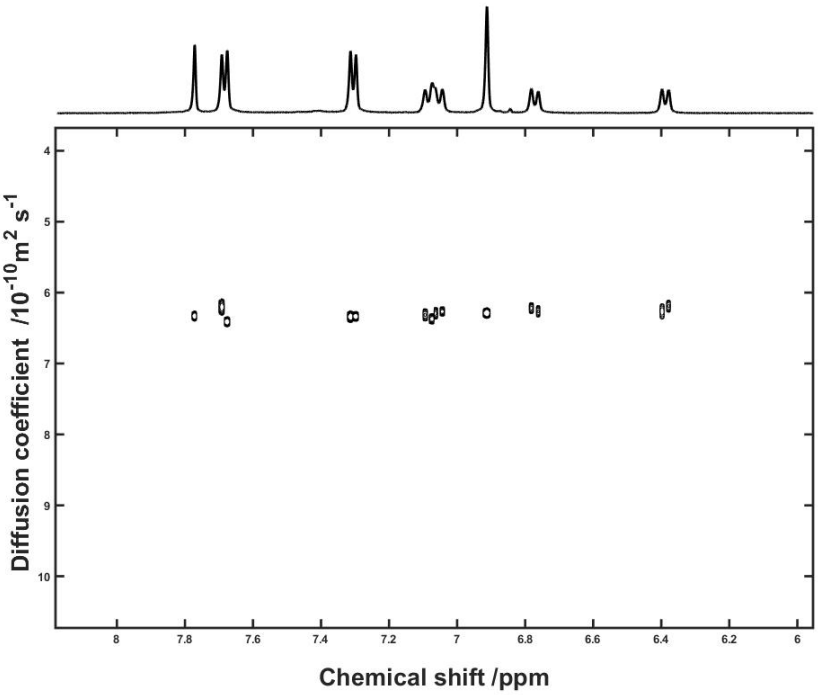

Figure S31. DOSY NMR spectrum of the 1:1 complex of ***c*-P14** and C_{70} in the mixture solvent consisting of 60% d_8-THF and 40% CS_2 at 285K, and the averaged diffusion coefficient (*D*) is estimated to be 6.31 m^2/S.

5. Theoretical calculations

Theoretical calculations were performed with the Gaussian09 program suite.[3] All calculations were carried out using the density functional theory (DFT) method with Becke's three-parameter hybrid exchange functionals and the Lee-Yang-Parr correlation functional (B3LYP) employing the 6-31G(d,p) basis set for all atoms.[4] Natural orbital occupation number (NOON) calculations were done by spin unrestricted UCAM-B3LYP/6-31G(d,p) method, and the multiple diradical characters y_i are defined as the occupation number of the LUNO+*i*.[5]

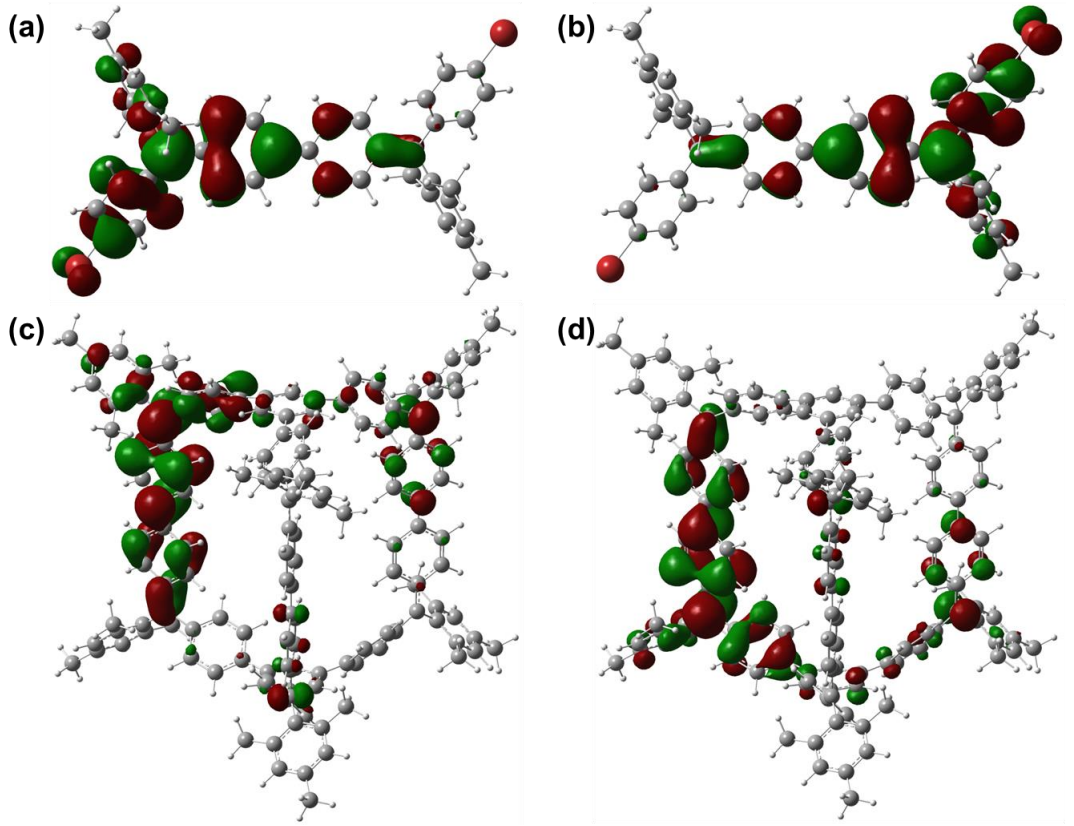

Figure S32. Calculated (UB3LYP/6-31G(d,p)) SOMO profiles of ***l*-Ph4** (SOMO α-spin (a), SOMO β-spin (b)) and ***c*-Ph14** (SOMO α-spin (c), SOMO β-spin (d)).

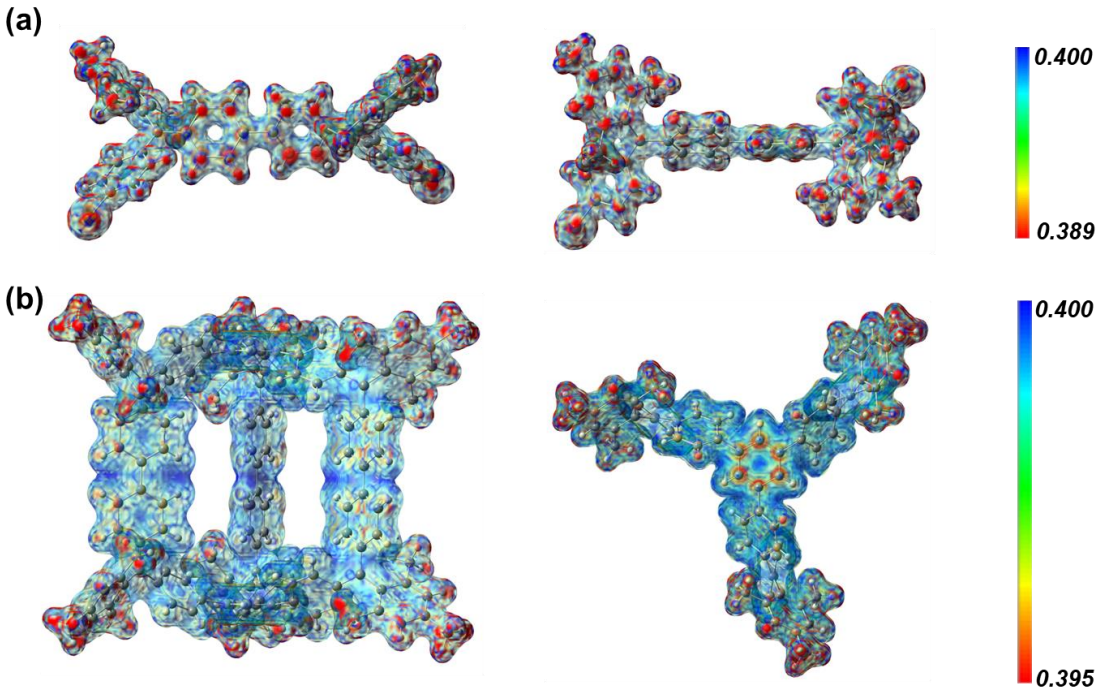

Figure S33. Side views and top views of calculated charge distribution maps of ***l*-Ph4^{2+}** (a) and ***c*-Ph14^{6+}** (b).

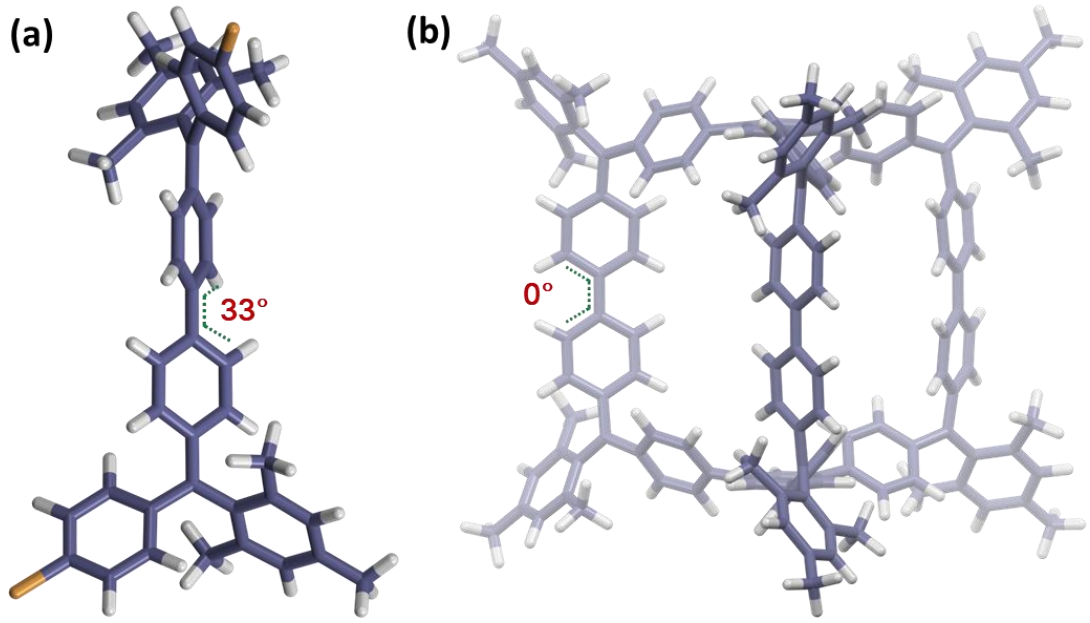

Figure S34. Optimized geometries of (a) ***l*-Ph4**$^{2+}$ and (b) ***c*-Ph14**$^{6+}$ at RB3LYP6-31G(d,p) level of theory. The torsion angles among the biphenyl subunits are labeled.

6. X-ray crystallographic data

The X-ray intensity data were measured at low temperature (T=100K), using a four circles goniometer Kappa geometry, Bruker AXS D8 Venture, equipped with a Photon 100 CMOS active pixel sensor detector. Frames were integrated with the Bruker SAINT[6] software package. Data were corrected for absorption effects using the multi-scan method (SADABS).[7] Molecule was solved with the software SHELXT,[8] using a Dual Space method. Refinement of the structure was performed by least squares procedures on weighted F2 values using the SHELXL-version 2014/6[9] included in the WinGx system programs for Windows.[10] Single crystal of compound ***l*-Ph4** (CCDC No 1190471) was obtained through slow evaporation of acetonitrile to its THF solution. Single crystal of ***l*-Ph4**$^{2+}$ (CCDC No 1190472) was obtained through slow diffusion of cyclohexane to its dichloromethane solution. Single crystal of ***c*-Ph14**$^{6+}$ (CCDC No 1190473) was obtained through slow diffusion of hexanes to its dichloromethane solution.

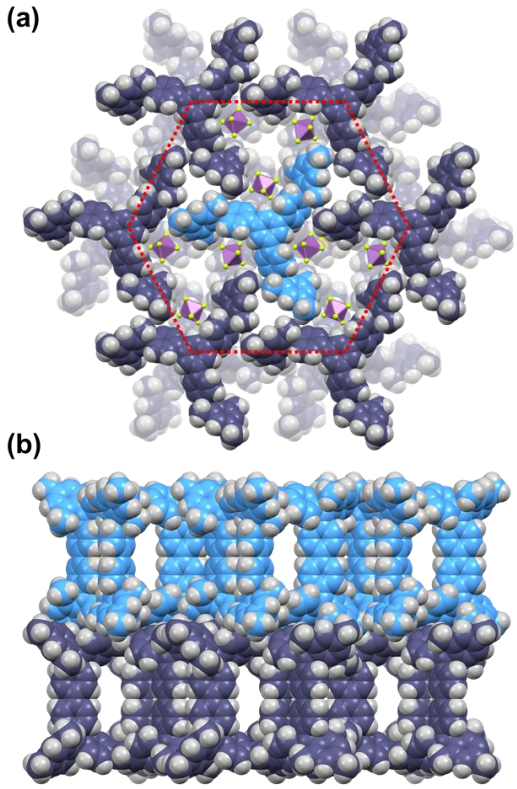

Figure S35. Packing structure of ***c*-Ph14**$^{6+}$ in *ab* plane. Layer structure was observed demonstrated seen from top view (a) and side view (b).

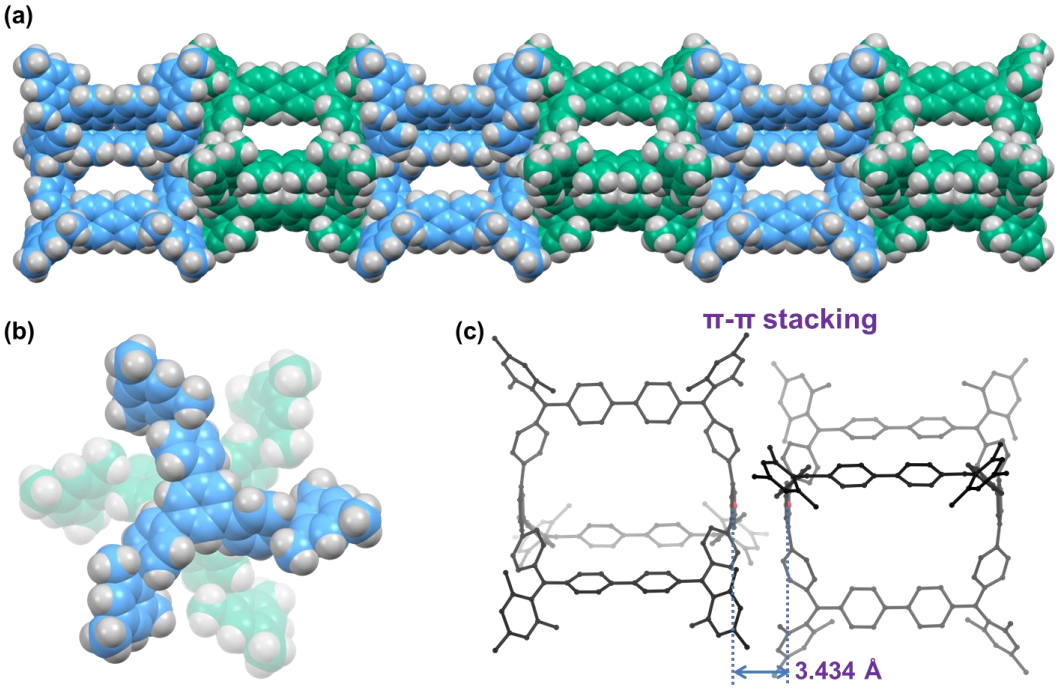

Figure S36. Packing structure of ***c*-Ph14**$^{6+}$ along *c* axis seen from side view (a) and top view (b). A molecular column based on prism-like cage framework (a), (b). The interaction between neighboring molecules is typical π-π stacking, as demonstrated in (c).

Table S5. Crystal data and structure refinement for ***l*-Ph4**.

Identification code	CCDC 1190471
Empirical formula	$C_{11}H_{9.5}Br_{0.5}$
Formula weight	60.55
Temperature/K	99.98
Crystal system	triclinic
Space group	P-1
a/Å	7.8715(3)
b/Å	8.3728(3)
c/Å	14.1114(5)
α/°	94.3560(10)
β/°	98.7750(10)
γ/°	91.6830(10)
Volume/Å^3	915.70(6)
Z	12
ρ_{calc}g/cm^3	1.318
μ/mm^{-1}	2.242
F(000)	372.0
Crystal size/mm^3	0.876 × 0.682 × 0.468
Radiation	MoKα (λ = 0.71073)
2Θ range for data collection/°	4.884 to 59.23
Index ranges	-10 ≤ h ≤ 10, -10 ≤ k ≤ 11, -19 ≤ l ≤ 19
Reflections collected	28199
Independent reflections	5103 [R_{int} = 0.0551, R_{sigma} = 0.0350]
Data/restraints/parameters	5103/0/211
Goodness-of-fit on F^2	1.134
Final R indexes [I>=2σ (I)]	R_1 = 0.0300, wR_2 = 0.0996
Final R indexes [all data]	R_1 = 0.0362, wR_2 = 0.1112

Largest diff. peak/hole / e $Å^{-3}$	0.55/-0.67

Table S6. Crystal data and structure refinement for ***l*-Ph4^{2+}**.

Identification code	CCDC 1190472
Empirical formula	$C_{22}H_{19}BrF_6Sb$
Formula weight	599.03
Temperature/K	100.01
Crystal system	orthorhombic
Space group	Pcca
a/Å	34.691(17)
b/Å	8.184(4)
c/Å	15.076(7)
α/°	90
β/°	90
γ/°	90
Volume/$Å^3$	4280(3)
Z	8
$\rho_{calc}g/cm^3$	1.859
μ/mm^{-1}	3.214
F(000)	2328.0
Crystal size/mm^3	0.68 × 0.46 × 0.15
Radiation	MoKα (λ = 0.71073)
2Θ range for data collection/°	4.696 to 56.616
Index ranges	$-46 \leq h \leq 46$, $-10 \leq k \leq 10$, $-20 \leq l \leq 19$
Reflections collected	71907
Independent reflections	5305 [R_{int} = 0.0998, R_{sigma} = 0.0408]
Data/restraints/parameters	5305/0/276
Goodness-of-fit on F^2	1.185

Final R indexes [I>=2σ (I)]	R_1 = 0.0585, wR_2 = 0.1345
Final R indexes [all data]	R_1 = 0.0896, wR_2 = 0.1567
Largest diff. peak/hole / e Å^{-3}	1.32/-2.49

Table S7. Crystal data and structure refinement for ***c*-Ph14^{6+}**.

Identification code	CCDC 1190473
Empirical formula	$C_{144}H_{120}F_{36}Sb_6$
Formula weight	3258.30
Temperature/K	100.03
Crystal system	hexagonal
Space group	$P6_3/m$
a/Å	18.9873(11)
b/Å	18.9873(11)
c/Å	33.688(2)
α/°	90
β/°	90
γ/°	120
Volume/Å^3	10517.9(14)
Z	2.0004
ρ_{calc}g/cm^3	1.007
μ/mm^{-1}	0.822
F(000)	3150.0
Crystal size/mm^3	0.75 × 0.65 × 0.52
Radiation	MoKα (λ = 0.71073)
2Θ range for data collection/°	5.1 to 56.566
Index ranges	-25 ≤ h ≤ 25, -25 ≤ k ≤ 25, -44 ≤ l ≤ 44
Reflections collected	340864
Independent reflections	8607 [R_{int} = 0.0878, R_{sigma} = 0.0307]

Data/restraints/parameters	8607/0/293
Goodness-of-fit on F^2	1.147
Final R indexes [I>=2σ (I)]	R_1 = 0.1029, wR_2 = 0.2927
Final R indexes [all data]	R_1 = 0.1411, wR_2 = 0.3503
Largest diff. peak/hole / e $Å^{-3}$	1.07/-0.50

7. NMR and high-resolution mass spectra of new compounds

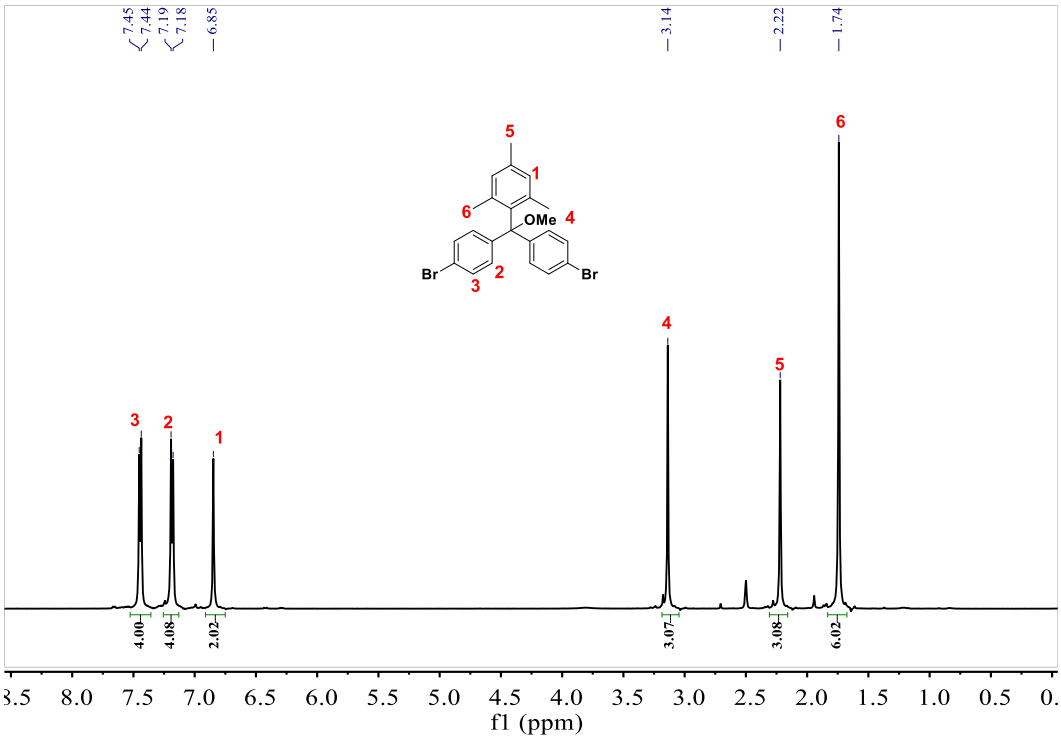

Figure S37. ^{1}H NMR spectrum of compound **3** (500 MHz, DMSO-d_6, rt).

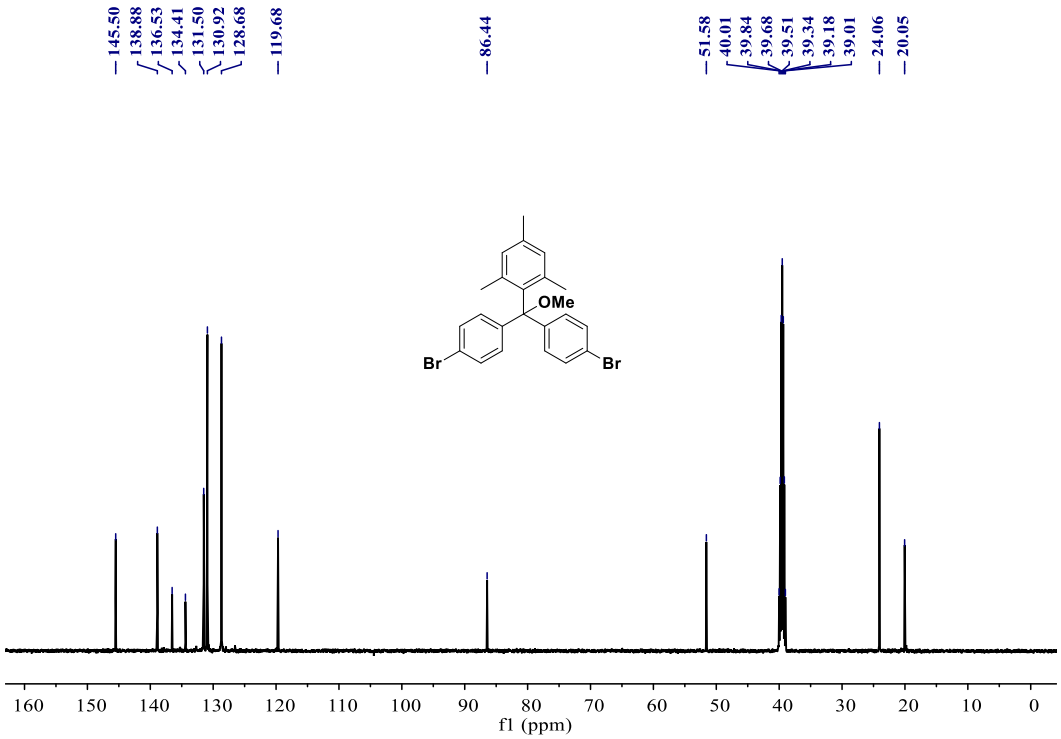

Figure S38. ^{13}C NMR spectrum of compound **3** (126 MHz, DMSO-d_6, rt).

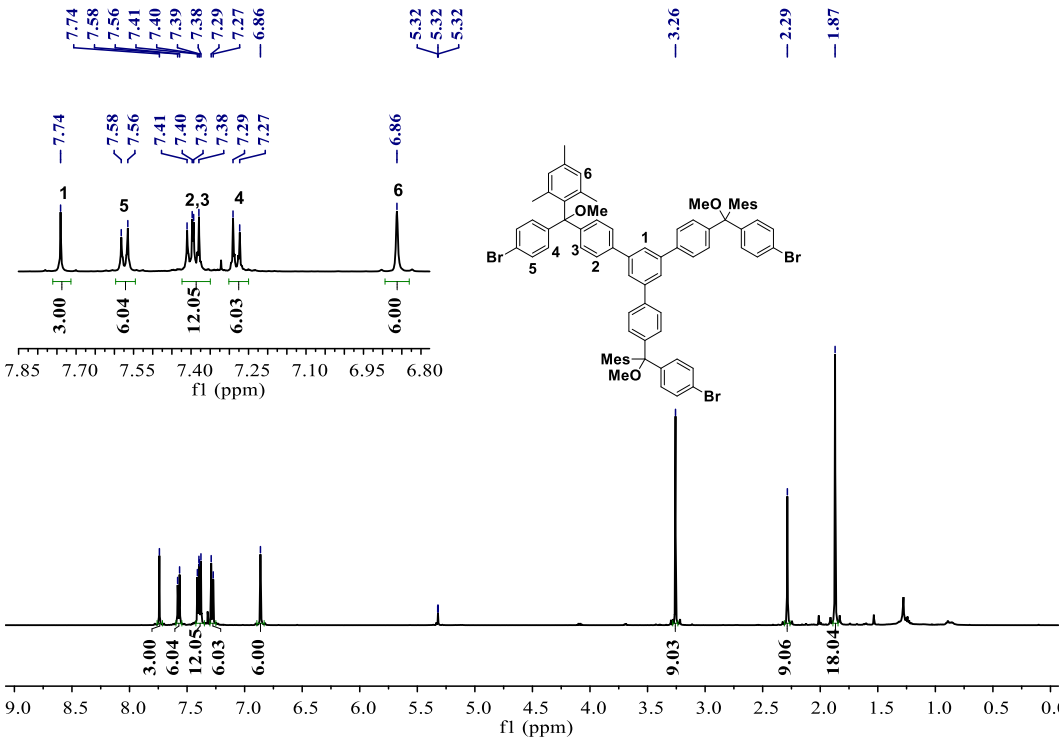

Figure S39. ^{1}H NMR spectrum of compound **4** (500 MHz, DMSO-d_6, rt).

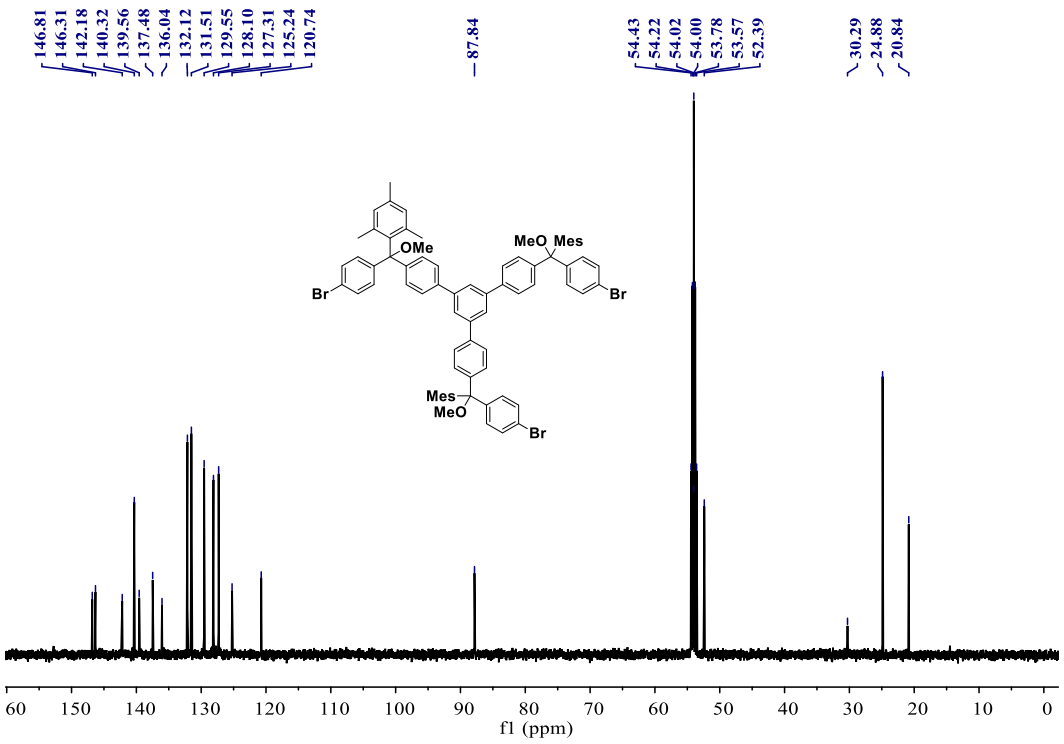

Figure S40. ^{13}C NMR spectrum of compound **4** (126 MHz, CD_2Cl_2, rt).

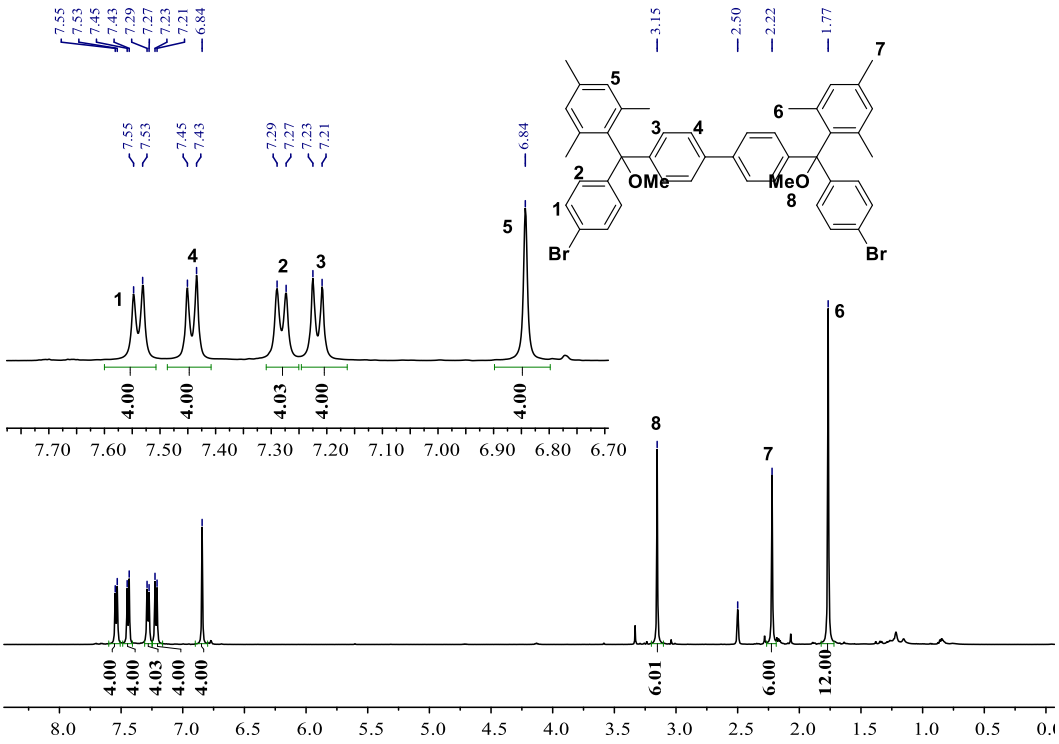

Figure S41. ^{1}H NMR spectrum of compound **7** (500 MHz, DMSO-d_6, rt).

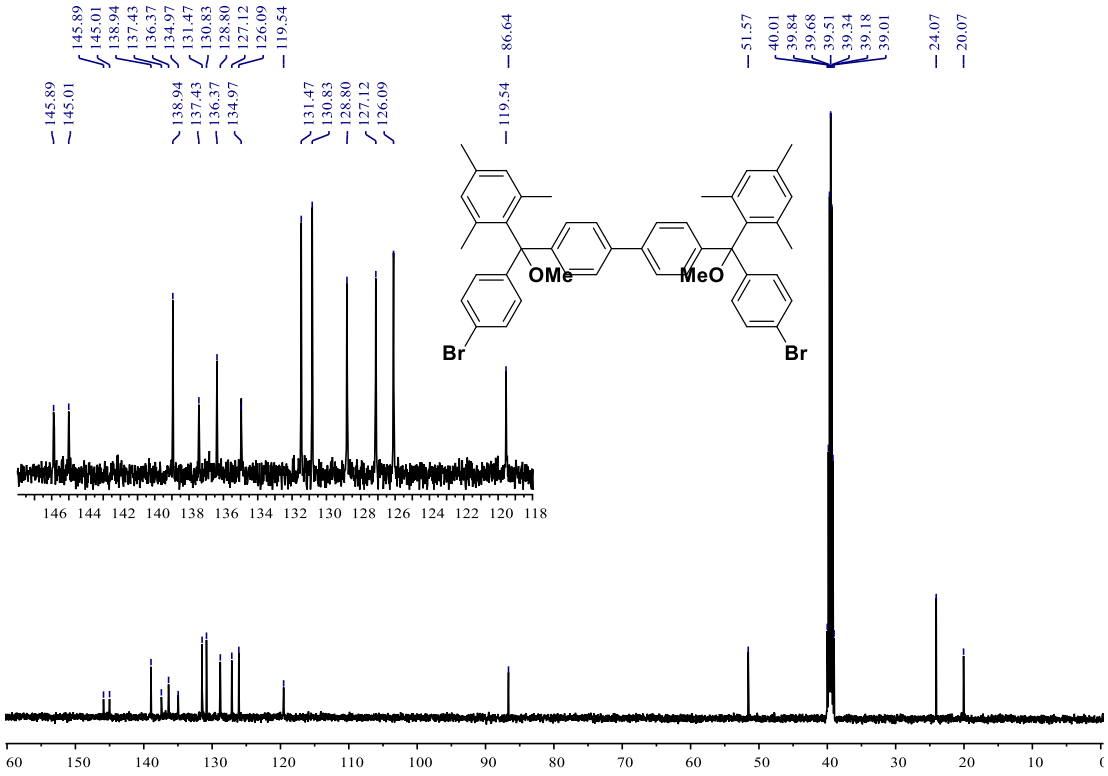

Figure S42. ^{13}C NMR spectrum of compound **7** (126 MHz, $CDCl_3$, rt).

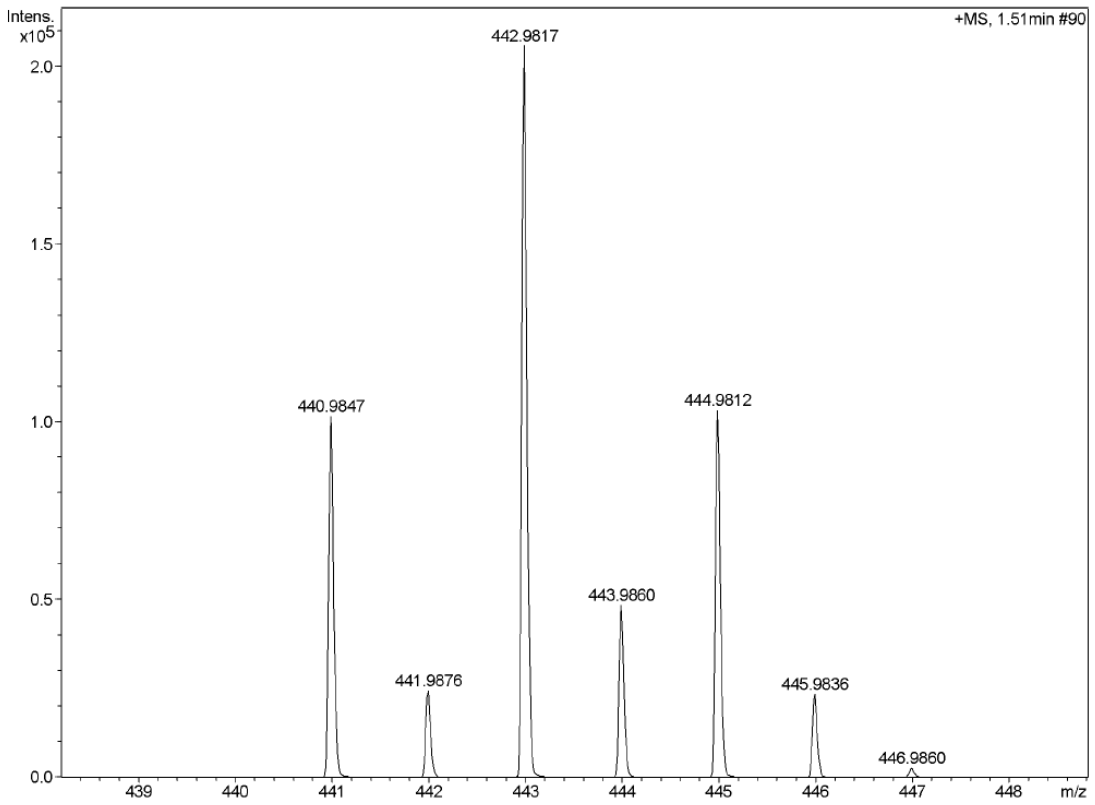

Figure S43. HR mass spectrum (APCI) of the compound **3**.

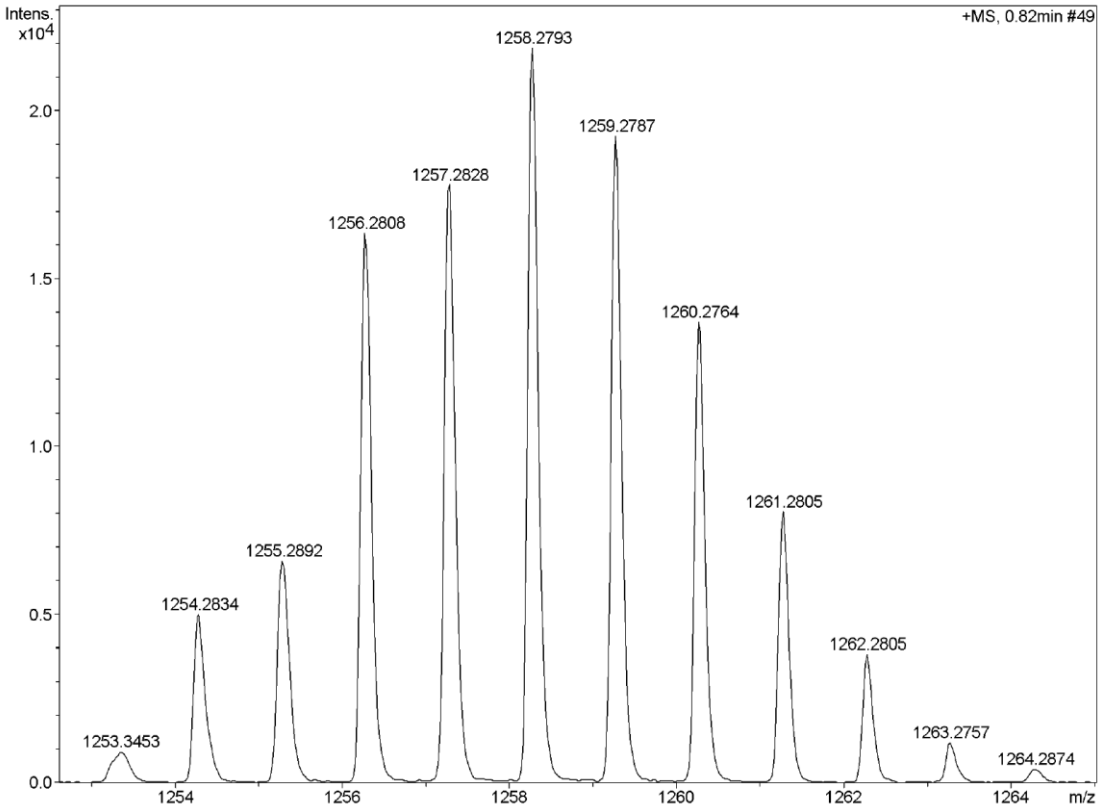

Figure S44. HR mass spectrum (APCI) of the compound **4**.

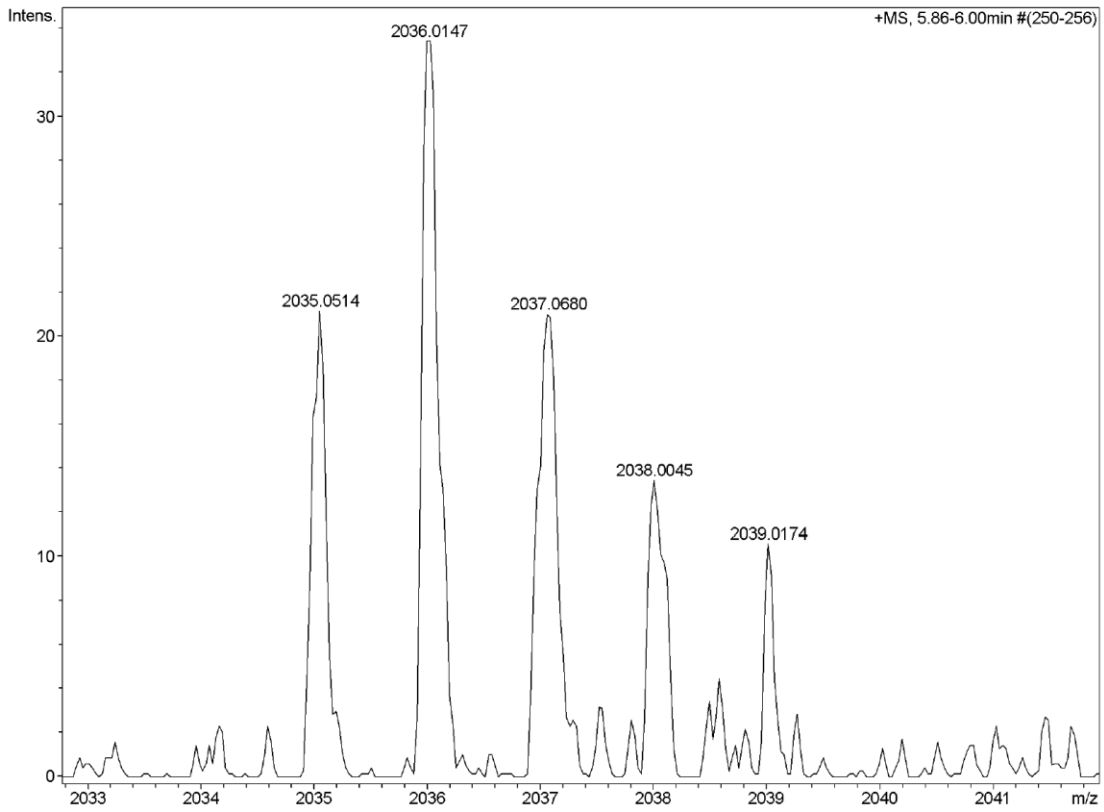

Figure S45. HR mass spectrum (APCI) of the compound **5**.

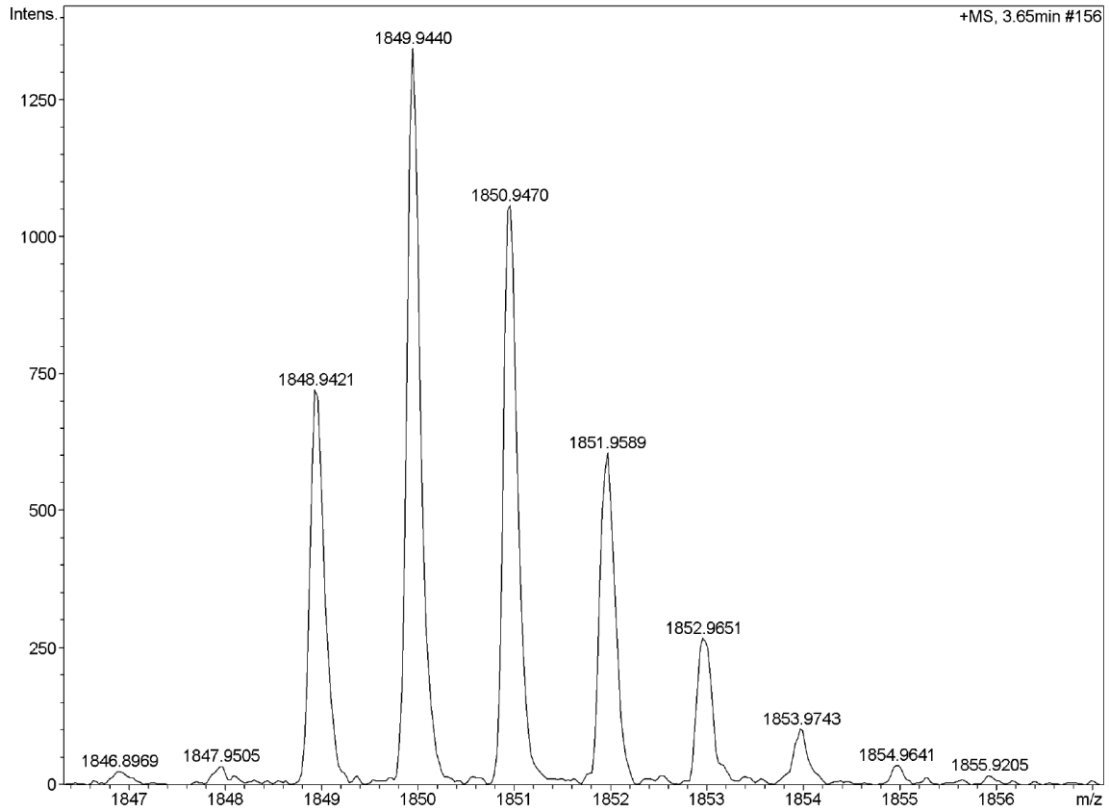

Figure S46. HR mass spectrum (APCI) of the compound ***c*-Ph14**.

8. References

[1] Cai, M.; Zhu, M.; Wang, P.; Song, C. Synthesis and Properties of Novel Poly(aryl ether ketone)s Containing Both Diphenyl Moiety and Amide Linkages in The Main Chains. *Polymer* **2010**, *51*, 1293–1300.

[2] Gasparro, F. P.; Kolodny, N. H. NMR Determination of The Rotational Barrier in *N*,*N*-Dimethylacetamide. A Physical Chemistry Experiment. *J. Chem. Edu.* **1977**, *54*, 258–261.

[3] *Gaussian 09; Revision A.2*; Frisch, M. J.; Trucks, G. W.; Schlegel, H. B.; Scuseria, G. E.; Robb, M. A.; Cheeseman, J. R.; Scalmani, G.; Barone, V.; Mennucci, B.; Petersson, G. A.; Nakatsuji, H.; Caricato, M.; Li, X.; Hratchian, H. P.; Izmaylov, A. F.; Bloino, J.; Zheng, G.; Sonnenberg, J. L.; Hada, M.; Ehara, M.; Toyota, K.; Fukuda, R.; Hasegawa, J.; Ishida, M.; Nakajima, T.; Honda, Y.; Kitao, O.; Nakai, H.; Vreven, T.; Montgomery, J., J. A.; Peralta, J. E.; Ogliaro, F.; Bearpark, M.; Heyd, J. J.; Brothers, E.; Kudin, K. N.; Staroverov, V. N.; Kobayashi, R.; Normand, J.; Raghavachari, K.; Rendell, A.; Burant, J. C.; Iyengar, S. S.; Tomasi, J.; Cossi, M.; Rega, N.; Millam, N. J.; Klene, M.; Knox, J. E.; Cross, J. B.; Bakken, V.; Adamo, C.; Jaramillo, J.; Gomperts, R.; Stratmann, R. E.; Yazyev, O.; Austin, A. J.; Cammi, R.; Pomelli, C.; Ochterski, J. W.; Martin, R. L.; Morokuma, K.; Zakrzewski, V. G.; Voth, G. A.; Salvador, P.; Dannenberg, J. J.; Dapprich, S.; Daniels, A. D.; Farkas, Ö.; Foresman, J. B.; Ortiz, J. V.; Cioslowski, J.; Fox, D. J.; Gaussian, Inc., Wallingford CT, **2009**.

[4] (a) Becke, A. D. Density-functional Thermochemistry. III. The Role of Exact Exchange. *J. Chem. Phys.* **1993**, *98*, 5648. (b) Lee, C.; Yang, W.; Parr, R. G. Development of the Colle-Salvetti Correlation-energy Formula into a Functional of the Electron Density. *Phys. Rev. B: Condens. Matter* **1988**, *37*, 785. (c) Yanai, T.; Tew, D.; Handy, N. A New Hybrid Exchange–correlation Functional Using the Coulomb-attenuating Method (CAM-B3LYP). *Chem. Phys. Lett.* **2004**, *393*, 51–57. (d) Ditchfield, R.; J. Hehre, W.; Pople, J. A. Self-Consistent Molecular-Orbital Methods. IX. An Extended Gaussian-Type Basis for Molecular-Orbital Studies of Organic Molecules. *J. Chem. Phys.* **1971**, *54*, 724. (e) Hehre, W. J.; Ditchfield, R.; Pople, J. A. Self—

Consistent Molecular Orbital Methods. XII. Further Extensions of Gaussian—Type Basis Sets for Use in Molecular Orbital Studies of Organic Molecules. *J. Chem. Phys.* **1972**, *56*, 2257. (f) Hariharan, P. C.; Pople, J. A. The influence of polarization functions on molecular orbital hydrogenation energies. *Theor. Chim. Acta* **1973**, *28*, 213–222.

[5] (a) Yamanaka, S.; Okumura, M.; Nakano M.; Yamaguchi, K. EHF theory of chemical reactions Part 4. UNO CASSCF, UNO CASPT2 and R(U)HF coupled-cluster (CC) wavefunctions. *J. Mol. Struct.* **1994**, *310*, 205–218. (b) Kamada, K.; Ohta, K.; Shimizu, A.; Kubo, T.; Kishi, R.; Takahashi, H.; Botek, E.; Champagne B.; Nakano, M. Singlet Diradical Character from Experiment. *J. Phys. Chem. Lett.* **2010**, *1*, 937–940.

[6] Saint Program included in the package software: APEX3 v2016.1.0

[7] SADABS. Ver. 2014/5. Krause, L.; Herbs-Irmer, R.; Sheldrick, G. M.; Stalke, D. Comparison of Silver and Molybdenum Microfocus X-ray Sources for Single-crystal Structure Determination. *J. Appl. Crystallogr.* **2015**, *48,* 3–10.

[8] SHELXT-Integrated space-group and crystal-structure determination Sheldrick, G. M. *Acta Crystallogr., Sect. A* **2015**, A71, 3.

[9] Sheldrick, G. M. *SHELXT* - Integrated Space-group and Crystal-structure Determination. *Acta Crystallographica., Sect C Structural Chemistry*, **2015**, *71*, 3–8.

[10] Farrugia, L. J. WinGX Suite for Small-molecule Single-crystal Crystallography. *J. Appl. Cryst.* **1999**, *32*, 837–838.